

SIGNAL ENHANCEMENT AND CONVERTED WAVE PROCESSING OF 4C OBC  
SEISMIC DATA FROM THE SHALLOW-WATER ARABIAN GULF

A Thesis

by

HAORAN GUO

Submitted to the Office of Graduate and Professional Studies of  
Texas A&M University  
in partial fulfillment of the requirements for the degree of

MASTER OF SCIENCE

Chair of Committee,	Yuefeng Sun
Committee Members,	Mark E. Everett
	Richard L. Gibson
	Yalchin Efendiev
Head of Department,	Michael Pope

August 2017

Major Subject: Geophysics

Copyright 2017 Haoran Guo

## ABSTRACT

High-quality seismic imaging contributes to geological interpretation, rock property analysis, reservoir characterization and hydrocarbon exploration. Shear wave imaging has been significantly utilized with the development of advanced processing techniques, which improve the quality of seismic stacked imaging. Multi-component data used in this research provide an opportunity to study both compressional waves and converted shear waves. However, the acquisition system in the shallow-water Arabian gulf with the hard seafloor gives rise to dispersive surface waves, which contaminate reflection signals severely. In this thesis, a processing workflow is designed for the 4C OBC seismic data to obtain P-P wave, converted PP-S and PS-S wave imaging in four-component data.

In this study, by considering their characteristics in linearity, surface waves can be separated from reflection signals. Three methods are compared and implemented to remove surface waves, including a bandpass filter, a F-K filter and a F-X filter (named as Surface Wave Noise Attenuation in ProMAX). According to surface wave analysis and comparison of filtering results, the Surface Wave Noise Attenuation methodology can lead to the best result of surface wave removal in shot and receiver domain. Thenceforth, residual noises at far offsets still destroy the reflected signals. FK filters are applied in shot, receiver and CDP domain to suppress residual noises and enhance signals. After several rounds of noise attenuation, the signal-to-noise ratio has a

remarkable increase in 4C seismic data, and clear reflection events appear in the CDP records.

Besides compressional waves, two kinds of converted waveforms exist in the shallow-water environment: PP-S wave (converted from subsurfaces) and PS-S wave (converted at the sea bottom). All wave modes are recorded in the four-component seismic data, so the enhancement of each wave mode is essential to achieve their stacked images. By using the P stacking velocity to do NMO, only the reflection events with P velocities are corrected to flat. After filtering out up-dipping and down-dipping events via FK filters, P wave reflection signals are enhanced, and the velocity analysis of P waves is more accurate. In the same way, converted PP-S and PS-S waves are strengthened and their stacked sections are attained separately in four-component data.

To evaluate these stacked images, synthetic traces are created by convolving the Ricker wavelet with reflection coefficients, which relate to the sonic log and density log data. By plotting synthetic traces in seismic images at CDP702, first, assess how well stacked sections match seismology traces. Then, the energy distribution of various wavefields is analyzed in four components. These two criteria decide the better stacked images to describe the real geological structures. Ideally, these images should reflect the same subsurface structures. However, because of various wavefields and different measurement, there exist slight variations between P-P wave, PP-S and PS-S wave imaging. In summary, the processing sequence developed in the thesis achieved signal enhancement, P wave and converted shear wave imaging, which can improve the geological interpretation and hydrocarbon exploration.

## DEDICATION

I dedicate my thesis to my parents who supported me without reservation for a good education.



## ACKNOWLEDGEMENTS

I would like to offer my appreciation to my committee chair, Dr. Yuefeng Sun, for his support and help in various aspects. And I would like to thank my committee members, Dr. Everett, Dr. Gibson, and Dr. Efendiev for their guidance and support throughout my master research at Texas A&M University.

My grateful thanks also go to my friends, my colleagues in our group and the department faculty and staff for offering me academic help and making my time at Texas A&M University a great experience.

Finally, I am grateful for all support and encouragement from my family.

## CONTRIBUTORS AND FUNDING SOURCES

This work was supervised by a thesis committee consisting of Professor Yuefeng Sun [advisor], Mark E. Everett and Richard L. Gibson of the Department of Geology and Geophysics and Professor Yalchin Efendiev of the Department of Mathematics.

All work for the thesis was completed by the student, under the advisement of Professor Yuefeng Sun of the Department of Geology and Geophysics.

Graduate study was supported by a research scholarship from Williford Scholars.

## NOMENCLATURE

4C	Four Components
OBC	Ocean Bottom Cable
NMO	Normal Moveout Correction
$V_p$	Velocity of Compressional Wave
$V_s$	Velocity of Shear Wave
S/N	Signal to Noise Ratio
CMP	Common Middle Point
CCP	Common Converted Point
ACP	Asymptotic Converted Point

## TABLE OF CONTENTS

	Page
ABSTRACT .....	ii
DEDICATION .....	iv
ACKNOWLEDGEMENTS .....	v
CONTRIBUTORS AND FUNDING SOURCES.....	vi
NOMENCLATURE.....	vii
TABLE OF CONTENTS .....	viii
LIST OF FIGURES .....	x
LIST OF TABLES .....	xiv
1. INTRODUCTION.....	1
1.1 Research Motivation .....	2
1.2 Research Objective.....	2
1.3 Geological Background and Dataset .....	3
2. SURFACE WAVE ANALYSIS .....	5
2.1 Introduction .....	5
2.2 Literature Review .....	6
2.3 Methods .....	8
2.3.1 Surface Wave Noise Attenuation .....	8
2.3.2 Bandpass Filter .....	9
2.3.3 FK Filter .....	9
2.4 Results .....	9
2.5 Summary .....	12
3. SIGNAL ENHANCEMENT AND DATA PROCESSING.....	29
3.1 Introduction .....	29
3.2 Literature Review .....	30
3.2.1 Conventional P Wave Processing.....	30
3.2.2 Converted Shear Wave Processing.....	30

3.2.3 Multi-Component Seismic Data Processing.....	31
3.2.4 Application of Shear Wave Imaging .....	32
3.3 Processing Flow and Methods.....	33
3.3.1 Surface Wave Attenuation.....	33
3.3.2 Residual Noise Removal .....	34
3.3.3 Wave Mode Enhancement.....	34
3.3.4 Velocity Analysis and Stacking .....	35
3.4 Results .....	41
3.4.1 Log Data Analysis and Velocity Model .....	41
3.4.2 Surface Wave Attenuation Results .....	45
3.4.3 Residual Noise Removal Results .....	46
3.4.4 Wave Mode Enhancement Results .....	65
3.4.5 Seismic Data Stacking Results .....	65
3.4.6 Wave Mode Analysis and Geological Interpretation .....	73
4. CONCLUSIONS .....	87
REFERENCES .....	89

## LIST OF FIGURES

	Page
Figure 1: Location map of the study area.....	4
Figure 2: Portions of raw shot records: (a) Pressure component (b) Inline component (c) Crossline component (d) Vertical component.....	13
Figure 3: Frequency spectra of raw shot records: (a) Pressure component (b) Inline component (c) Crossline component (d) Vertical component. ....	15
Figure 4: Frequency decomposition in pressure component: 4-6-17-20, 17-20-45-55, 45-55-75-80 and 75-80-110-120Hz. ....	16
Figure 5: Frequency decomposition in inline component: 4-6-15-20, 15-20-35-45, 35- 45-75-80 and 75-80-110-120Hz. ....	17
Figure 6: Frequency decomposition in crossline component: 4-6-15-20, 15-20-35-45, 35-45-75-80 and 75-80-110-120Hz. ....	18
Figure 7: Frequency decomposition in vertical component: 4-6-15-20, 15-20-45-55, 45-55-75-80 and 75-80-110-120Hz. ....	19
Figure 8: A portion of the raw shot record of pressure component illustrates the velocity range of surface waves.....	20
Figure 9: After three Surface Wave Noise Attenuation filters: (a) a portion of the shot record of pressure component (b) a portion of extracted surface waves. ....	21
Figure 10: After Bandpass Filter: (a) a portion of the shot record of pressure component (b) a portion of extracted surface waves. ....	22
Figure 11: Frequency-wavenumber spectrum of the pressure component shot record using 2D Fourier transform in which the blue polygon represents the rejecting zone.....	23
Figure 12: After FK Filter when the polygon is rejected: (a) a portion of the shot record of pressure component (b) a portion of extracted surface waves. ....	24
Figure 13: After FK Filter when the polygon is accepted: (a) a portion of the shot record of pressure component (b) a portion of extracted surface waves. ....	25
Figure 14: Frequency spectra: (a) Surface Wave Noise Attenuation (b) Bandpass Filter (c) FK Filter (rejected) (d) FK Filter (accepted).....	26

Figure 15: Portions of the shot record of pressure component (a) After three Surface Wave Noise Attenuation filters (b)After Bandpass Filter (c) After FK Filter (rejected) (d) After FK Filter (accepted). .....	27
Figure 16: PS-S waveform: (a) Raypath (b) Stack binning. ....	37
Figure 17: PP-S waveform: (a) Raypath (b) Stack binning. ....	38
Figure 18: Pressure component and inline component data processing workflow. ....	39
Figure 19: Illustrating the statistic $V_p/V_s$ value from log data. ....	40
Figure 20: Processing sequences to preserve P wave reflection signals. ....	40
Figure 21: Gamma ray, density (blue) & neutron porosity (red), effective porosity, water saturation, P (blue) & S (red) velocity, and $V_p/V_s$ (from left to right) at the depth C636.52m-C941.32m from the Well B.....	43
Figure 22: A portion of the raw shot record of pressure component. ....	48
Figure 23: After three Surface Wave Noise Attenuation filters, a portion of the shot record of pressure component.....	49
Figure 24: After sorting to the receiver domain, a portion of the receiver record of pressure component, showing residual surface waves. ....	49
Figure 25: After three Surface Wave Noise Attenuation filters, a portion of the receiver record of pressure component.....	50
Figure 26: (a) Same as Figure 23 (b) After sorting to the shot domain, a portion of the shot record of pressure component. ....	51
Figure 27: A portion of the raw shot record of inline component (a) Opposite phases between positive offsets with negative offsets (b) After phase rotation in positive offsets. ....	52
Figure 28: After phase rotation, a portion of the shot record of inline component.....	52
Figure 29: After the same flows to remove surface waves, a portion of the shot record of inline component, showing residual noises. ....	53
Figure 30: After FK Filter, a portion of the shot record of pressure component. ....	53
Figure 31: After removing residual noises, a portion of the CDP record of pressure component.....	54

Figure 32: After FK Filter, a portion of the shot record of inline component.....	54
Figure 33: After removing residual noises, a portion of the CDP record of inline component.....	55
Figure 34: Preprocessed CDP record of crossline component. ....	55
Figure 35: Preprocessed CDP record of vertical component. ....	56
Figure 36: Pressure component data: (a) A portion of the raw shot record (b) Frequency spectrum of the raw shot record (c) A portion of the preprocessed shot record (d) Frequency spectrum of the preprocessed shot record. ....	57
Figure 37: Inline component data: (a) A portion of the raw shot record (b) Frequency spectrum of the raw shot record (c) A portion of the preprocessed shot record (d) Frequency spectrum of the preprocessed shot record. ....	59
Figure 38: Crossline component data: (a) A portion of the raw shot record (b) Frequency spectrum of the raw shot record (c) A portion of the preprocessed shot record (d) Frequency spectrum of the preprocessed shot record. ....	61
Figure 39: Vertical component data: (a) A portion of the raw shot record (b) Frequency spectrum of the raw shot record (c) A portion of the preprocessed shot record (d) Frequency spectrum of the preprocessed shot record. ....	63
Figure 40: Pressure component data: (a) Preprocessed CDP record (b) CDP record after extracting P wave reflections, showing hyperbolic P wave reflections; (c) CDP record after extracting PP-S wave reflections, showing hyperbolic PP-S wave reflections; (d) CDP record of after extracting PS-S wave, showing hyperbolic PS-S- wave reflections. ....	67
Figure 41: Inline component data: (a) Preprocessed CDP record (b) CDP record after extracting P wave reflections, showing hyperbolic P wave reflections; (c) CDP record after extracting PP-S wave reflections, showing hyperbolic PP-S wave reflections; (d) CDP record of after extracting PS-S wave, showing hyperbolic PS-S- wave reflections.....	68
Figure 42: Pressure component data: (a) P-P stacked section (b) PP-S stacked section (c) PS-S stacked section.....	69
Figure 43: Inline component data: (a) P-P stacked section (b) PP-S stacked section (c) PS-S stacked section. ....	70



Figure 44: Crossline component data: (a) P-P stacked section (b) PP-S stacked section (c) PS-S stacked section.....	71
Figure 45: Vertical component data: (a) P-P stacked section (b) PP-S stacked section (c) PS-S stacked section.....	72
Figure 46: Illustrating P wave acoustic impedance, reflection coefficient and synthetic trace with different-frequency Ricker wavelets (100Hz and 20Hz), based on P wave sonic log and density log data. ....	76
Figure 47: Illustrating PP-S wave acoustic impedance, reflection coefficient and synthetic trace with different-frequency Ricker wavelets (100Hz and 20Hz), based on S wave sonic log and density log data. ....	77
Figure 48: Illustrating PS-S wave acoustic impedance, reflection coefficient and synthetic trace with different-frequency Ricker wavelets (100Hz and 20Hz), based on S wave sonic log and density log data. ....	78
Figure 49: Portions of P stacked sections at the reservoir zone with synthetic P-wave reflection signals: (a) Hydrophone; (b) Inline geophone; (c) Crossline geophone; (d) Vertical geophone.....	79
Figure 50: Portions of PP-S stacked sections at the reservoir zone with synthetic PP-S wave reflection signals: (a) Hydrophone; (b) Inline geophone; (c) Crossline geophone; (d) Vertical geophone.....	81
Figure 51: Portions of PS-S stacked sections at the reservoir zone with synthetic PS-S wave reflection signals: (a) Hydrophone; (b) Inline geophone; (c) Crossline geophone; (d) Vertical geophone.....	83
Figure 52: (a) P stacked section in pressure component (b) PP-S stacked section in vertical component (c) PS-S stacked section in inline component.....	85

## LIST OF TABLES

	Page
Table 1: Velocity model based on sonic log data and geological background. ....	44
Table 2: Illustrating P-P wave, PP-S wave and PS-S wave energy distributions in pressure component, inline component and vertical component data. ....	86

## 1. INTRODUCTION

An accurate subsurface imaging via seismic data processing is critical for geological interpretation and hydrocarbon exploration. Four-component seismic data can improve the imaging of subsurface structures and offer the great potential in converted shear wave study. With the development of shear-wave acquisition and processing techniques, the advantages of shear-wave processing include imaging through a gas cloud and imaging subsalt features (Stewart et al., 2003). However, the shear source is not suitable in the marine environment and very costly. The research on 4C seismic data provides an access to obtain converted shear waves in the offshore field.

The converted P-SV mode occurs at the seafloor (Tatham et al., 1984) and the processing techniques are proposed to gain the SV-SV imaging in the marine environment. Based on the modelling results (Sun et al., 2009), the P-S conversion at the sea bottom in the shallow-water environment (around 10 meters depth) is more than a thousand times stronger than that in other deep-water environments (>100 meters depth). Zhang (2015) developed an advanced processing flow to obtain the stacked result of converted P-S wave at the sea floor. However, Johns et al. (2006) gained P-SV prestack time imaging by processing P-SV waves converted from subsurfaces. The conversion mode is actually complicated in the shallow-water Arabian Gulf. Therefore, both P-SV conversions at the seafloor and at subsurfaces are analyzed in this research. By developing a 4C seismic processing workflow, P wave and converted shear wave reflection signals are processed and imaged with high S/N.

## **1.1 Research Motivation**

The quality of seismic imaging depends on the field environment, the acquisition system and processing sequences. The research data were acquired in the Arabian Gulf, where there are high-velocity layers at very shallow depth, which trap the energy and cause strong surface waves and multiples. And due to the insufficient time delay between shots, surface waves contaminate not only the present shot gather, but also the next one at far offsets (Sun and Berteussen, 2010). So, existing surface waves create great difficulties in the following processing sequences.

In previous studies, conventional processing flows are applied for single-component seismic data (Yilmaz, 2001). For multi-component data, both P waves and converted shear waves are recorded. Sun et al. (2009) proposed that the strong P-S conversion happens at the sea bottom in the shallow-water environment of Arabian Gulf. However, the complication of conversion modes and characteristics of converted waves make it more difficult to gain an accurate converted shear-wave imaging. Therefore, based on the wave characteristic of real data, it is necessary to design a processing flow for the 4C OBC seismic data in the shallow-water environment.

## **1.2 Research Objective**

The purposes of this research are as follows: 1) Separate reflection signals from strong surface waves to increase the signal-to-noise ratio; 2) Develop a proper four-component processing flow, by using the research data from the shallow-water Arabian Gulf to gain a more accurate subsurface imaging.

An interface wave may propagate at the water-solid contact in the offshore field. Its propagation velocity is related to the shear velocity of the shallowest sediment layer ( $V_s$ ). The interface wave may be a slower Scholte wave ( $V_s < V_{sea}$ ) or a faster Rayleigh wave ( $V_s > V_{sea}$ ). In most marine environments, shear velocity in the shallowest layer is less than the propagation velocity in the seawater. So, Hardage et al. (2011) suggested the Scholte wave will be the dominant surface wave in most 4C marine projects. Accordingly, a key objective of the study is to part Scholte waves from reflection signals.

The converted P-S mode at the seafloor is achievable (Tatham et al., 1984), and it is also possible to record the P-S wave converted from subsurfaces (Johns et al., 2006). However, considering the existence of two conversion modes is not performed in previous studies. Thus, another objective is to develop a processing flow for the 4C OBC seismic data to obtain P-wave and PS-wave imaging.

### **1.3 Geological Background and Dataset**

The study area is located around the offshore fields in U.A.E. (Figure 1). The seismic data acquired in this area are the four-component Ocean Bottom Cable (OBC) data along two 2D lines. In this study, only one of these 2D lines is processed, which consists of two segments from the North to the South. There are totally 1195 shots, among which 600 shots are from the northern segment and 595 shots are from the southern segment. Because of 10 shots overlap between these two segments, the seismic data only has 1185 shots (Shot 1001-2185) in inline, crossline, vertical and pressure component. For Shot 1179, there are only pressure component data with 96 channels.

That's why inline, crossline and vertical component data have the same 419869 channels, but pressure component data have 419965 channels. The water depth along the test line is less than 20m. The air gun depth is 5m. The source spacing is about 19m and the receiver spacing is 25m. Each detector is consisted of a hydrophone and a 3D geophone. So, seismic data record pressure variations by hydrophones and motions by geophones. The recording length is 6s, and the sample rate is 2ms.

Well log data are also available in this research, which include P-wave and S-wave velocity, Gamma ray, density, porosity and saturation. It is essential to estimate the potential reservoir via analyzing log data. Based on the well coordinates, the closest distance between the test line and the well is 733m at CDP702. So, well log tie at CDP702 will greatly verify the interpretation of seismic imaging.



**Figure 1: Location map of the study area.**

## 2. SURFACE WAVE ANALYSIS

### 2.1 Introduction

The shallow-water (less than 20m) environment with the hard sea floor in the study area lead to strong surface waves. The OBC acquisition system in offshore fields can detect Scholte waves (Boiero et al., 2013). In the study, the 4C OBC seismic data record Scholte wave (Label B) in pressure (Figure 2(a)), inline (Figure 2(b)), crossline (Figure 2(c)) and vertical (Figure 2(d)) component. Due to inadequate time interval between shots, Scholte waves from previous shots (Label A) also contaminate shot records at far offsets (Sun, 2007). Label C shows head waves. Because of the different measurements of hydrophones and geophones, only the shot record in pressure component shows hyperbolic reflections (Label D) at near offsets. Inline geophones record the displacement of shear waves, but there is no useful reflection signal, instead noises. Strong acoustic waves trapped in the water column are also detected by inline geophones, especially in the shallow-water environment with hard sea bottom (Sun, 2007). Likewise, crossline geophones record acoustic waves trapped in the water column, like wave guides. Because coupling of inline geophones is better than that of crossline geophones, Scholte waves are highly mixed with reflection signals in crossline component (Figure 2(c)). Zhang et al. (2015) suggested the noises in crossline records could contaminate the vertical records, due to the energy leakage. Thus, vertical component records (Figure 2(d)) have a lower S/N than pressure and inline component records.

Sun et al. (2007) proposed the dominant frequency of surface wave is around 10Hz, but the dominant frequency of reflected wave is around 20Hz. Figure 3 shows the frequency spectra of four-component raw shot records. Because the physical measurements are different, the raw power recorded by hydrophones is thirty thousand times than that by 3D geophones. By comparing the power at 10Hz and at 20Hz (Figure 3), the signal-to-noise ratio in pressure and inline components is higher than crossline and vertical records.

Florian et al. (2017) developed a method to estimate shear-wave velocity by utilizing the characteristics of surface waves. On the other hand, Scholte waves can be considered as unwanted noises, contaminating the signals in shallow-water seismic data. Thus, it is necessary to separate surface waves from reflection signals in the study.

## **2.2 Literature Review**

Surface waves propagate along the interface. A Scholte wave is a surface wave propagating at an interface between a fluid and an elastic solid medium. Because the energy of surface waves is the maximum at water/solid interface and decreases exponentially away from the interface, sources and receivers should be located close to the seafloor. Boiero et al. (2013) demonstrated Scholte waves can be detected by Ocean Bottom Cable (OBC) in the shallow marine environment. Ernst and Herman (2000) proposed guided waves, which are reflected multiples in one layer separated from the surrounding medium by high-impedance contrasts. So, the shallow marine environment leads to guided waves in the water column, which cover large parts of seismic records as well. In the study data, surface waves include the trapped waves in the water column and



the interface waves at the hard sea bottom, which have a negative impact on the data quality and geological interpretation.

Geophysicists have designed various methodologies to separate surface waves from useful reflected waves. Yilmaz (2011) proposed bandpass filtering and FK filtering are efficient approaches to eliminating noises, based on spectral analysis. Henley (1999) suggested linear noises can be attenuated in the radial-trace (R-T) domain by a low-cut filter. For Scholte waves in the shallow-water Arabian Gulf, Zhang et al. (2010) designed a T-F-K filter by using S transform, which provides FK spectra analysis in time domain. The S transform converts data from T-X domain to TFK domain. The S transform formula of a time series  $u(t)$  (Stockwell et. al., 1996) is expressed as:

$$S(t, f) = \int_{-\infty}^{+\infty} u(\tau) \cdot w(t - \tau, \sigma(f)) \cdot \exp(-j2\pi f\tau) d\tau$$

Where the Gaussian window is  $w(t, \sigma(f)) = \frac{1}{\sigma(f)\sqrt{2\pi}} \cdot \exp(-\frac{t^2}{2\sigma^2(f)})$ .

To adjust the Gaussian window, variable-factor S transform is proposed (Pinnegar and Mansinha, 2003a):

$$S(t, f, \beta) = \int_{-\infty}^{+\infty} u(t) \cdot w(t - \tau, f, \beta) \cdot \exp(-j2\pi f\tau) d\tau.$$

Stockwell (2007) demonstrated the width of window depends on the frequency, and lower frequencies lead to a wider window, which can provide better localization in the frequency domain.

To analyze signals in both the time-space domain and frequency-wavenumber domain, the expression of TFK transform is:

$$TFK(\tau, f, k) = \int_{-\infty}^{+\infty} \int_{-\infty}^{+\infty} u(t, x) \exp(-j2\pi kx) w(t - \tau, \sigma(f)) \exp(-j2\pi f\tau) dx d\tau$$

Compared with the conventional FK transform, the TFK transform has advantages when the FK panel of data varies with time. Zhang et al. (2013) also designed an approach to removing surface waves by a two-step strategy, which includes a time-frequency-wavenumber (TFK) filter and a TFK dependent polarization filter.

Even though these advanced methodologies may improve S/N better, the main objective of this research is to find a processing flow, which can perform different-wavetype stacking for four-component data. Therefore, only three basic methods are tested and applied to separate Scholte waves in the study, which are Surface Wave Noise Attenuation, Bandpass Filter and F-K Filter in the ProMAX seismic software.

## 2.3 Methods

### 2.3.1 Surface Wave Noise Attenuation

In the Surface Wave Noise Attenuation flow, low-frequency arrays are formed, based on the surface velocity and the frequency cut-off. The seismic data are transformed from the T-X (time-space) domain to the F-X (frequency-space) domain. At each frequency, the number of traces to mix is determined by the formula:

$$\text{Mix} = \text{velocity} / (\text{frequency} * \text{trace spacing}).$$

Then the data are transformed back to the T-X domain. Surface wave noise attenuation operates on the data in panels, which are overlapped and merged together. Each panel normally contains panel size traces. The first and last panel edge traces overlap with adjacent panels. Within the panel edges, panel mix traces from adjacent

panels are mixed and output. Remaining traces in the edges are discarded. Frequency components higher than the cutoff frequency remain unchanged. (ProMAX, 1997)

### *2.3.2 Bandpass Filter*

Bandpass Filter is in fact a frequency filter. A single four-frequency Ormsby filter is used to all traces at all times. These four frequencies represent the 0 and 100 percent of the low-cut ramp, and the 100 and 0 percent of the high-cut ramp. These ramps are formed by cosine tapers in the frequency domain. (ProMAX, 1997)

### *2.3.3 FK Filter*

First, the F-K filter transforms data from the T-X domain to F-K (frequency-wavenumber) domain by a 2D Fourier Transform. An arbitrary polygon is specified in the F-K domain, which is used to pass or reject signals. If passing, the filter almost doesn't attenuate the signals within the specific polygon, instead attenuating those outside of the polygon. But if rejecting, the data within the polygon are attenuated strongly without affecting the outside data. In the end, the data are converted internally into the T-X domain via the inverse Fourier Transform. (ProMAX, 1997)

## **2.4 Results**

Figure 4-7 show the frequency decomposition of pressure, inline, crossline and vertical component records. The linear surface waves mostly exist in the frequency range of lower than 15Hz in all four components of seismic data. In the pressure record, hyperbolic reflections exist at the frequency range 17-20-45-55Hz. Surface waves are highly dispersive. Due to the different measurements, the vertical component record (Figure 7(b)) is influenced by surface waves more seriously than the pressure record.

Horizontal records (Figure 5(b) and 6(b)) are worse at the frequency range 15-20-35-45Hz where surface waves are mixed with reflected waves severely.

To part surface waves from desired signals, the frequency and velocity features of surface waves should be analyzed. By measuring the velocity values of linear surface waves in shot domain (Figure 8), the velocity range is approximately from 750m/s to 1500m/s. All the approaches to removing surface waves are based on the wave characteristics of real data.

The Surface Wave Noise Attenuation uses surface wave velocity values and the cut-off frequency in the F-X domain. Based on the surface wave analysis, three Surface Wave Noise Attenuation filters are designed, which have 750m/s, 1000m/s and 1500m/s as the velocity values. And the frequency cut-off is set as 20Hz. Figure 9(a) shows the shot record in pressure component after these filters, and Figure 9(b) shows the extracted Scholte waves by using Surface Wave Noise Attenuation. Compared with the raw shot gather, surface waves are attenuated clearly by this method in Figure 9(a). Thus, this methodology achieved surface noise attenuation and signal enhancement.

By analyzing the frequency spectra, surface waves have a narrow range of low frequencies between 0 and 15Hz, and the dominant frequency is around 10Hz. Four frequency values of Bandpass Filter should be set to form the low-cut and high-cut ramp. In this case, the low-cut ramp is 12-15Hz and the high-cut ramp is 100-110Hz. Figure 10(a) and 10(b) show the shot record after bandpass filtering and the extracted surface waves by this filter. In Figure 10(a), low-frequency and high-frequency noises are suppressed obviously by bandpass filtering, but there are still residual linear Scholte

waves in the shot gather. So, Bandpass Filter can be used to remove Scholte waves. However, there are still linear surface noises in the shot gather, whose frequencies are larger than 12Hz. And some desired signals with very low frequencies may be also suppressed by this bandpass filter.

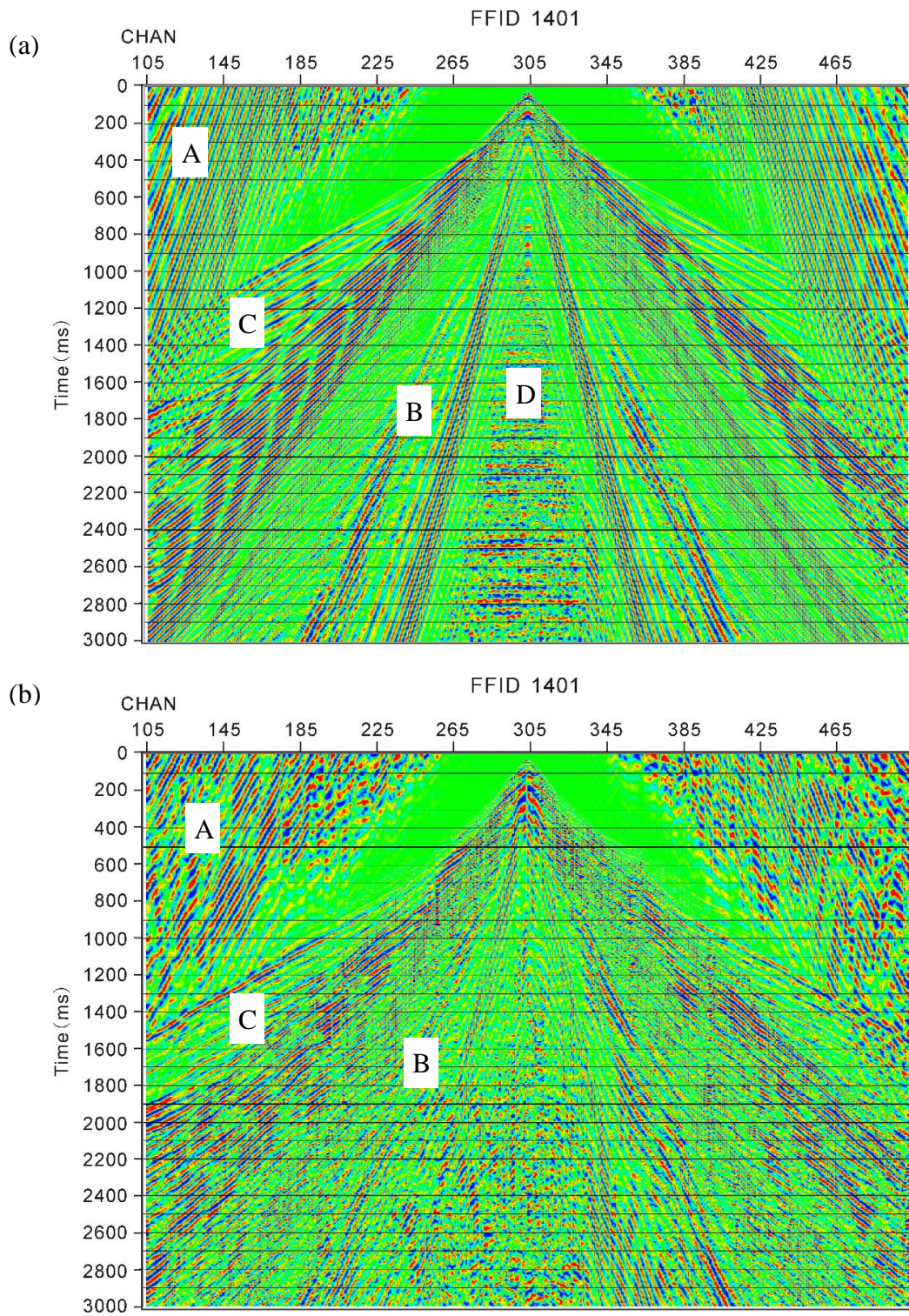
The F-K Filter first transforms the seismic data from X-T domain to F-K domain. Because surface waves are low-frequency and low-velocity, they should be close to the wavenumber axis in the FK spectrum. Figure 11 shows the FK panel, in which a picked polygon near the wavenumber axis represents surface waves. Due to the processing software effect, two processing flows are applied to perform FK filtering. First, by considering the picked polygon as a rejected zone, the filtered shot gather is shown in Figure 12(a). In another flow, the picked polygon is treated as an accepted zone, so the filtered surface waves are shown in Figure 13(b). Then, the raw record is subtracted by the filtered surface waves to obtain the reflection signals in Figure 13(a). Compared with the raw shot gather, both shot gathers in Figure 12(a) and 13(a) show more reflections after suppressing surface noises, but some residual surface waves still exist. So, it can be concluded the reflection signals can be enhanced by FK Filter.

Figure 14 shows the frequency spectra of these filtered results in Figure 9(a), 10(a), 12(a) and 13(a). After these methodologies, the energy at the frequency 30Hz is around 0.0095. The frequency spectrum after three Surface Wave Noise Attenuation filters in Figure 14(a) indicates that the 10Hz frequency content is suppressed to 0.0003. Figure 14(b) illustrates the bandpass filter suppresses the frequency contents below 12Hz to zero. Figure 14(c) and (d) are the frequency spectra after two strategies of FK filter, in

which the raw power of surface-wave frequencies around 10Hz is suppressed to 0.0005. Meanwhile, the frequency contents of reflections are enhanced.

## **2.5 Summary**

To conclude, surface waves have low frequencies, low velocities and high amplitudes. Figure 15 shows the filtered shot results by using Surface Wave Noise Attenuation, Bandpass Filter and FK Filter. The Rejected polygon in FK Filter (Figure 15(c)) leads to the same result as the accepted polygon with subtraction (Figure 15(d)). And the shot record after Surface Wave Noise Attenuation (Figure 15(a)) shows more continuous and strong reflection signals. Even though the bandpass filter removes all the frequency contents which are less than 12Hz, there are still residual surface waves clearly in Figure 15(b). On the other hand, it may be not possible to do inversion with damaging low-frequency signals. By observing their frequency spectra (Figure 14), Surface Wave Noise Attenuation suppresses the energy of 10Hz frequency to 0.0003, but FK Filter just suppresses it to 0.0005. Thus, Surface Wave Noise Attenuation is the best approach to removing surface noises and enhancing reflection signals in this study.



**Figure 2: Portions of raw shot records: (a) Pressure component (b) Inline component (c) Crossline component (d) Vertical component.**



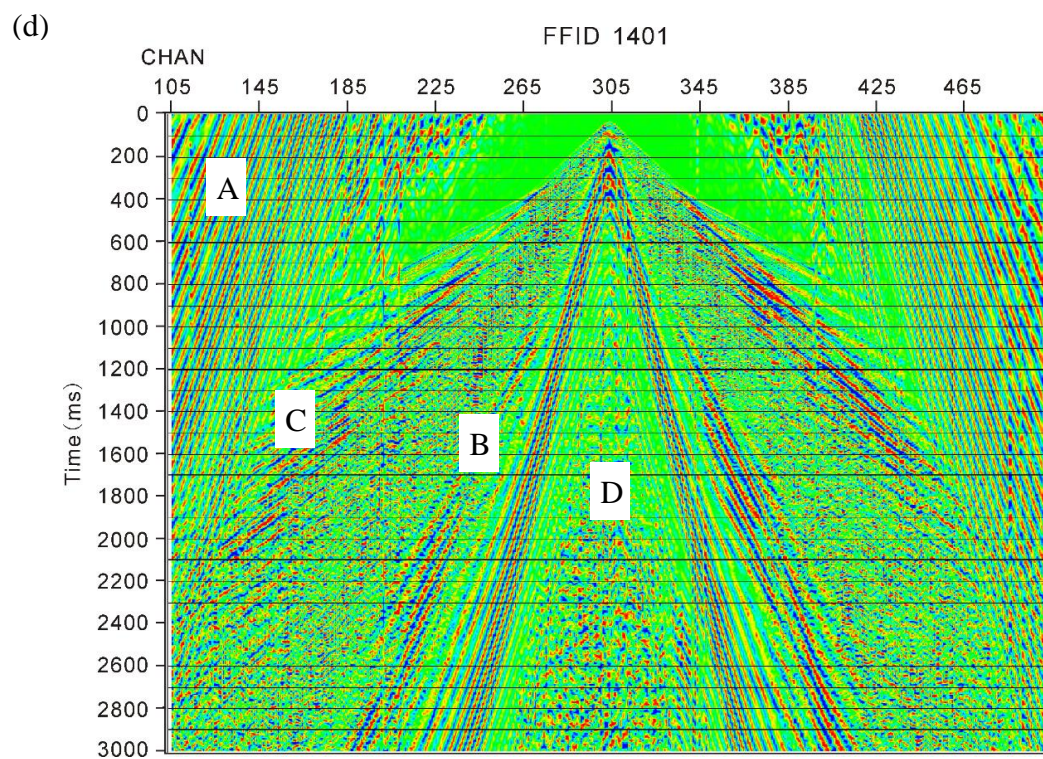
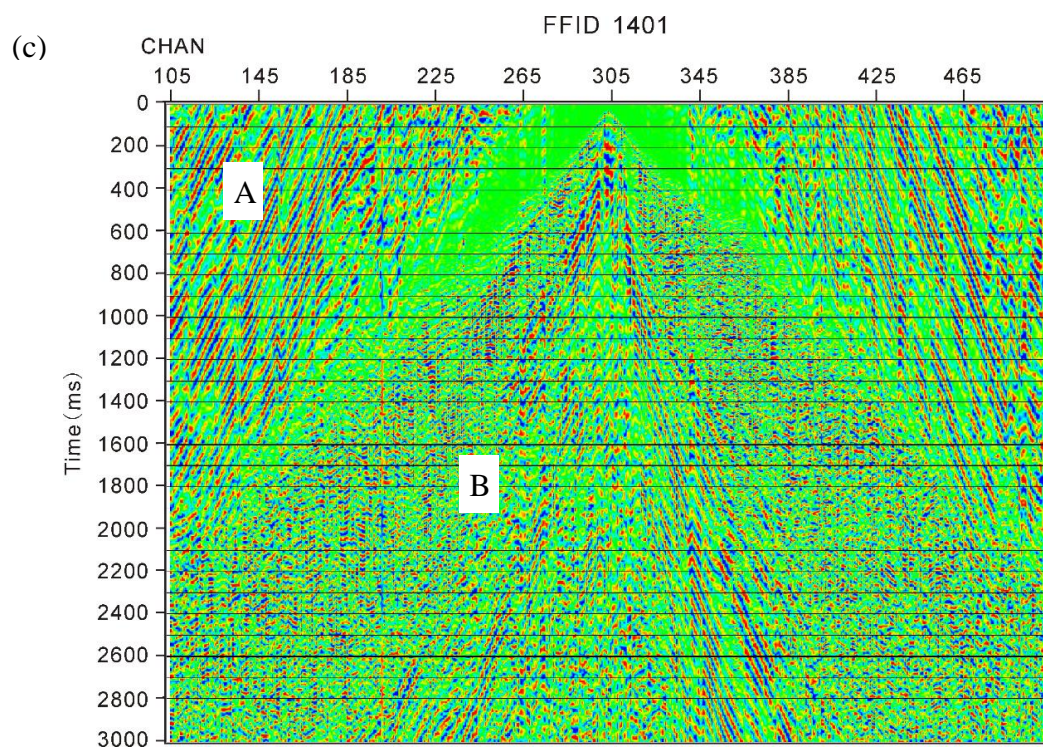


**Figure 2: Continued.**



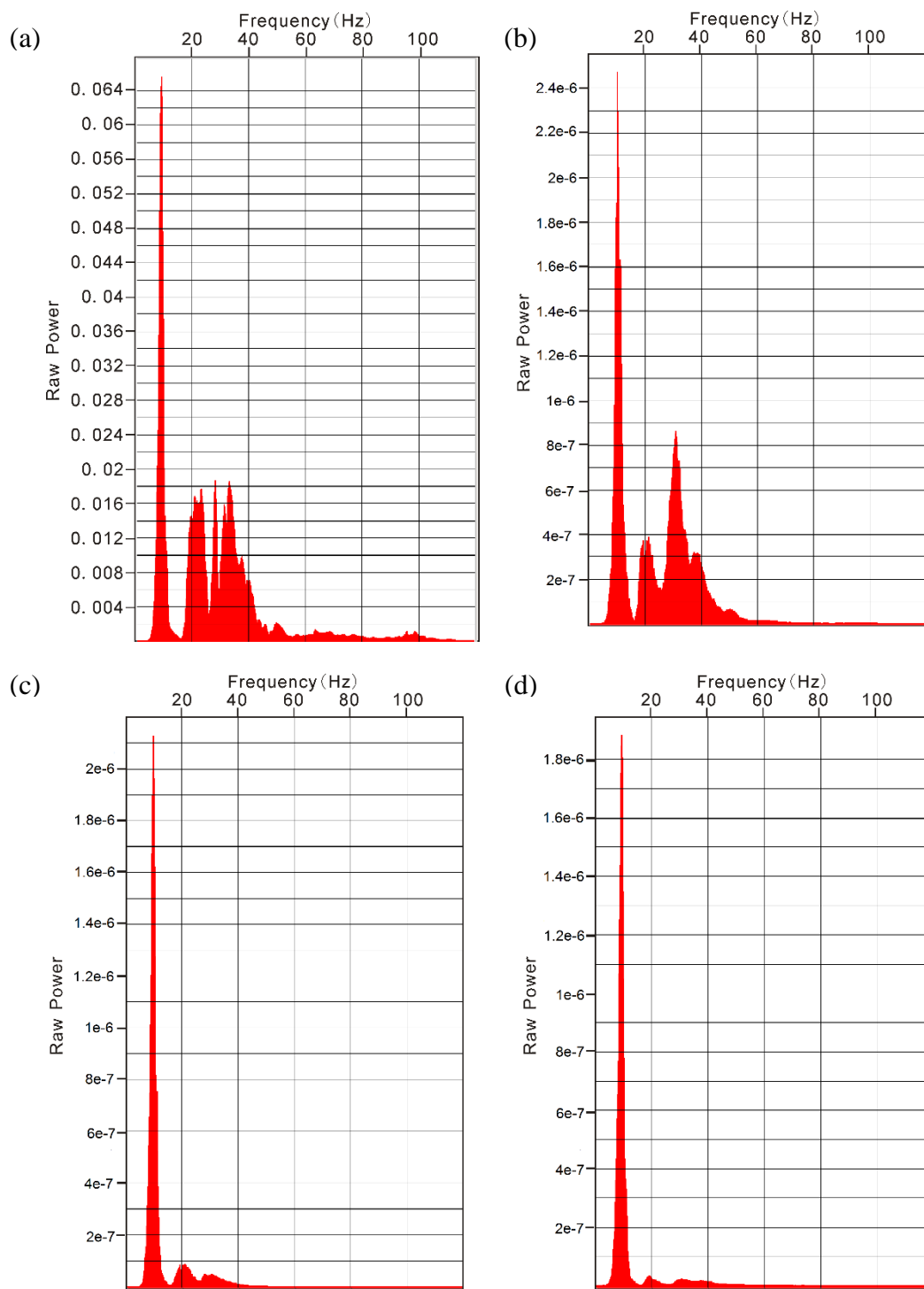


**Figure 3: Frequency spectra of raw shot records: (a) Pressure component (b) Inline component (c) Crossline component (d) Vertical component.**

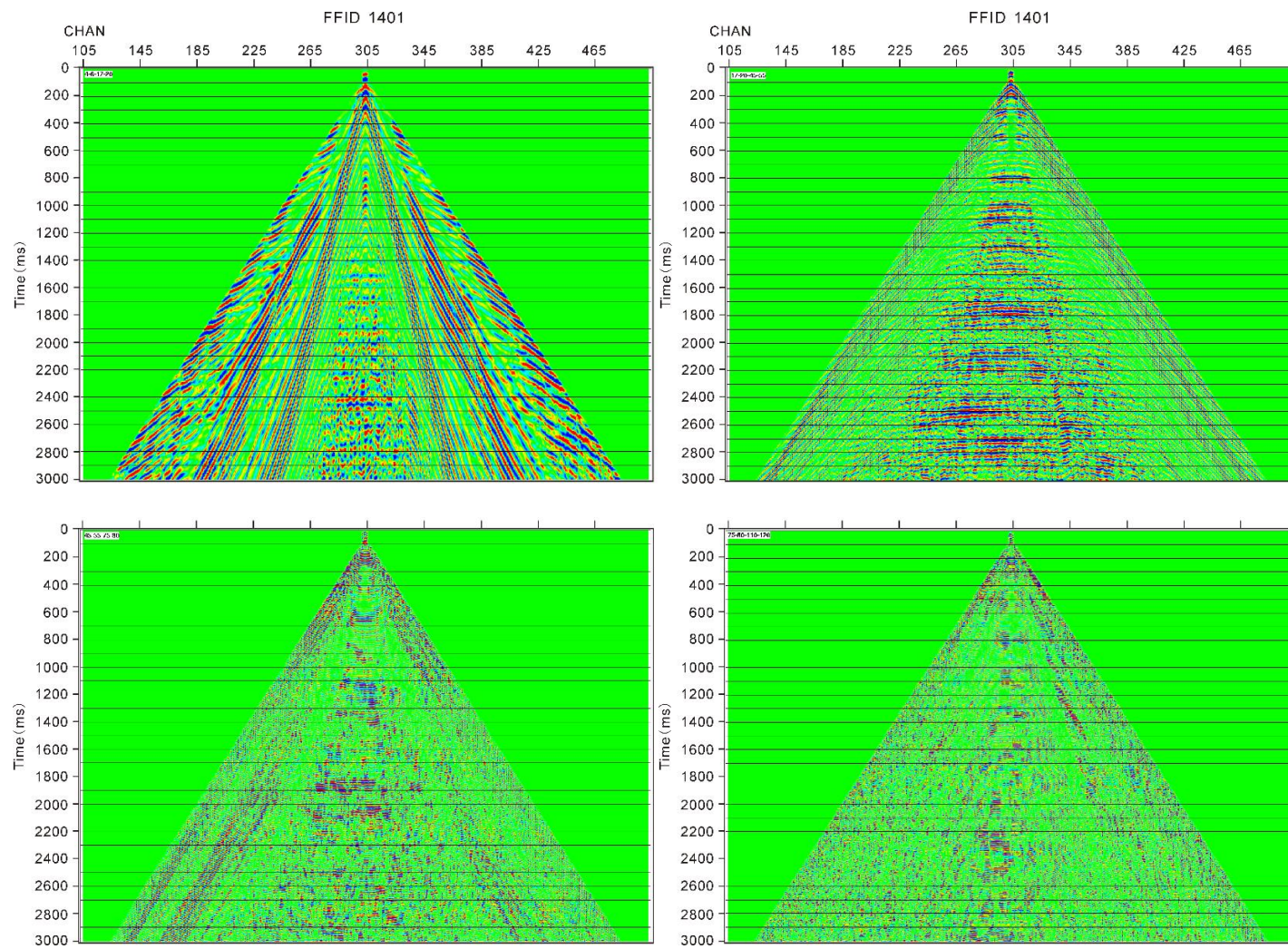


**Figure 4: Frequency decomposition in pressure component: 4-6-17-20, 17-20-45-55, 45-55-75-80 and 75-80-110-120Hz.**

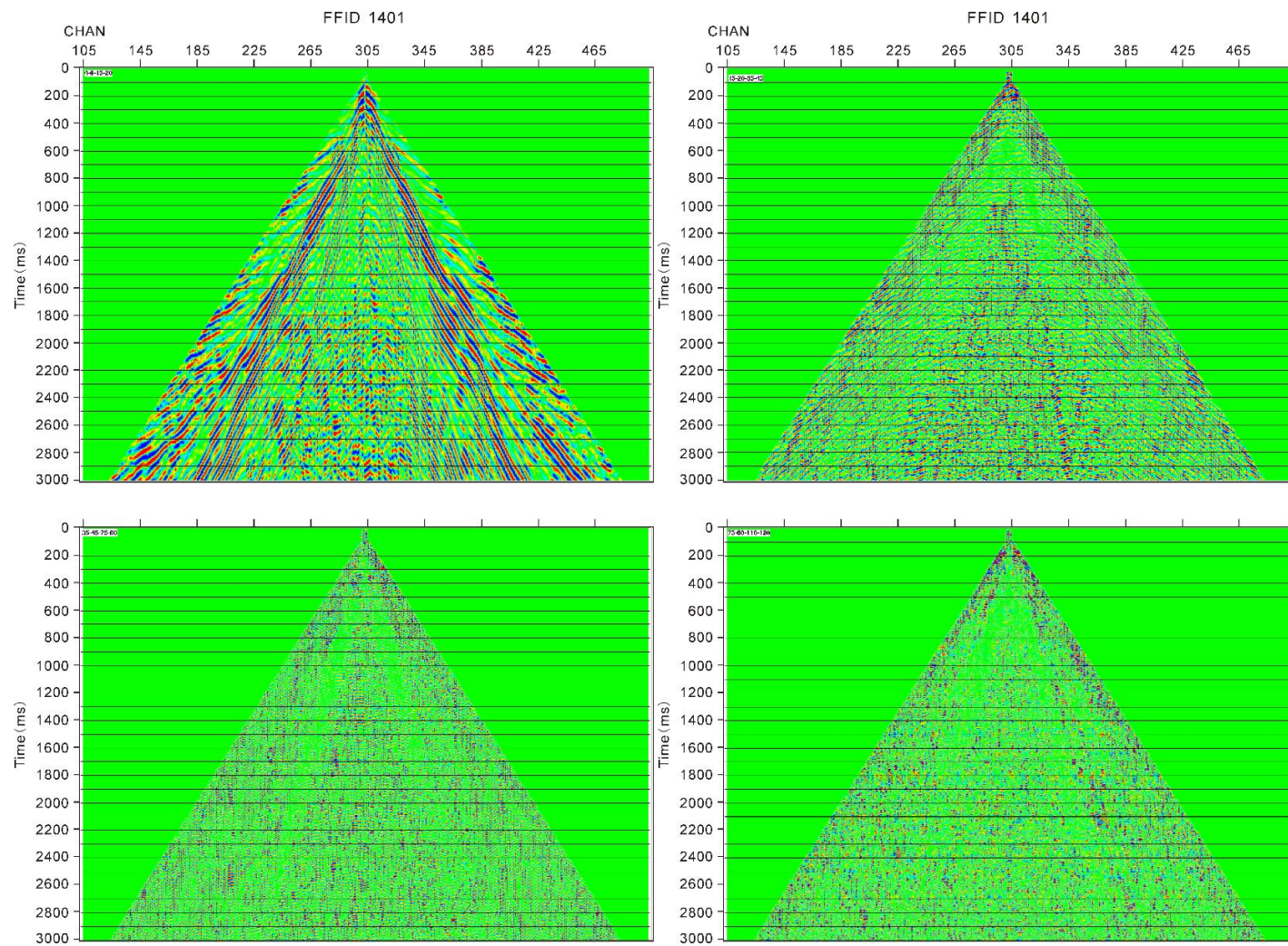


**Figure 5: Frequency decomposition in inline component: 4-6-15-20, 15-20-35-45, 35-45-75-80 and 75-80-110-120Hz.**



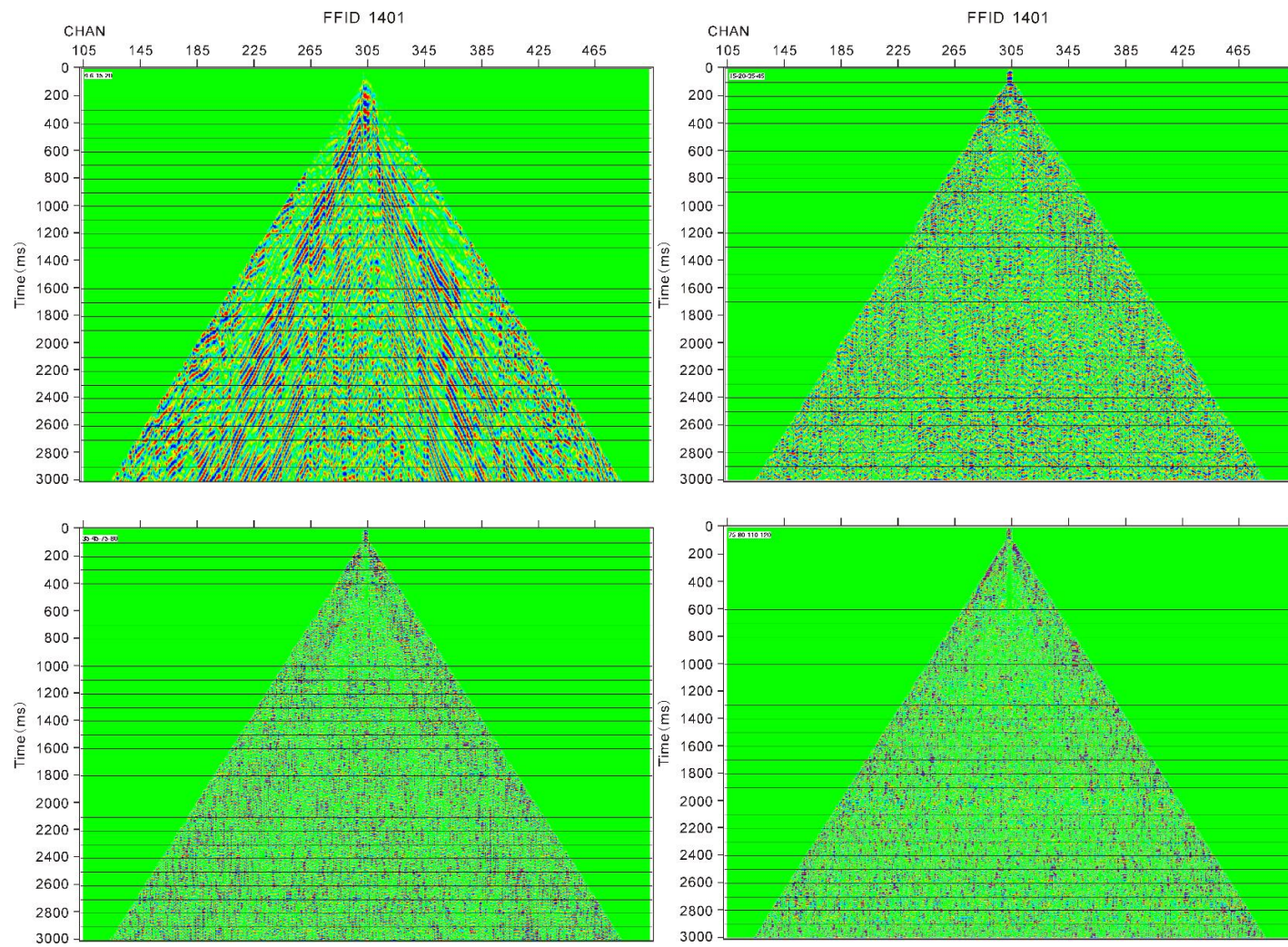


**Figure 6: Frequency decomposition in crossline component: 4-6-15-20, 15-20-35-45, 35-45-75-80 and 75-80-110-120Hz.**

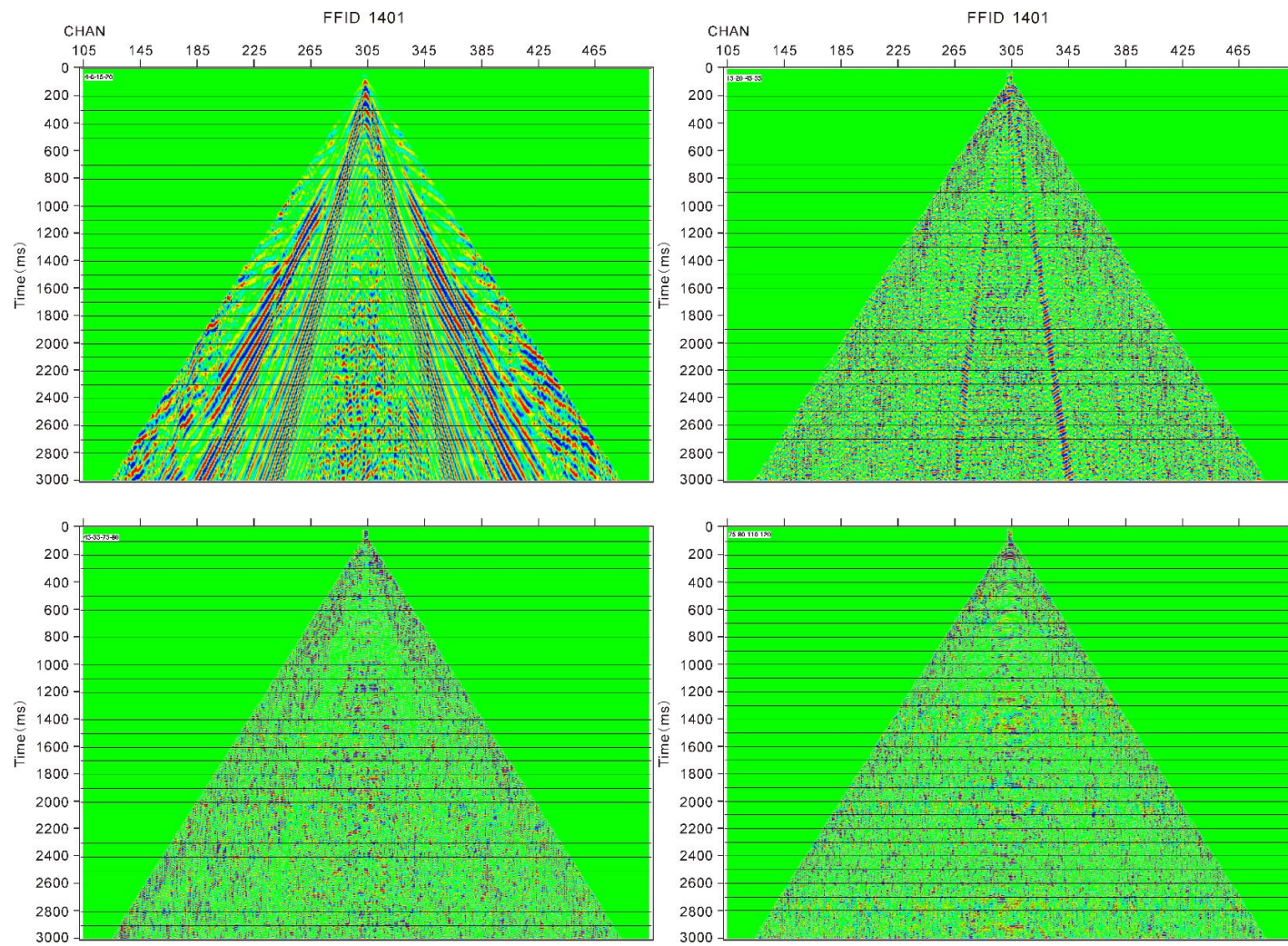


**Figure 7: Frequency decomposition in vertical component: 4-6-15-20, 15-20-45-55, 45-55-75-80 and 75-80-110-120Hz.**



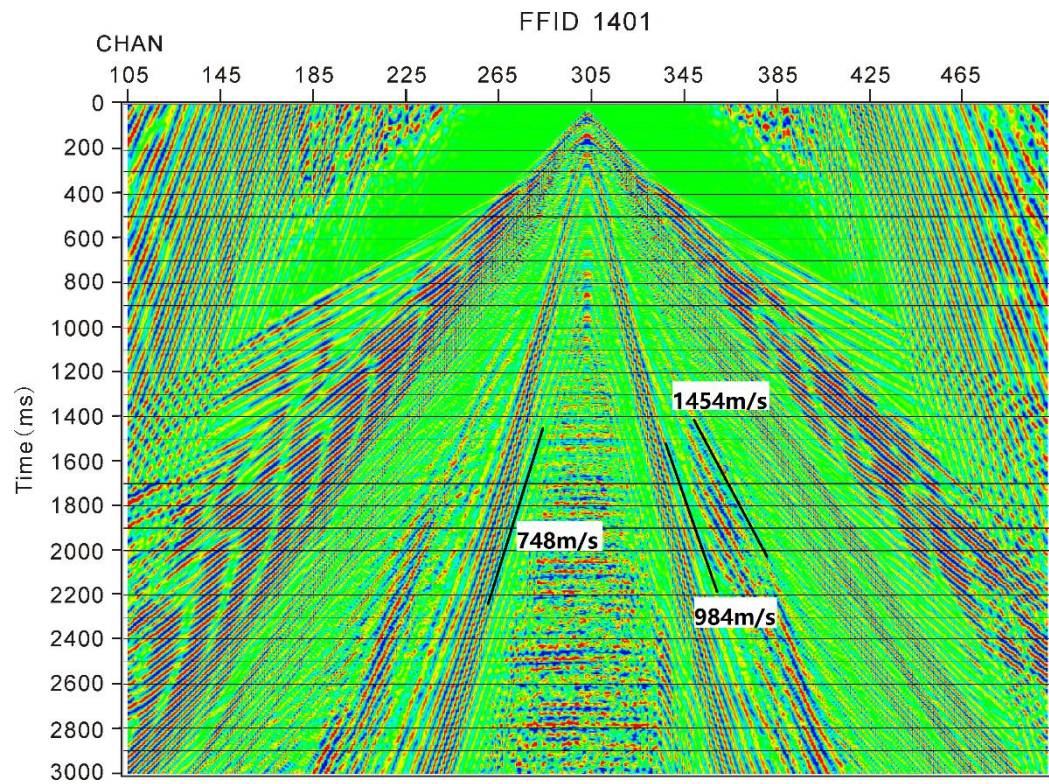


**Figure 8:** A portion of the raw shot record of pressure component illustrates the velocity range of surface waves.

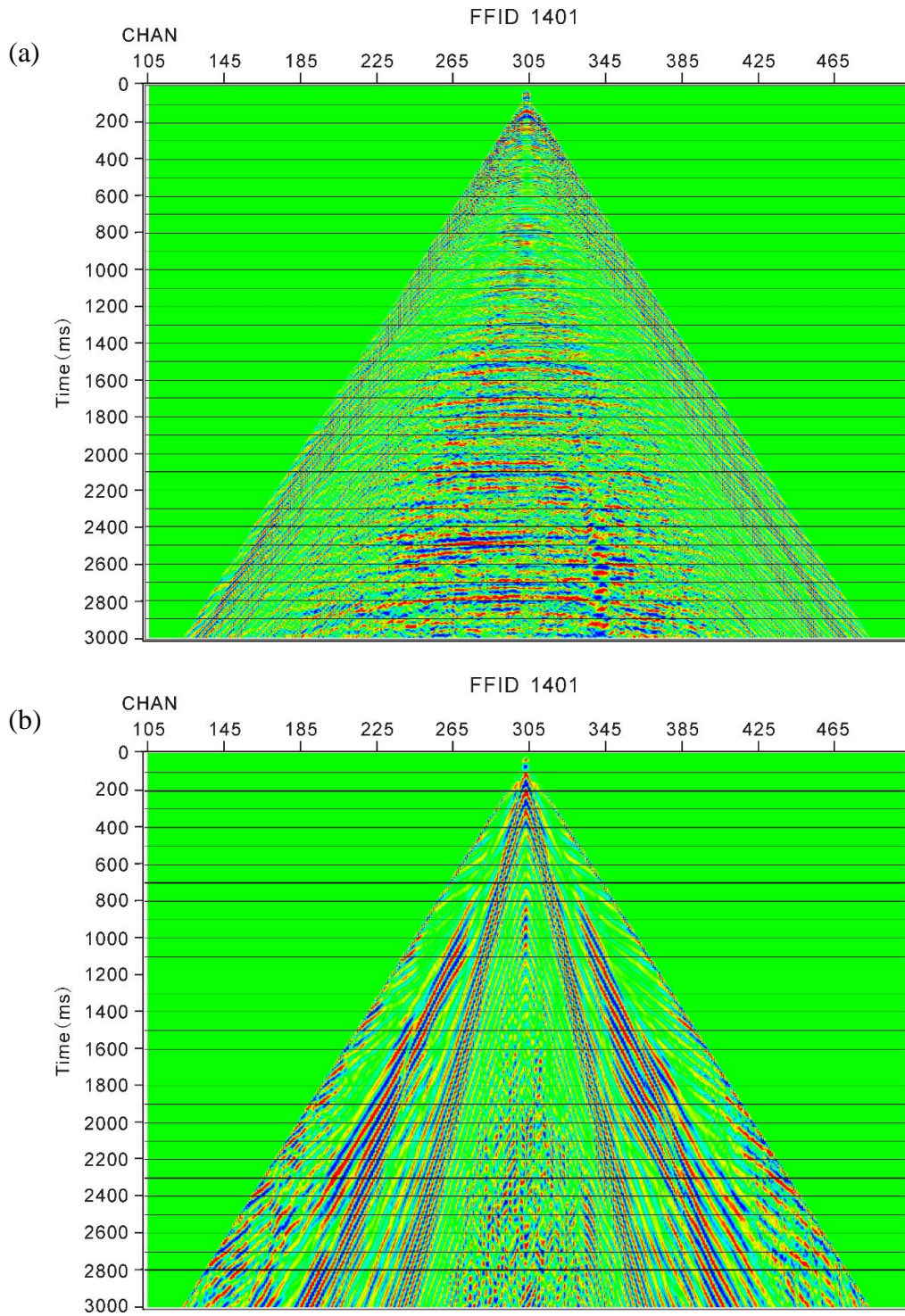


**Figure 9: After three Surface Wave Noise Attenuation filters: (a) a portion of the shot record of pressure component (b) a portion of extracted surface waves.**



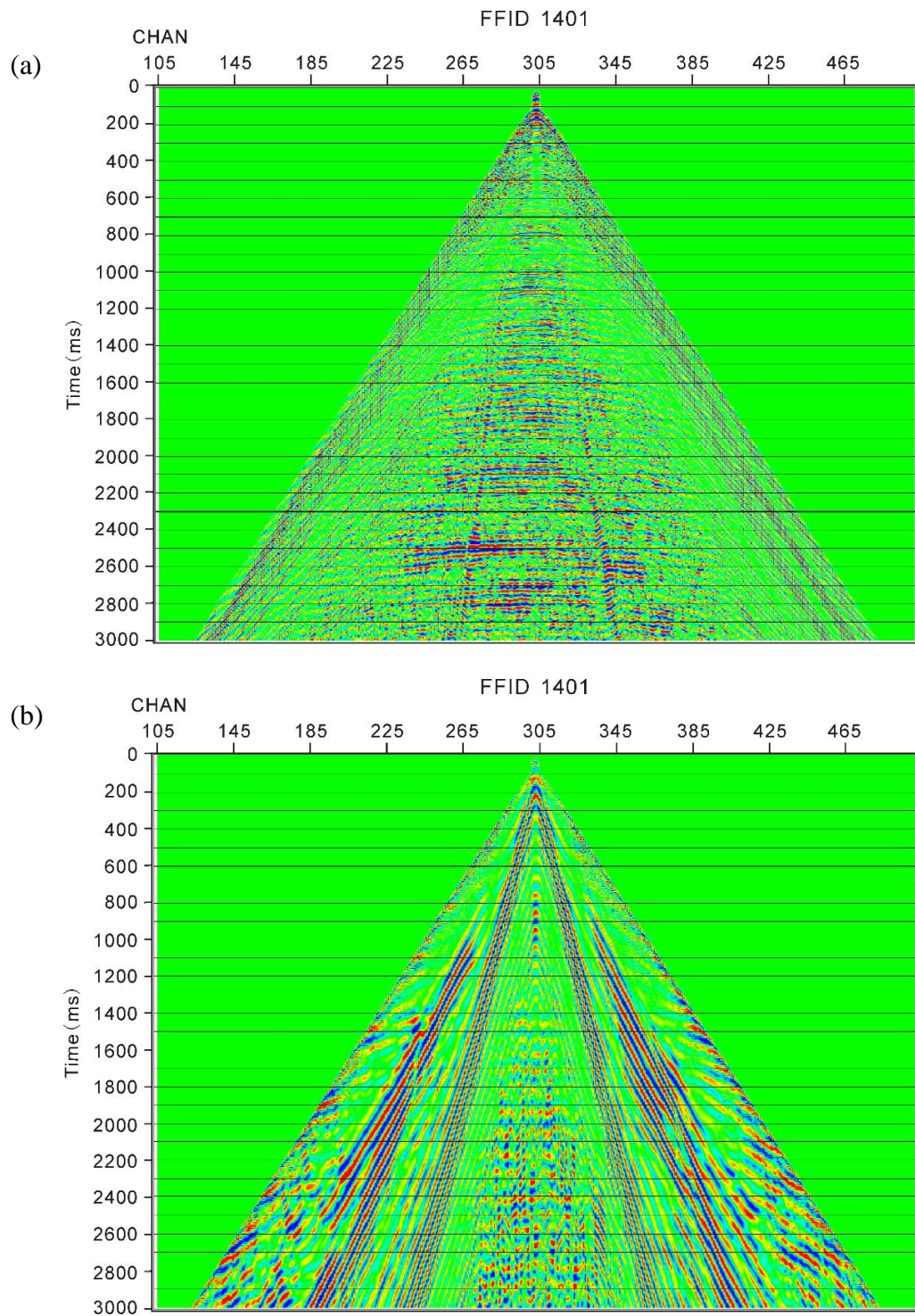


**Figure 10: After Bandpass Filter: (a) a portion of the shot record of pressure component (b) a portion of extracted surface waves.**



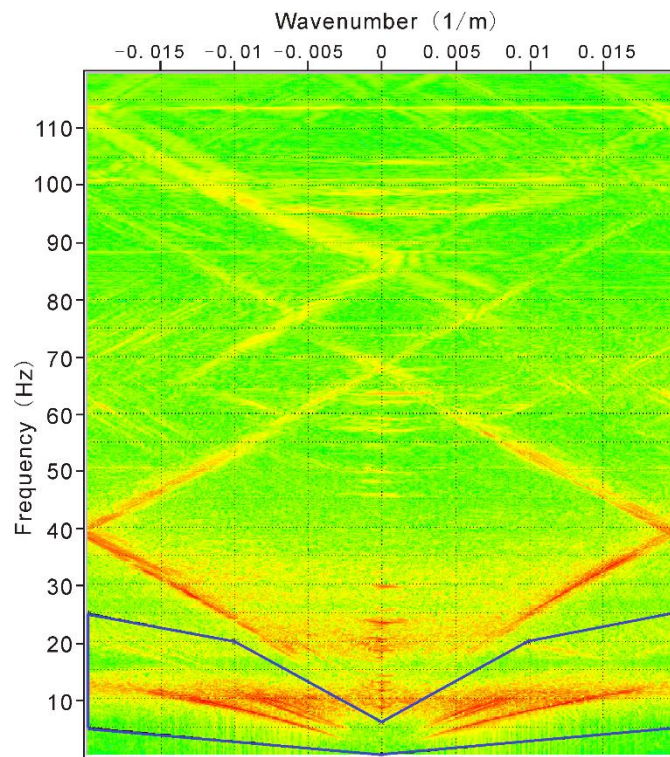


**Figure 11: Frequency-wavenumber spectrum of the pressure component shot record using 2D Fourier transform in which the blue polygon represents the rejecting zone.**

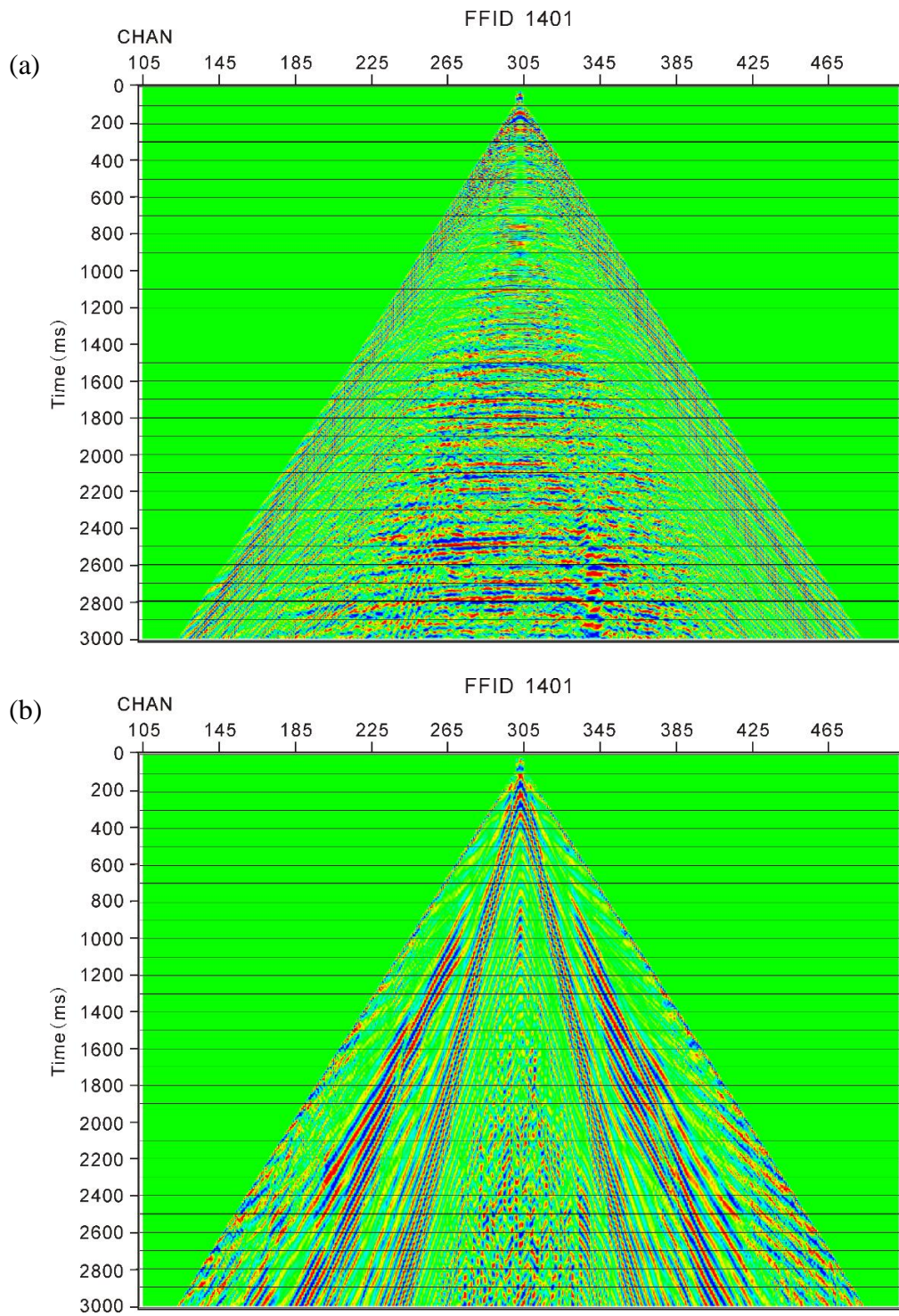


**Figure 12: After FK Filter when the polygon is rejected: (a) a portion of the shot record of pressure component (b) a portion of extracted surface waves.**

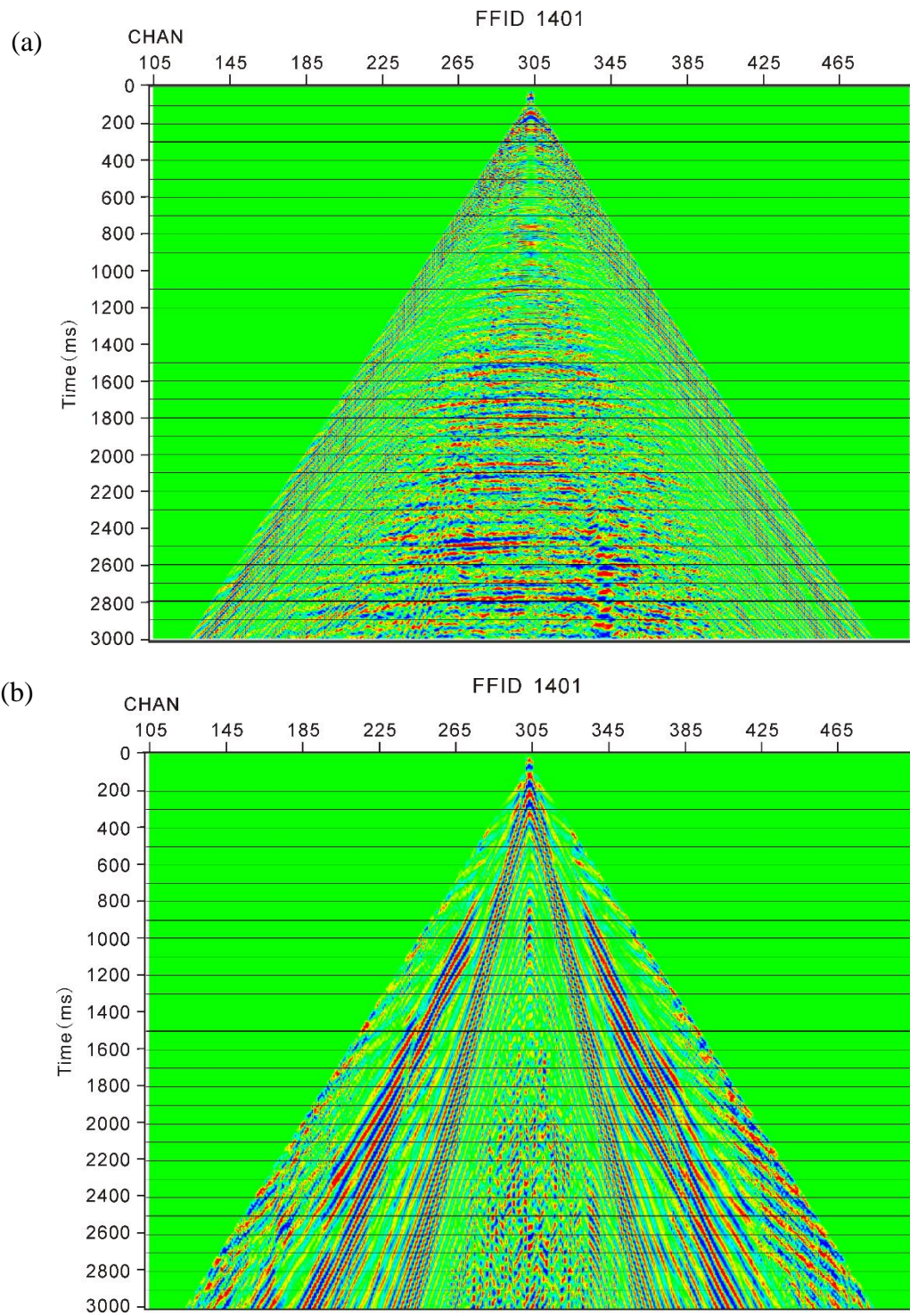


**Figure 13: After FK Filter when the polygon is accepted: (a) a portion of the shot record of pressure component (b) a portion of extracted surface waves.**

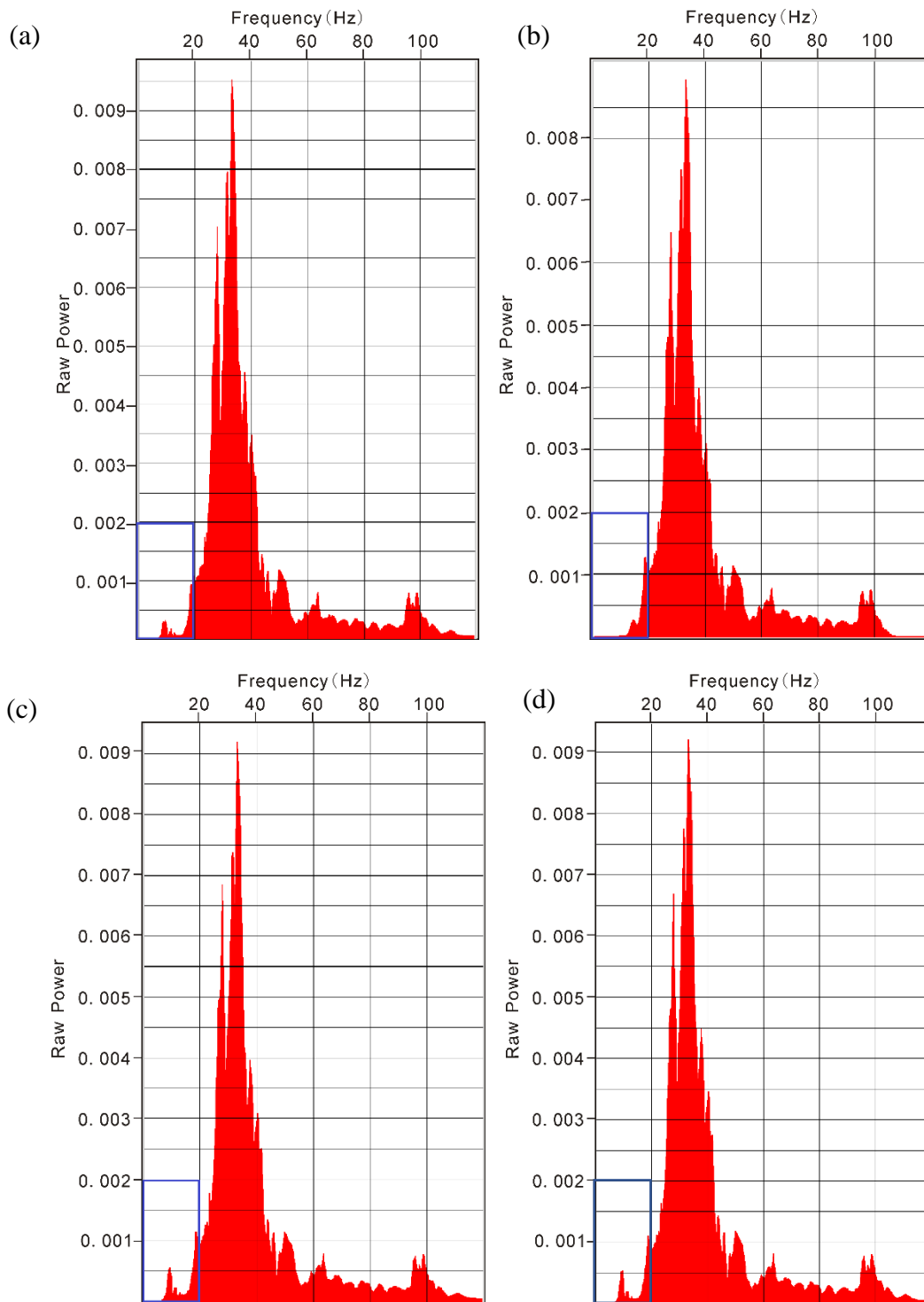


**Figure 14: Frequency spectra: (a) Surface Wave Noise Attenuation (b) Bandpass Filter (c) FK Filter (rejected) (d) FK Filter (accepted).**



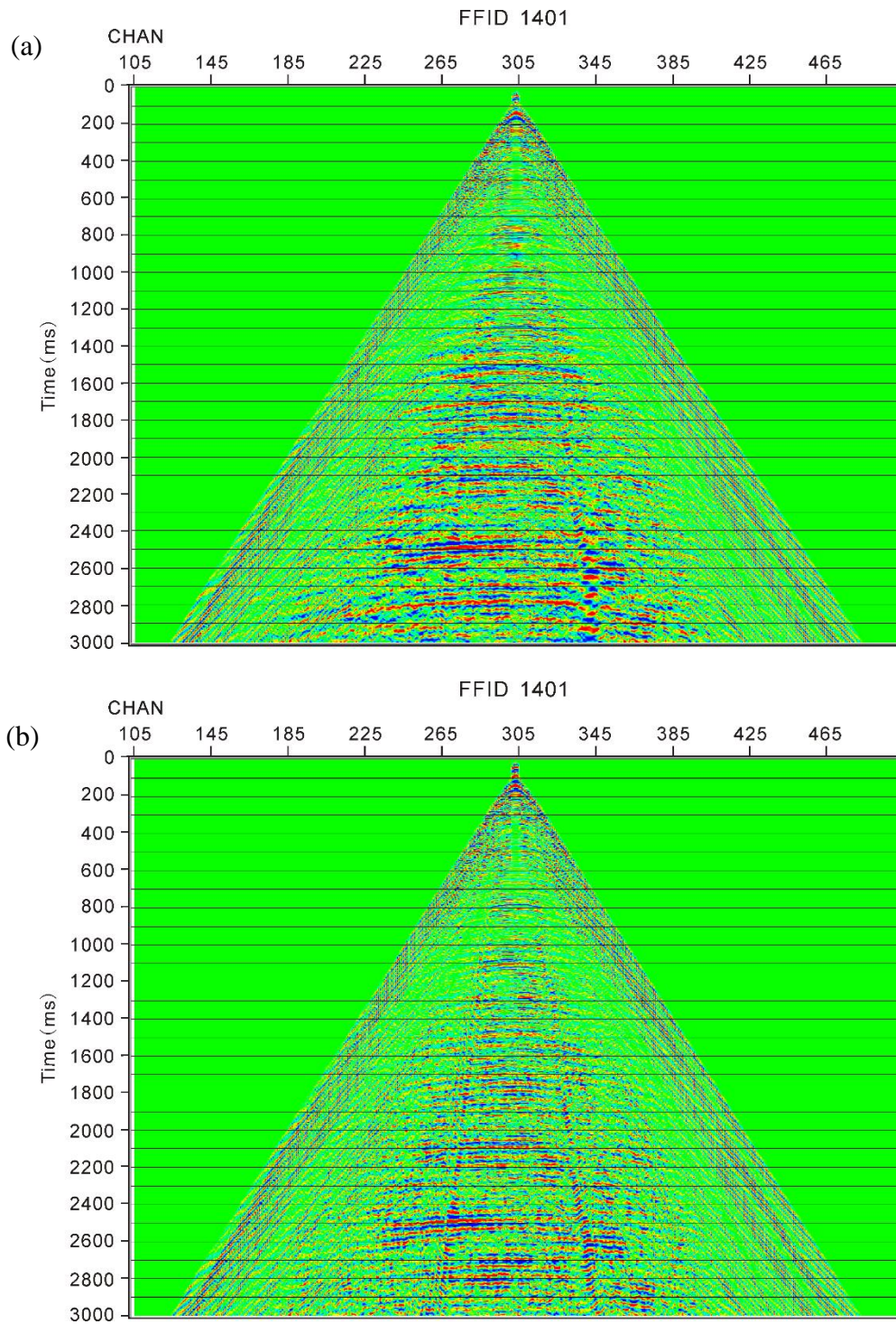


**Figure 15: Portions of the shot record of pressure component (a) After three Surface Wave Noise Attenuation filters (b)After Bandpass Filter (c) After FK Filter (rejected) (d) After FK Filter (accepted).**

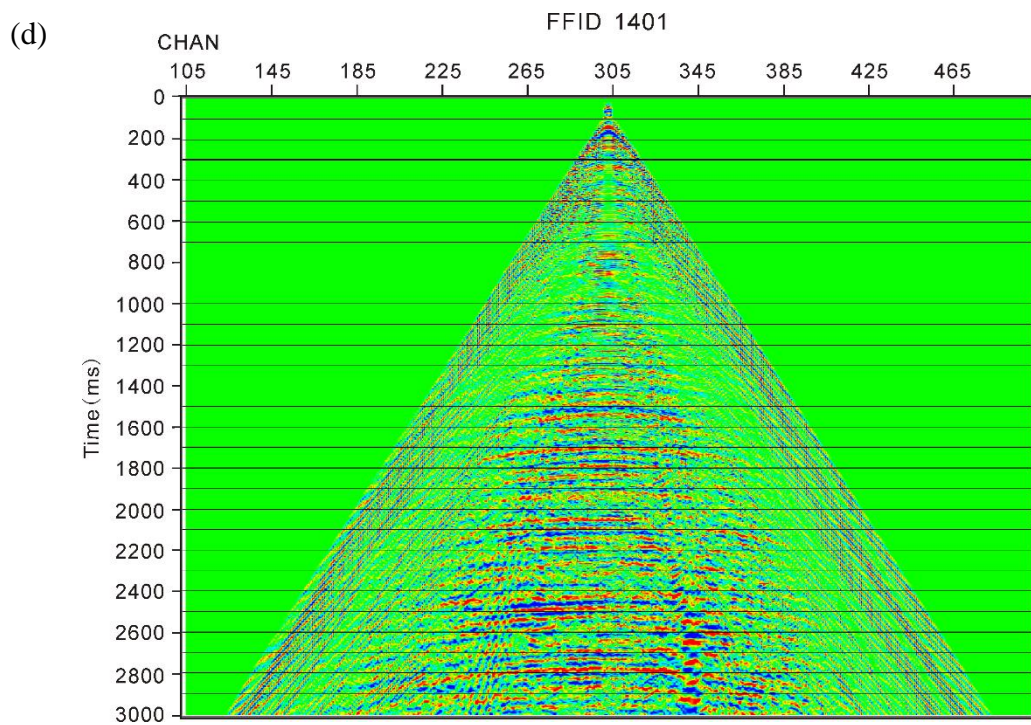
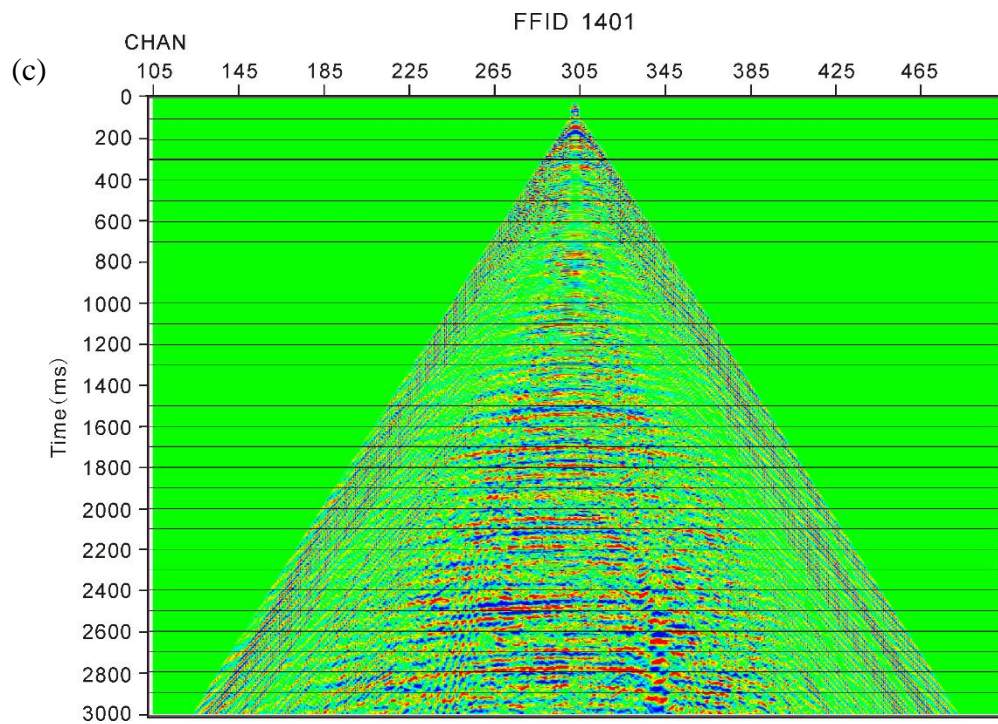


**Figure 15: Continued.**

### 3. SIGNAL ENHANCEMENT AND DATA PROCESSING

#### 3.1 Introduction

The purpose of seismic data processing is to image subsurface structures for geological interpretation and rock property analysis. Due to the advantages of shear waves, converted shear waves are increasingly applied for subsurface imaging and exploration (Stewart et al., 2003). The 4C OBC seismic data in the study area give rise to an opportunity to study converted shear-waves. Tatham and Goolsbee (1984) proposed the waveform conversion from P wave to S wave may happen at the seafloor. Johns (2006) gained P-S prestack time imaging by processing P-S waves converted from subsurfaces. Zhang et al. (2015) imaged the converted PS-S wavefield in the shallow-water environment. Based on the reflection coefficient for a P wave and the transmission coefficients for a P wave and a converted S wave, the S wave amplitude increases with the offsets, so the transmitted S wave energy can be one thousand times than the transmitted P wave energy at far offsets (Zhang et al., 2012). The conversion mode is very complicated, whether happen at the seafloor or at the subsurfaces. In this research, these two conversion modes (PS-S wave and PP-S wave) are analyzed separately in the 4C seismic data. Therefore, by obtaining P wave, PS-S wave and PP-S wave imaging, multicomponent data indeed can provide a more accurate description of subsurface structures than single-component data.

## **3.2 Literature Review**

### *3.2.1 Conventional P Wave Processing*

Yilmaz (2001) introduced the processing and applications of reflection seismic data for exploring oil or gas fields. In a homogeneous medium, wave energy decays as  $1/r^2$ , and wave amplitude decays as  $1/r$  ( $r$ -the radius of the wavefront). True amplitude recovery (TAR) is applied to compensate for the loss of amplitude due to the wavefront spreading and attenuation. Basic data processing sequences include: preprocessing, deconvolution, CMP sorting, velocity analysis, normal moveout correction, multiple attenuation, dip moveout correction, CMP stacking, poststack processing, migration and residual statics correction. For noise and multiple attenuation, there are various methodologies and filters mentioned, including Frequency-Wavenumber Filter, Radon Transform and Predictive Deconvolution. But all the theories and approaches are based on conventional single-component seismic data.

### *3.2.2 Converted Shear Wave Processing*

A converted P-S mode means a down-going P wave is converted to an up-going S wave at a reflector, so the down-going wave is faster than the up-going wave. Based on the Snell's law, the image point is located close to the receiver, instead of the midpoint. And the image points move closer to the receiver station as the reflection layer is closer to the seafloor. Therefore, Hardage et al. (2011) proposed common midpoint (CMP) imaging (Figure 16(a)) cannot be used when a P-S mode happens at a reflection layer, instead common-conversion point (CCP) imaging is applicable. The CCP stacking (Figure 17(a)) means a single vertical imaging trace in one stacking bin of the CCP



image space must be constructed by summing data from different time windows of all CCP traces that traverse the bin. The curved trajectory is positioned in several stacking binning (Figure 17(b)). Garotta et al. (1985) assumed the converted-points trajectory is aligned vertically, so the CCP trajectory is positioned in only one stacking binning, just like one stacking binning in CMP imaging (Figure 16(b)), which is called as an asymptotic binning.

### *3.2.3 Multi-Component Seismic Data Processing*

When multi-component seismic data are acquired as 2D data, Hardage et al. (2011) suggested 3D geophones can be deployed, so a consistent horizontal sensor is oriented parallel to the vertical plane along receiver stations. Due to the orthogonal-sensor design of 3D geophones, the horizontal sensor will be oriented perpendicular to this vertical plane. So, 2D shear-wave data record SH-SH and SV-SV displacements within this vertical plane or oriented orthogonal to this plane. Nonetheless, when multi-component seismic data are acquired as 3D profiles, it is essential to do a mathematical rotation of source and receiver orientation to define SH-SH and SV-SV waves. In this study, the 4C OBC data are 2D profiles, so it is irrelevant to rotate the inline/crossline record into the radial/traverse record.

Loewenthal et al. (1985) proposed the summation between the vertical record (Z) with the pressure record (P) is a common method to suppress noises, because these two records have the same polarity of up-going waves and the opposite polarity of down-going waves. This method is called as PZ summation. However, Zhang et al. (2015) recommended the OBC data in the shallow water environment record various types of

noises, which is difficult to fully achieve the advantages of the PZ summation. Thus, PZ summation is not performed in the study, due to the shallow-water environment.

Hardage et al. (2011) demonstrated the traces at negative and positive offsets have opposite polarities in inline component data. In addition, Sun et al. (2007) proposed the reflection signals of inline component vary with offset, due to the angle dependence of shear wave energy converted at the seafloor. Thus, Zhang et al. (2015) illustrated stacking the inline record directly may result in reflection cancellations, due to the phase changes with offsets. Because of the offset-direction dependence of velocity, P-SV data in 4C data are processed as two separate volumes in negative and positive offsets. Stacking velocities are calculated separately in these two data volumes, leading to two distinct stacking images. Then a sum of them can make a total-offset image. All three images are critical to interpret geological structures.

#### *3.2.4 Application of Shear Wave Imaging*

Stewart et al. (2003) concluded the applications of shear wave imaging, including a better subsurface imaging, lithology estimation, descriptions of fluid features, anisotropy characteristic analysis and potential reservoirs exploration. 1) P wave is sensitive to gas saturation, so reflections from interfaces within and below the gas-bearing channels are attenuated and poor. The P wave stacking result has gas chimneys. But S wave is insensitive to gas saturation, so converted wave can image through a gas cloud, and delineate interfaces within and below the channels; 2) Converted waves can improve the imaging of subsalt features and near-surface structures, because of larger S-wave impedance changes and shorter shear wavelength; 3) A sand/shale lithologic

boundary has a strong impedance contrast in shear wave, but little in P wave. So, there are anomalous amplitudes in P-S wave stack at boundaries of reservoirs, because of strong reflected converted wave and weak reflected P wave; 4) Shear waves are not affected by fluid contents. So, compared with a flat spot in P-wave stacking result, there are continuous dipping results in the converted-wave result, which represent a fluid contact between gas/oil with water.

### **3.3 Processing Flow and Methods**

The processing flow is proposed to remove surface waves, attenuate residual noises, enhance different wave modes and obtain stacked results in four-component data. The processing sequence for four components is the same, except the phase rotation in inline component data. Hardage et al. (2011) proposed the polarities of traces at positive and negative offsets in inline component data are opposite. Figure 18 shows the processing workflow for the pressure and inline component data in this research. 4C OBC seismic data are separated into pressure, inline, crossline and vertical component data. Then the geometry is loaded into the dataset.

#### *3.3.1 Surface Wave Attenuation*

Based on the surface wave analysis in Chapter II, the selected methodology to remove dispersive surface waves is Surface Wave Noise Attenuation, which is applied in both the shot and the receiver domain. Surface wave attenuation should be done before true amplitude recovery, because the amplitude correction is aimed to compensate the loss of energy as body waves spread.

### *3.3.2 Residual Noise Removal*

After separating surface waves from reflected signals, there are still refractions and spatial aliasing noises. Above the linear direct wave in shot gathers, there are linear refractions and Scholte waves from previous shots, contaminating the data strongly, so all the waves above the direct waves are muted in the shot domain. The direct waves travel from the airgun to receivers in the water column, so the velocity of direct waves is the water velocity (1480m/s). The traveltime of direct waves at the largest offset (around 5000m) is about 3.3s. To make it simple, the topmute window is 3.3s at the largest offset and 0s at zero offset. Next, F-K filters are applied in shot, receiver and CDP domains separately, to remove residual noises. After noise attenuation, the S/N value of the dataset has been increased a lot.

### *3.3.3 Wave Mode Enhancement*

The Hook's law gives a relationship between the displacements with the pressure variation. So, hydrophones and 3D geophones may record both P waves and converted S waves. The complex wavefields and strong multiples in the shallow-water environment create great baffles to identify primary velocities during the velocity analysis. Well log data do offer a good reference for the following velocity analysis. Based on the RMS velocity formula, interval P and S velocities in depth domain are transformed to RMS velocities in time domain. To calculate the converted P-S velocities, a statistic  $V_s/V_p$  value is essential. Figure 19 shows the P velocity-S velocity plotting from the log data, in which the slope of the trendline indicates the  $V_s/V_p$  value equals to 0.5125.

There are lots of wave types with hyperbolic features. To get P-wave stacking in pressure component data, P velocities from log are used to do normal moveout correction (NMO), which makes P wave reflections flat. After that, corrected up-dipping and down-dipping events are filtered out by a specific FK filter. Then, the same P velocities are applied to do inverse NMO. Figure 20 illustrates the processing sequences to preserve P-wave reflection signals. Through this workflow, only hyperbolas with similar P velocities are preserved in the pressure record. In the same way, converted PP-S waves and PS-S waves can be extracted from the pressure record separately.

#### *3.3.4 Velocity Analysis and Stacking*

After P wave enhancement in pressure record, P velocity analysis is done to get more accurate P velocities in the constrained velocity spectra. Using the refreshed P velocities to do NMO and stack, P stacked section in pressure component is obtained. Likewise, the PP-S wave and PS-S wave stacking velocities are analyzed, and their stacked sections can be gained in pressure component data. The 4C OBC seismic data provide the P wave, PP-S wave and PS-S wave stacked sections in four component data, so these three wavefields are processed and imaged by the same processing flow in the crossline and vertical component data.

According to the previous literature review, when the P-S conversion occurs at the sea bottom, the incident P waves propagate downward to the seafloor. Some can be reflected to the seawater column, some are transmitted to the solid strata as P waves, but some can be converted as S waves in the solid layer. Converted shear waves keep going downward to the subsurface reflectors and are reflected upward to the receivers at the

seafloor. The transmitted and converted S waves at the water bottom can be considered as secondary S-wave sources, so the wave paths of incident S waves generated by the secondary S-wave sources and reflected shear waves from subsurfaces are symmetric of the reflection points or midpoints. Ignoring the traveltime in the shallow water column, the converted points are along one vertical line in depth. So, the algorithm of common midpoint (CMP) stacking in traditional seismic data processing sequences can be applied to get the PS-S stacked sections. However, when the incident P waves keep propagating downward to the subsurface interfaces, the reflected and converted shear waves are recorded by the receivers at the seafloor. Because the incident P waves have different velocities from the reflected S waves, the reflected points are not located at midpoints. The conversion points depend on P-wave velocity, S-wave velocity and the reflector depth, so the reflected points change with depth along a curve. The converted point moves far away from the source with a decreasing depth. So, the common converted points (CCP) stacking algorithm is applied by calculating the conversion points coordinates.

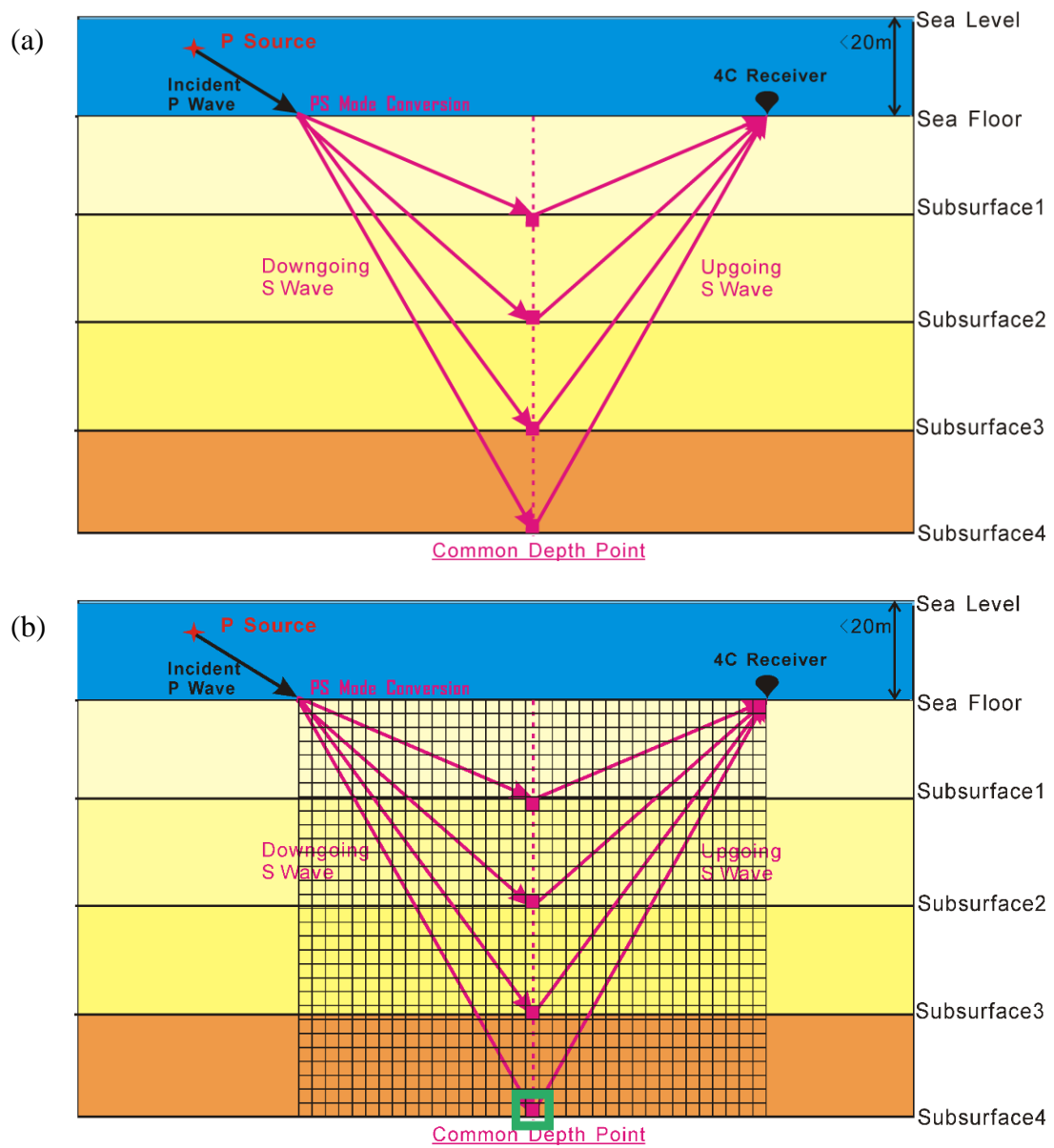


**Figure 16: PS-S waveform: (a) Raypath (b) Stack binning.**

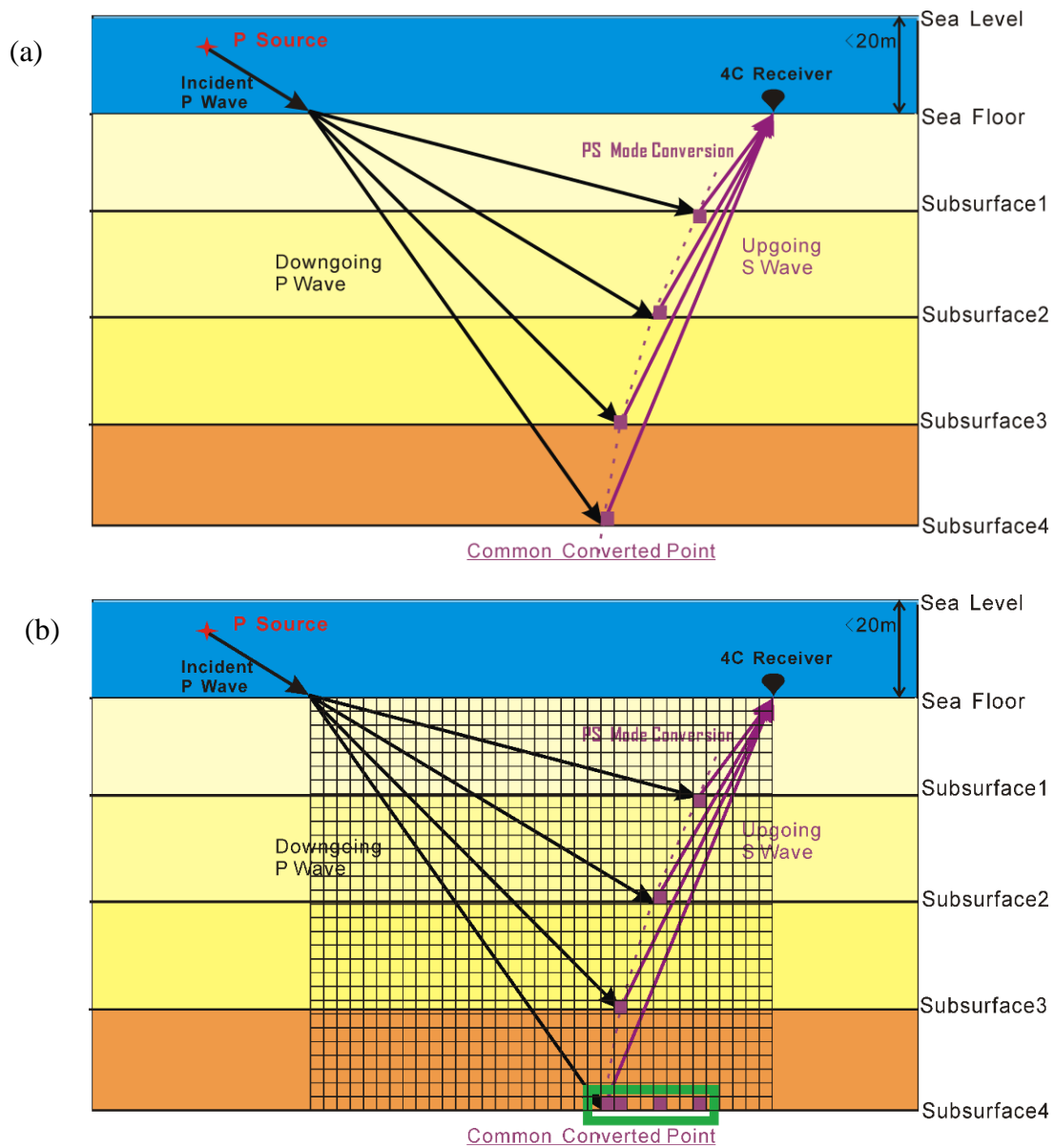


**Figure 17: PP-S waveform: (a) Raypath (b) Stack binning.**



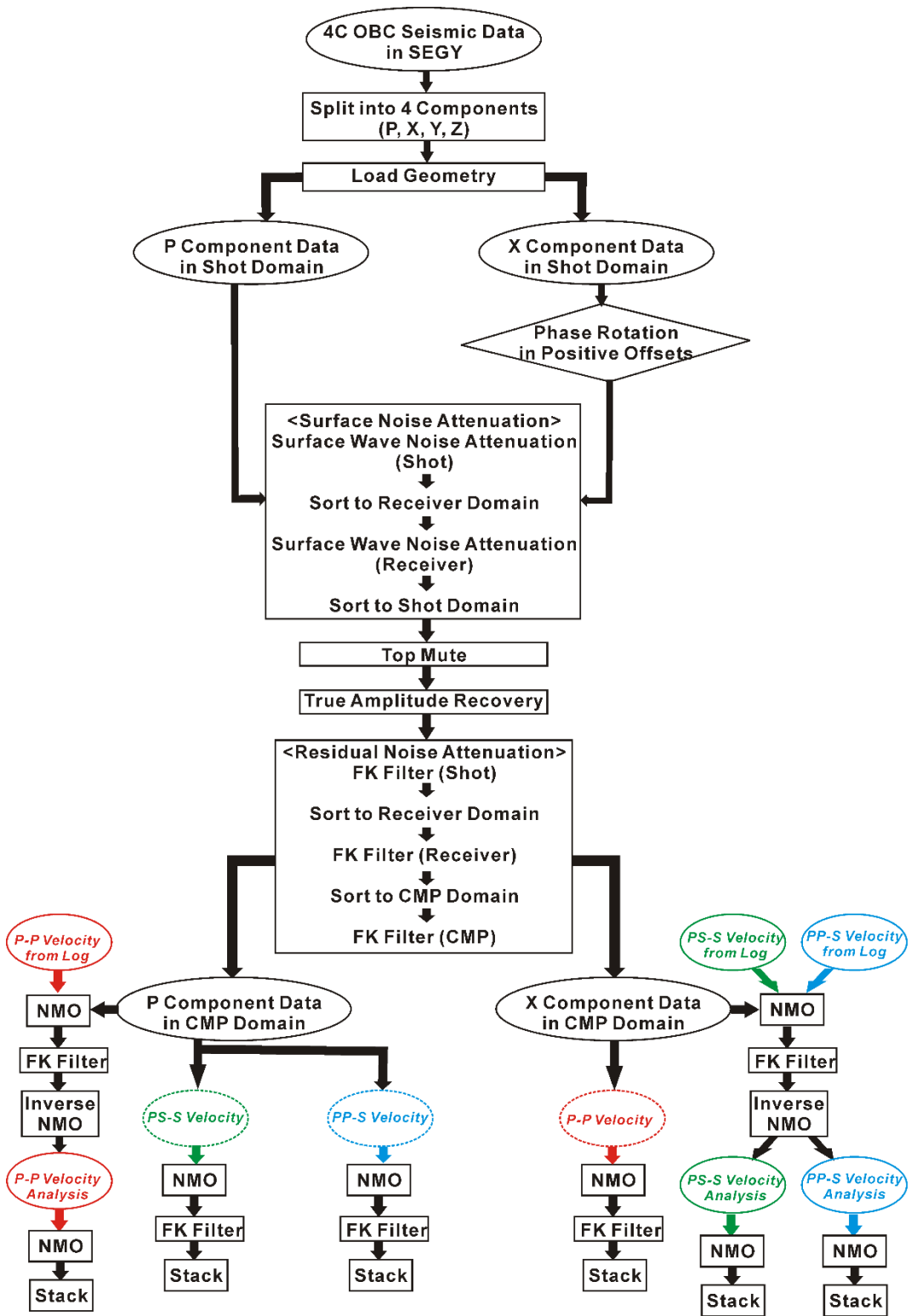
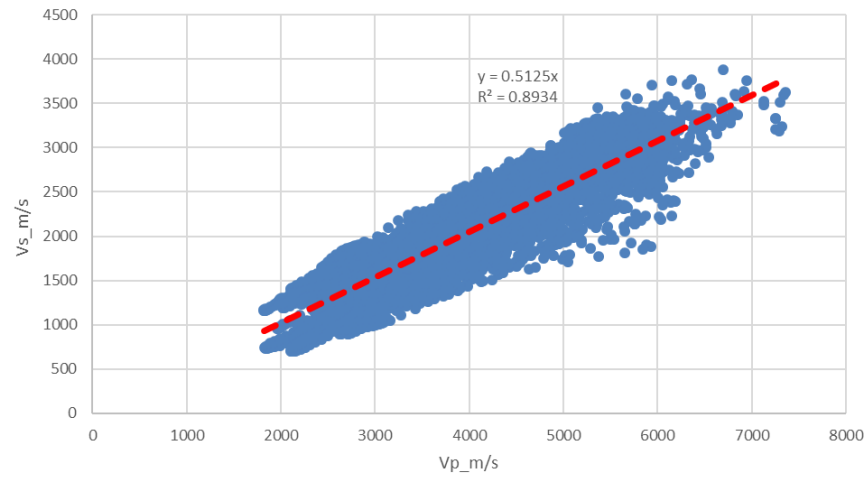
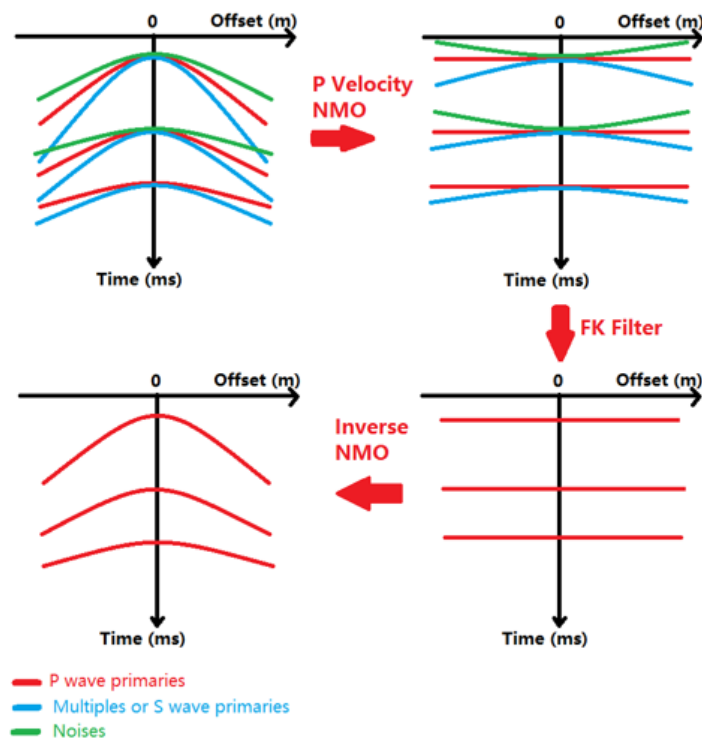


Figure 18: Pressure component and inline component data processing workflow.



**Figure 19: Illustrating the statistic  $V_p/V_s$  value from log data.**



**Figure 20: Processing sequences to preserve P wave reflection signals.**

### 3.4 Results

#### *3.4.1 Log Data Analysis and Velocity Model*

Well log data in Figure 21 include Gamma ray, bulk density, neutron porosity, effective porosity, water saturation, P-wave velocity, S-wave velocity and Vp/Vs ratio, which improve the potential reservoir estimation. The Gamma Ray Log is a continuous measurement of the natural radioactivity of the formations. Shales usually have higher radioactivity than other formations. The continuous low Gamma ray values around 25API in Figure 21 indicate the formations from C800m to C890m are sands. In the Density-Neutron Log, on a limestone scale, there are high neutron porosity values from C770m to C800m, which mean shale effects on NPHI. Because shales have bound water, the neutron tool responds to the presence of hydrogen in the bound water of shales. However, in the Effective Porosity Log, there is no respond to shales, because the water is immobile, and does not represent the effective porosity. In the Water Saturation Log, the water saturation is around 50% from C800m to C825m, but it becomes 100% from C825m to C890m. Therefore, the log data indicate that the potential reservoir starts from the C800m depth, and its thickness is about 25 meters.

In addition, well log data include the P-wave and S-wave logs. Via the RMS velocity formula, the instant Vp and Vs in the depth domain can be transformed to RMS velocities in the time domain, which provide a great reference for the velocity analysis. And Vp/Vs values along the depth can be calculated from sonic log data, which are necessary to locate the converted points in converted wave processing.

Table 1 shows the velocity model built from the log data and the geological background in this research area. The well depth is up to D116m, so above the red line in Table 1, P wave and S wave velocities are from well log data. But beneath the well, velocities can be estimated based on the rock properties of formations. For example, rocks in the formation Maaddud are limestones, which have high velocities ( $V_p=6340\text{m/s}$  and  $V_s=3270\text{m/s}$ ). But there are shales in the formation Nahr Umr, which have lower velocities ( $V_p=3810\text{m/s}$  and  $V_s=1880\text{m/s}$ ). Besides the P velocity and S velocity model, the P-S velocity model along the depth is created on  $V_p$ ,  $V_s$  and their statistic ratio ( $V_p/V_s=1.95$ ).

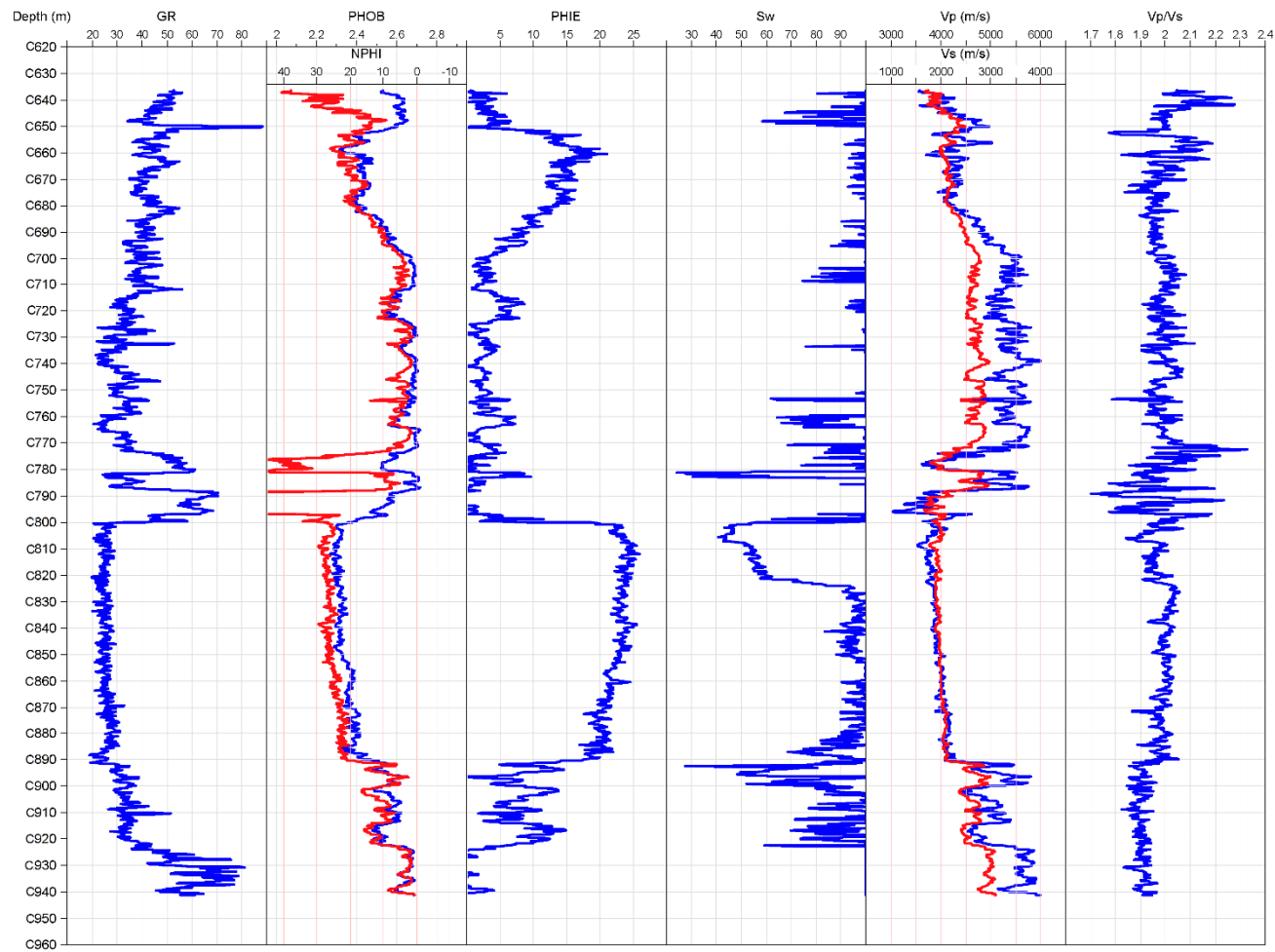


**Figure 21: Gamma ray, density (blue) & neutron porosity (red), effective porosity, water saturation, P (blue) & S (red) velocity, and Vp/Vs (from left to right) at the depth C636.52m-C941.32m from the Well B.**

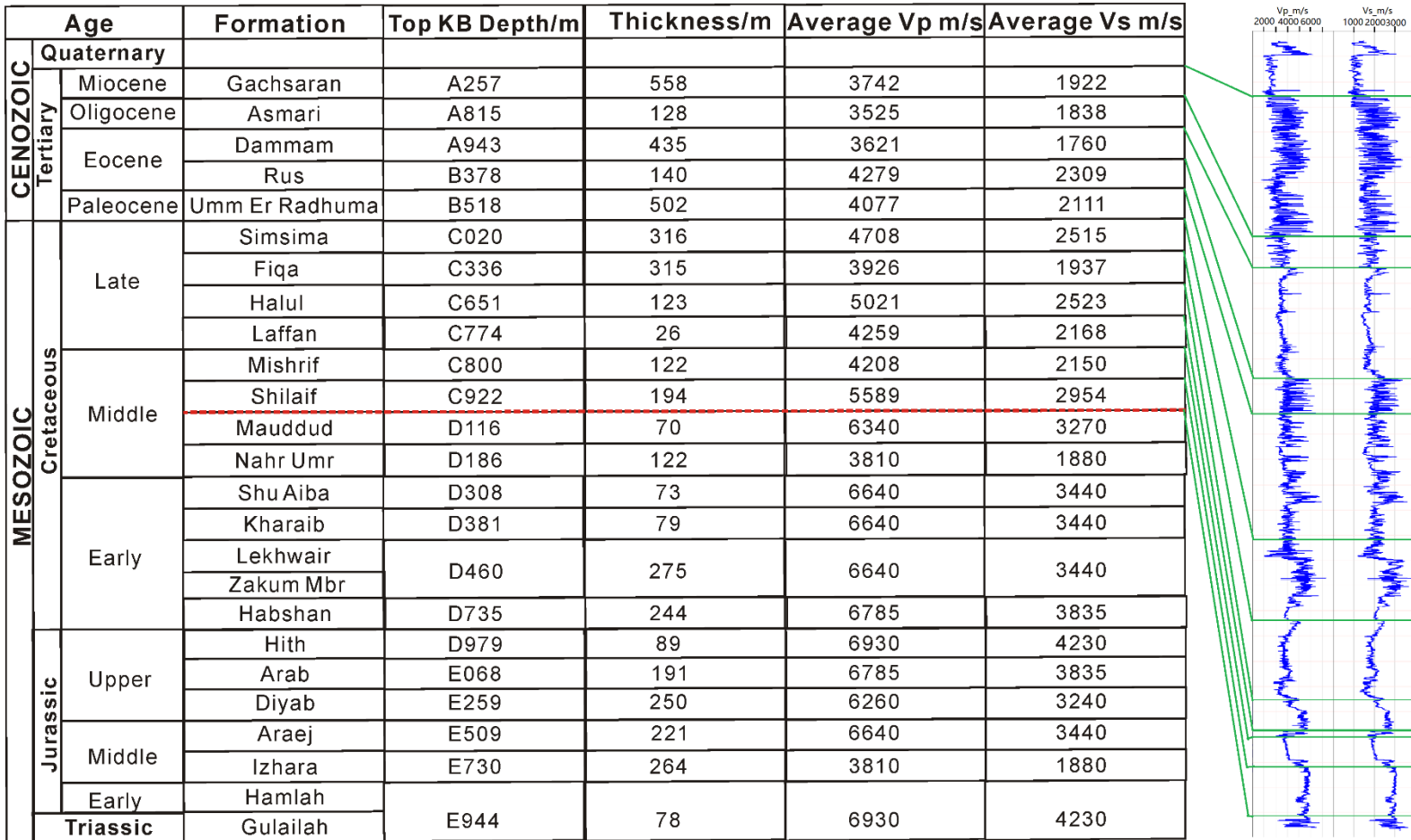


**Table 1: Velocity model based on sonic log data and geological background.**

### *3.4.2 Surface Wave Attenuation Results*

Based on the designed processing flow, the first task is to suppress strong linear surface waves shown in the raw shot gathers (Figure 22), covering reflected signals in pressure component. As discussed in Chapter II, the Surface Wave Noise Attenuation method uses surface wave velocities and the cut-off frequency to suppress surface waves in F-X domain. Figure 23 shows the shot gather after three Surface Wave Noise Attenuation filters, which indicates linear Scholte wave suppression and hyperbolic signal enhancement. Scholte waves are recorded by detectors, so when sorting the data from the shot domain to the receiver domain, there exist coherent surface waves again shown in Figure 24. The same approach is applied to receiver gathers to suppress surface waves, and the result in Figure 25 indicates Surface Wave Noise Attenuation also works well in the receiver domain. After the second round of surface wave suppression in receiver domain, there are more clear and continuous reflection events (Figure 26(b)), compared with the shot gather (Figure 26(a)) only after one round suppression in shot domain.

The processing sequence is the same in four component seismic data, except a phase rotation in inline component data. Figure 27(a) shows the polarities of traces at positive and negative offsets are opposite in inline component data. After the phase rotation at positive offsets, the result is shown in Figure 27(b). Figure 28 shows the shot record of inline component after phase rotation, in which there are noises without any sign of useful signals. Same as the pressure component data, the Surface Wave Noise

Attenuation filters are applied to both the shot and the receiver domain. The shot record after suppressing surface waves is shown in Figure 29.

### *3.4.3 Residual Noise Removal Results*

There still exist residual noises in the shot gather at far offsets after removing surface waves, shown in Figure 26(b). Then, two fan filters in different ranges of frequencies are used to remove residual noises, including refractions and spatial aliasing noises. Compared with the raw shot record in Figure 22, the shot gather after FK filter in Figure 30 obviously shows more continuous reflection signals. Because random noises exist in different domains, FK filtering is also implemented in receiver and CDP domains to improve the S/N ratio. After several rounds of noise attenuation, Figure 31 shows the preprocessed CDP gather, which can be used to do the following processing sequences. There are some empty traces of the pressure record in receiver and CDP domains. That's because there are only 96 channels in Shot 1179. When shot gathers are sorted to other domains, there will be some empty traces from this shot gather.

Likewise, although strong surface waves have already been removed in inline component, the exposed hyperbolic reflections are still weak, unclear and discontinuous, because of the uncertain direction of geophones. To remove residual noises, the same FK filters are applied in the shot domain (Figure 32). Then, by applying FK filters to the receiver and the CDP domain, the final preprocessed CDP gather is shown in Figure 33, in which hyperbolic reflections have appeared. Though the reflection signals recorded in inline component data (Figure 33) are not good as pressure component data (Figure 31),



the signal-to-noise ratio of inline component data has been improved a lot via following the preprocessing sequences.

In the same way, Figure 34 and 35 show the processed CDP records in crossline and vertical component data. In crossline component, due to the physical measurement, the reflection signals are not consistent in the CDP record. Because of the energy leakage, the vertical record is also influenced by the noisy crossline data (Zhao et al., 2015). So, the hyperbolic reflections in the CDP record of vertical component data (Figure 35) are less continuous and clear than the pressure component CDP record (Figure 31).

To analyze the signal-to-noise ratio before and after the noise attenuation in four-component seismic data, the frequency spectra of the raw shot record and the preprocessed shot record are studied. First, in pressure component data, the frequency spectrum of the raw shot record (Figure 36(b)) illustrates the energy of 10Hz (the dominant frequency of Scholte waves) is four times more than that of 20Hz (the dominant frequency of signals). After the preprocessing sequences, the frequency spectrum (Figure 36(d)) shows the energy of signals becomes around three times than that of surface noises. Figure 37(b) and (d) are the frequency spectra of the raw record (Figure 37(a)) and the preprocessed record (Figure 37(c)) of inline component data. The signal-to-noise energy ratio in the raw data is about 0.17; and it becomes to 2 after noise attenuation. In the same way, the energy ratio of the raw shot record in crossline component is 0.05; by following the preprocessing flow, the energy ratio grows into 2.7. Although the S/N increases in crossline component data, there is fewer reflection in the

shot record (Figure 38(c)). Figure 39 indicates the energy ratio in vertical component increase from 0.03 to 0.77 by the same sequences, which improves the S/N of vertical component is less than that of pressure or inline component. Additionally, compared with other three components, the dominant frequency of signals recorded by vertical geophones is larger than 20Hz, which is around 30Hz. Therefore, the signal enhancement in all four-component seismic data are verified by the quality of shot records as well as the quantity of signal-to noise energy ratio.

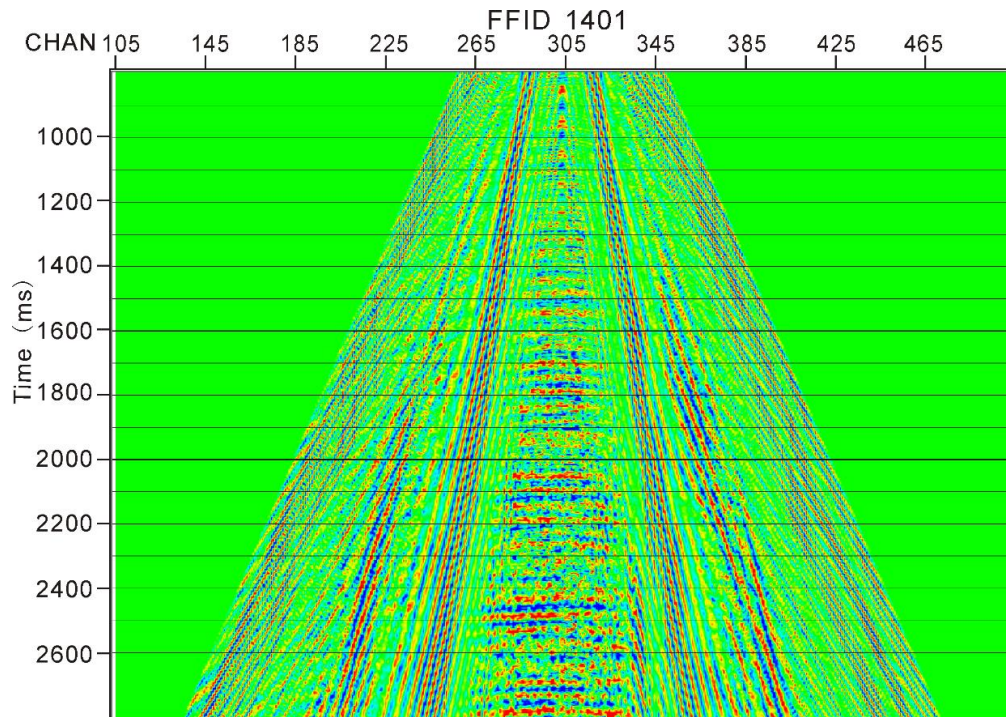


**Figure 22: A portion of the raw shot record of pressure component.**

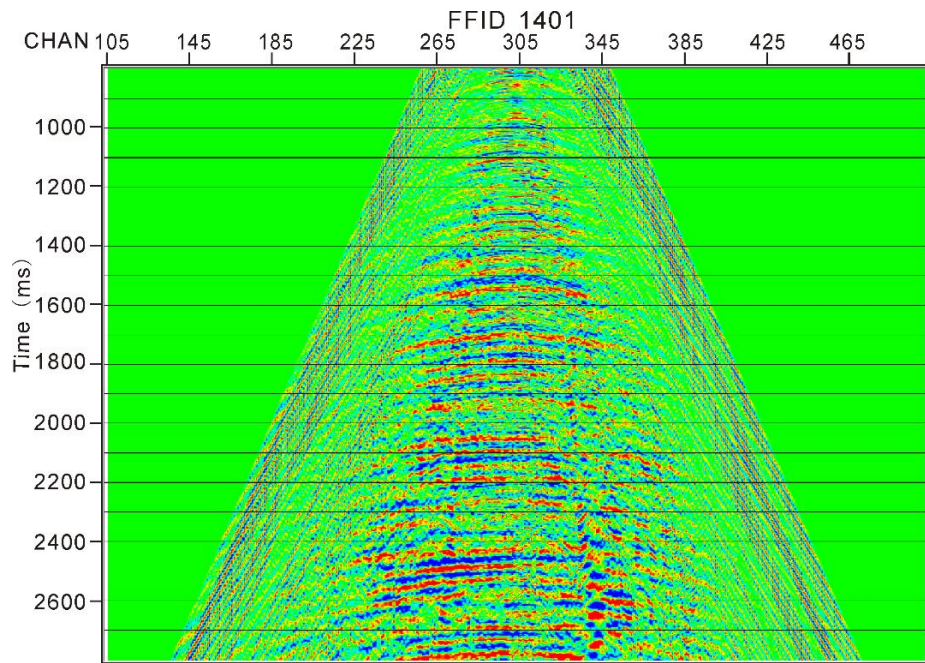


**Figure 23: After three Surface Wave Noise Attenuation filters, a portion of the shot record of pressure component.**

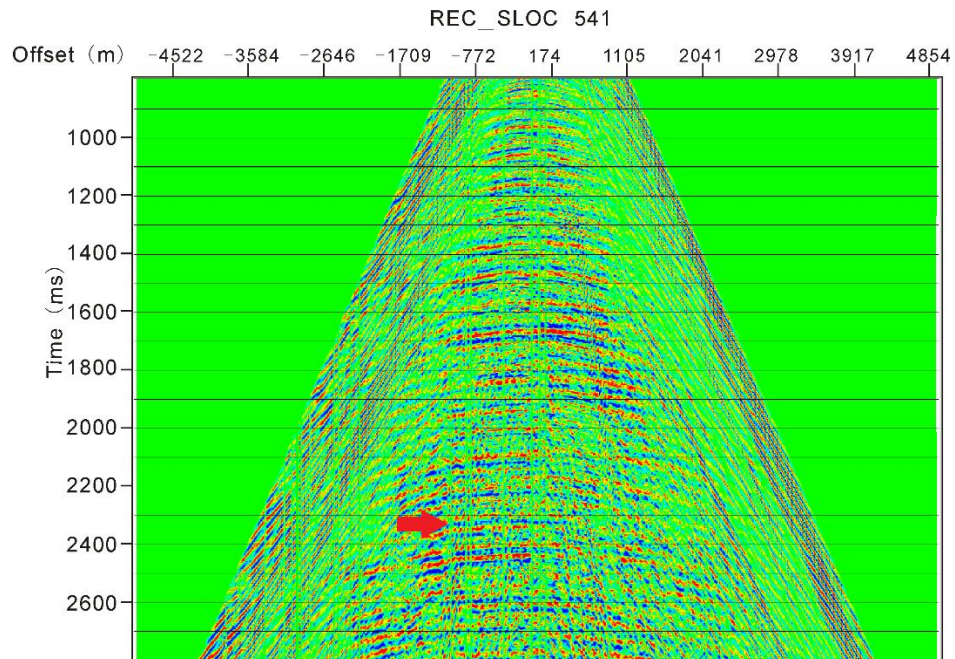


**Figure 24: After sorting to the receiver domain, a portion of the receiver record of pressure component, showing residual surface waves.**

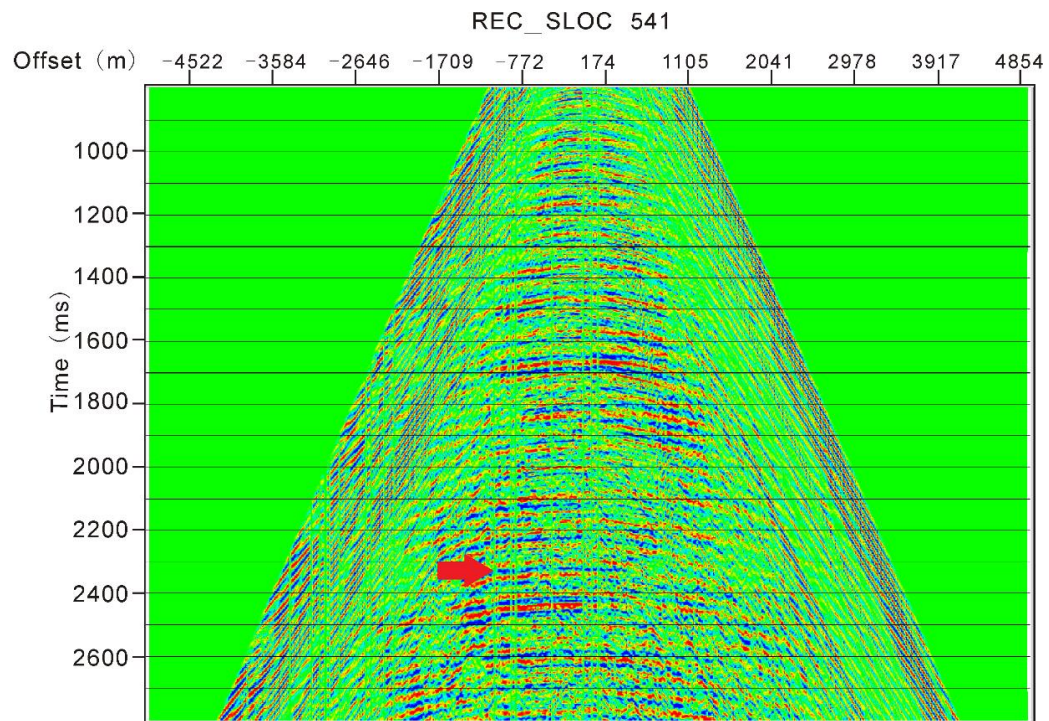


**Figure 25: After three Surface Wave Noise Attenuation filters, a portion of the receiver record of pressure component.**



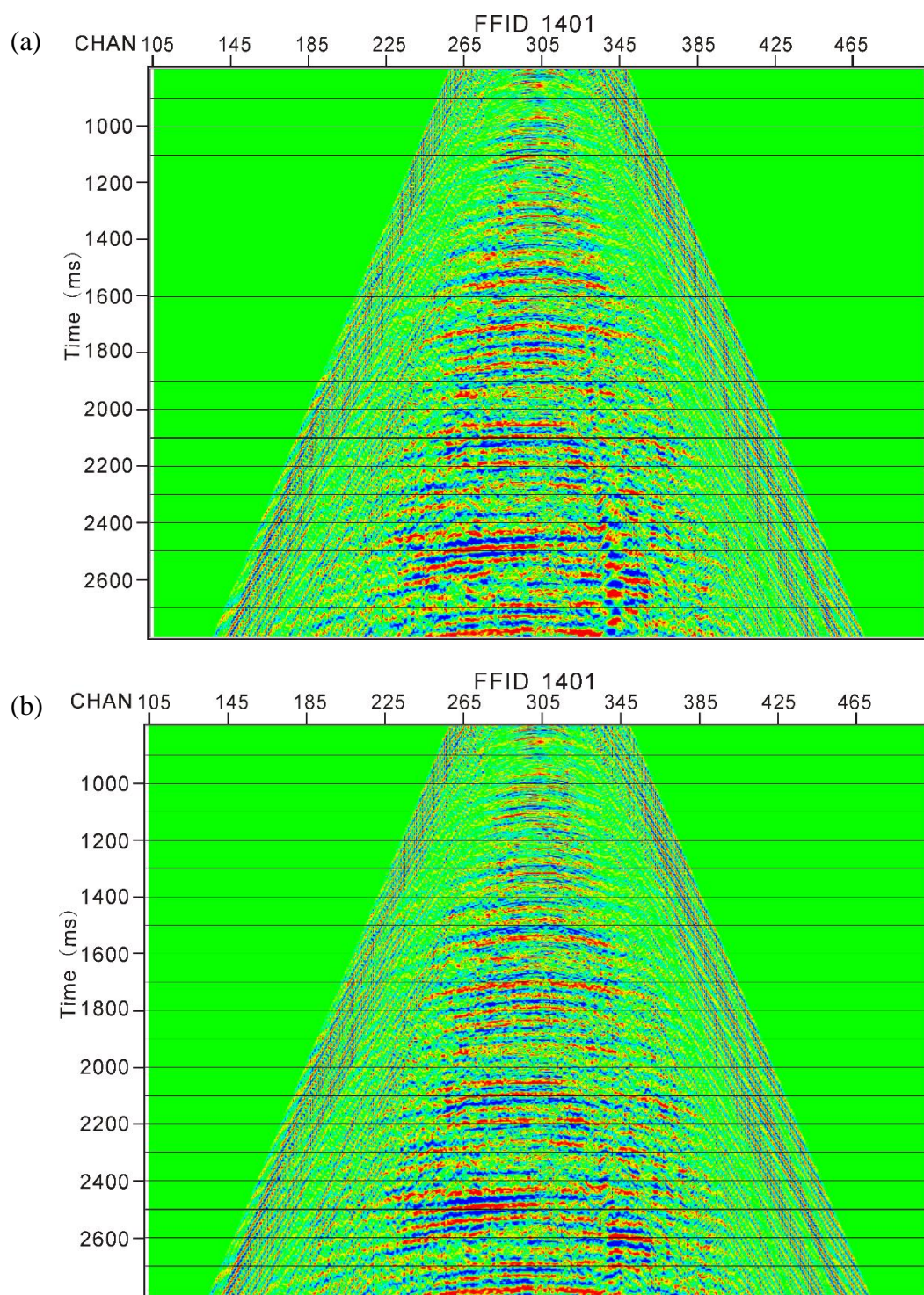


**Figure 26: (a) Same as Figure 23 (b) After sorting to the shot domain, a portion of the shot record of pressure component.**

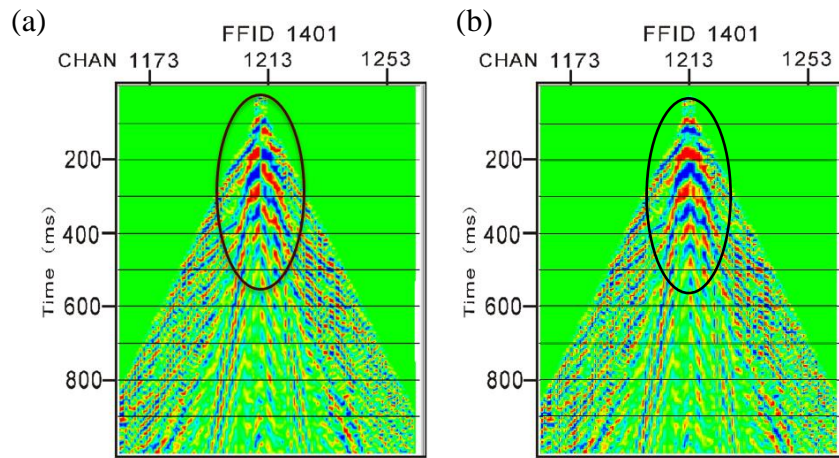


**Figure 27: A portion of the raw shot record of inline component (a) Opposite phases between positive offsets with negative offsets (b) After phase rotation in positive offsets.**

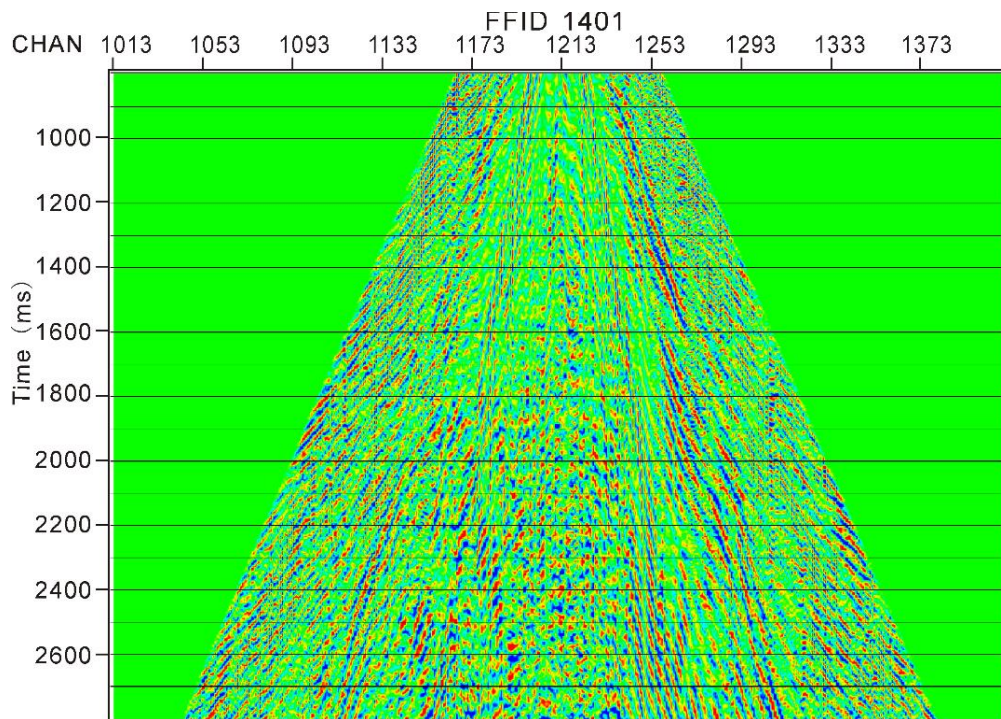


**Figure 28: After phase rotation, a portion of the shot record of inline component.**



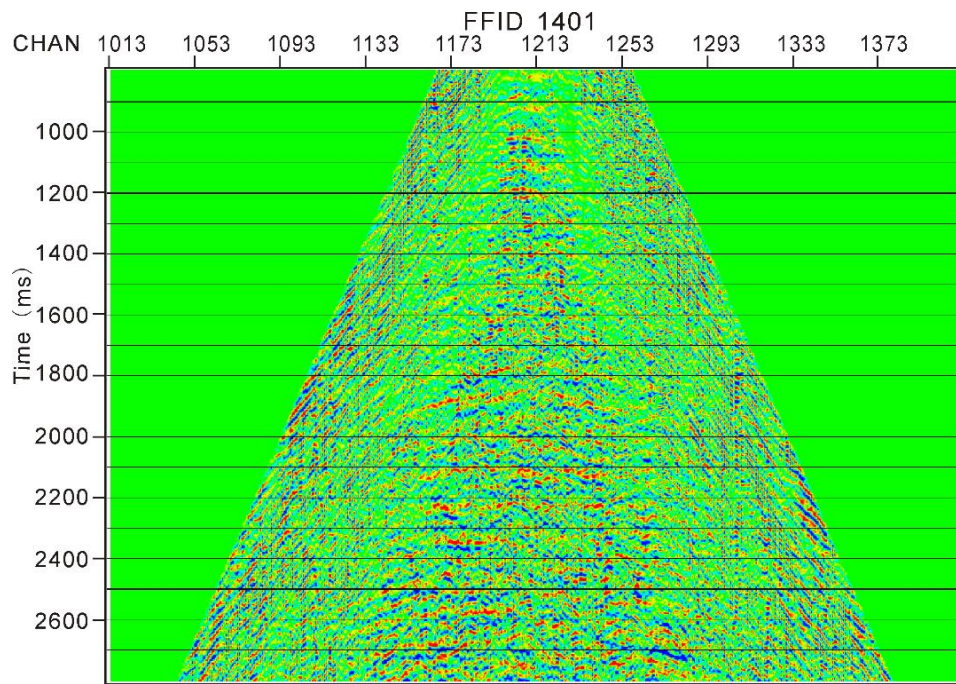


**Figure 29: After the same flows to remove surface waves, a portion of the shot record of inline component, showing residual noises.**

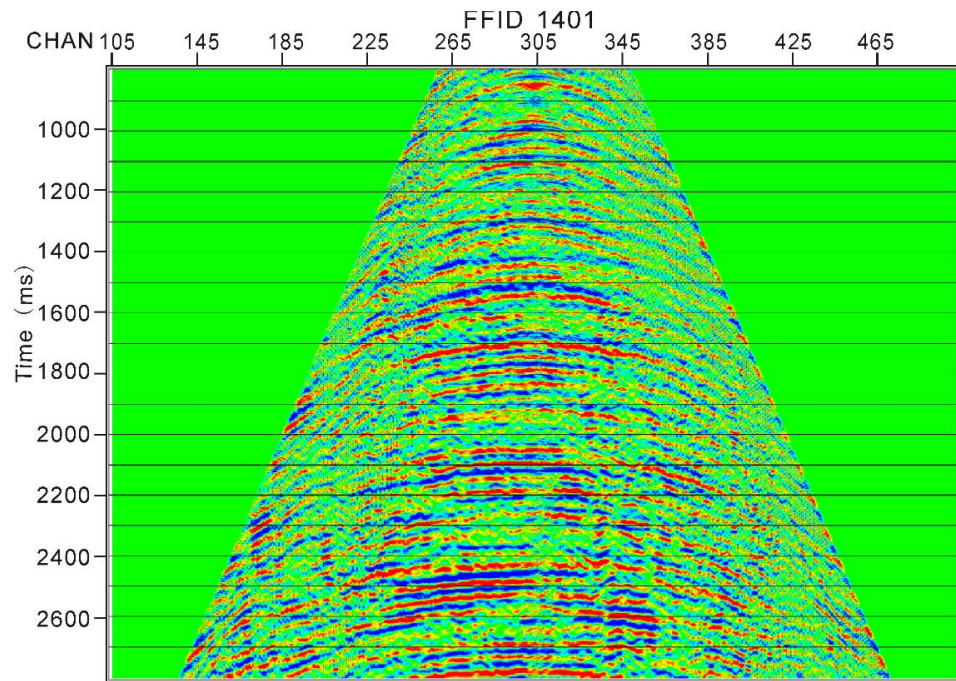


**Figure 30: After FK Filter, a portion of the shot record of pressure component.**

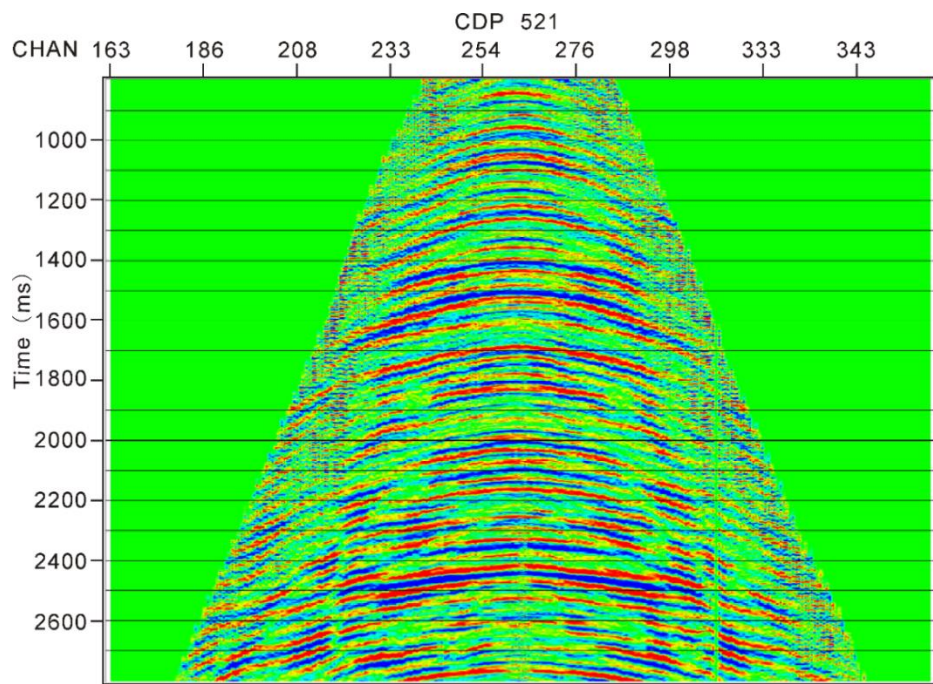


**Figure 31: After removing residual noises, a portion of the CDP record of pressure component.**

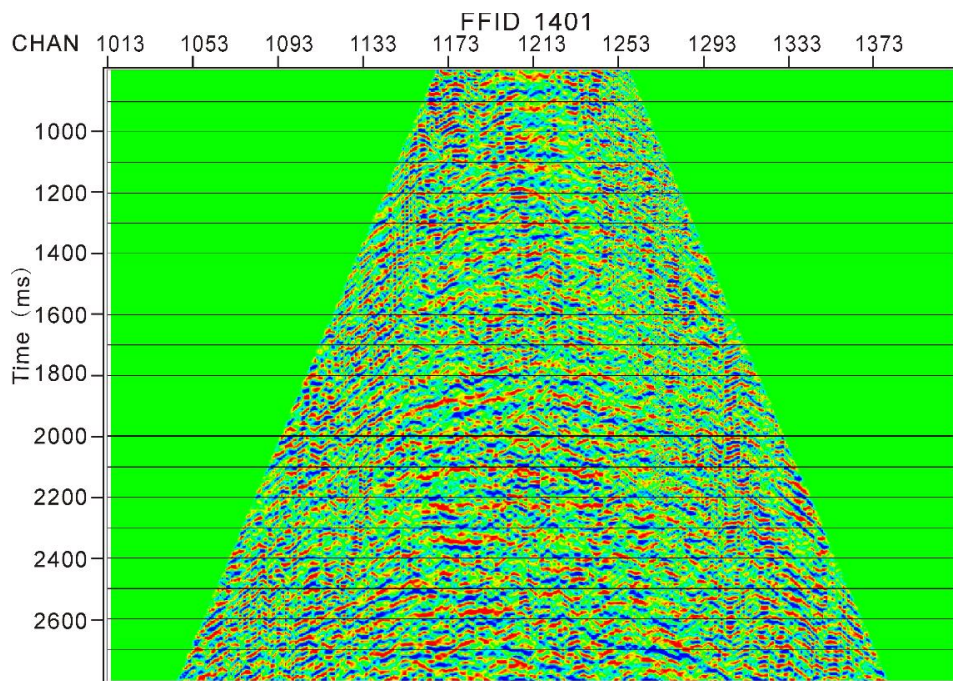


**Figure 32: After FK Filter, a portion of the shot record of inline component.**



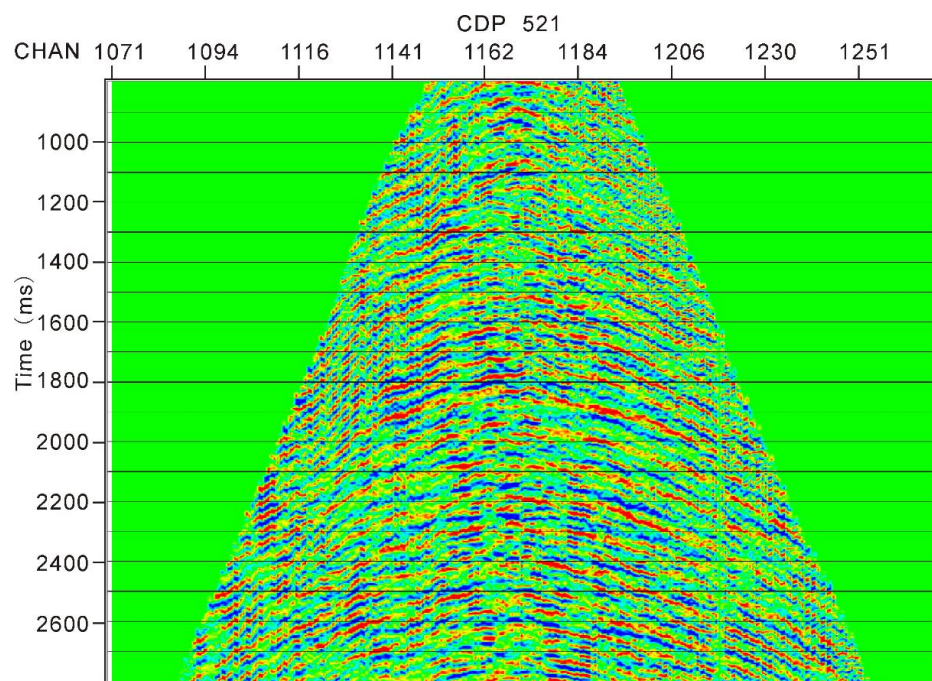


**Figure 33: After removing residual noises, a portion of the CDP record of inline component.**

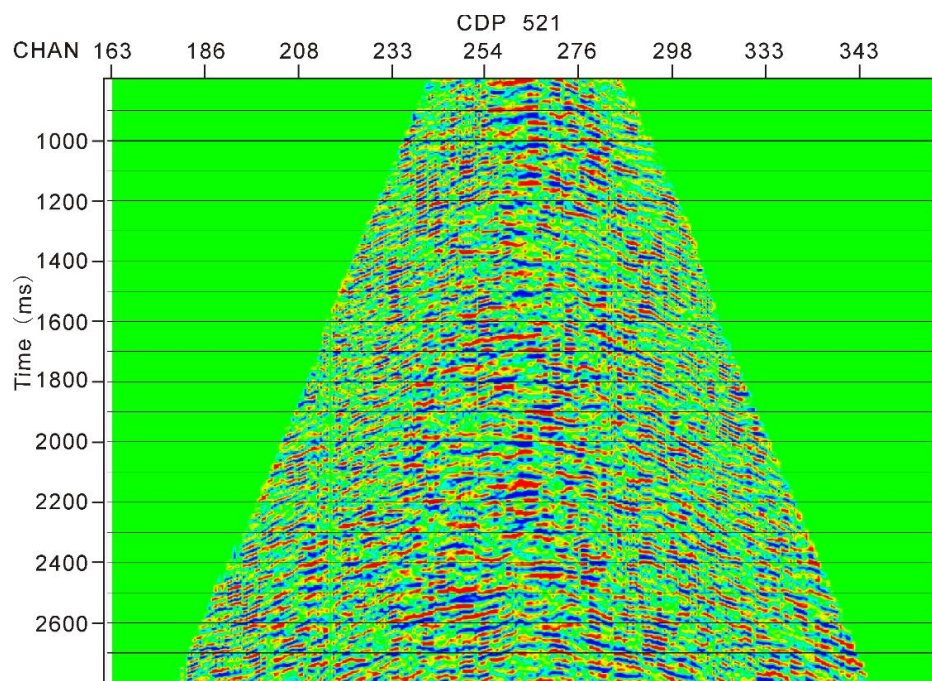


**Figure 34: Preprocessed CDP record of crossline component.**

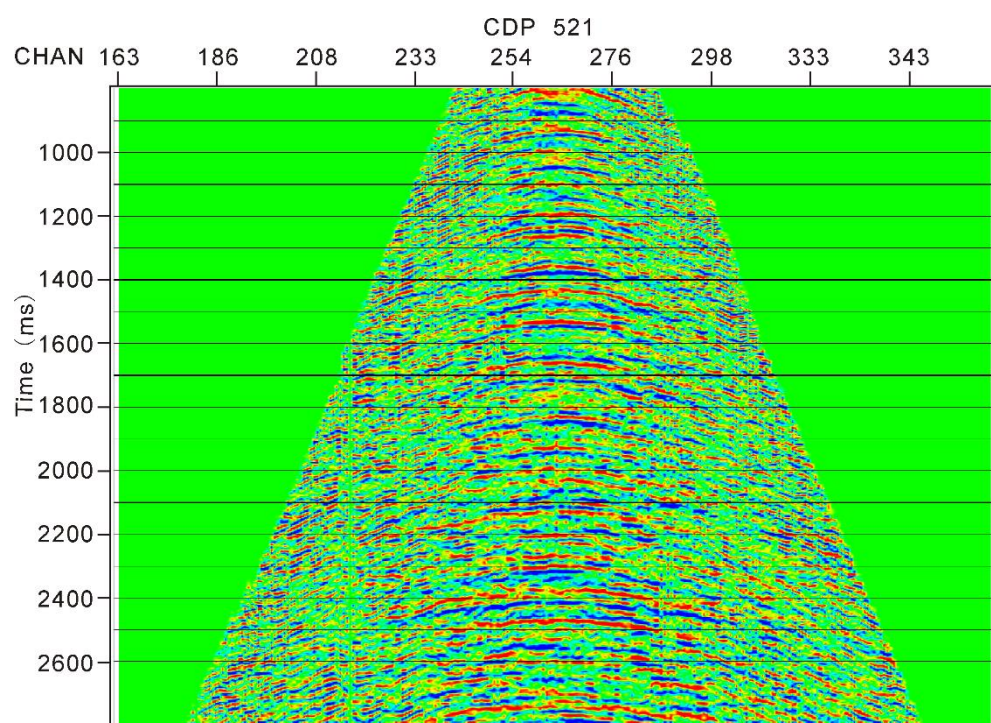


**Figure 35: Preprocessed CDP record of vertical component.**

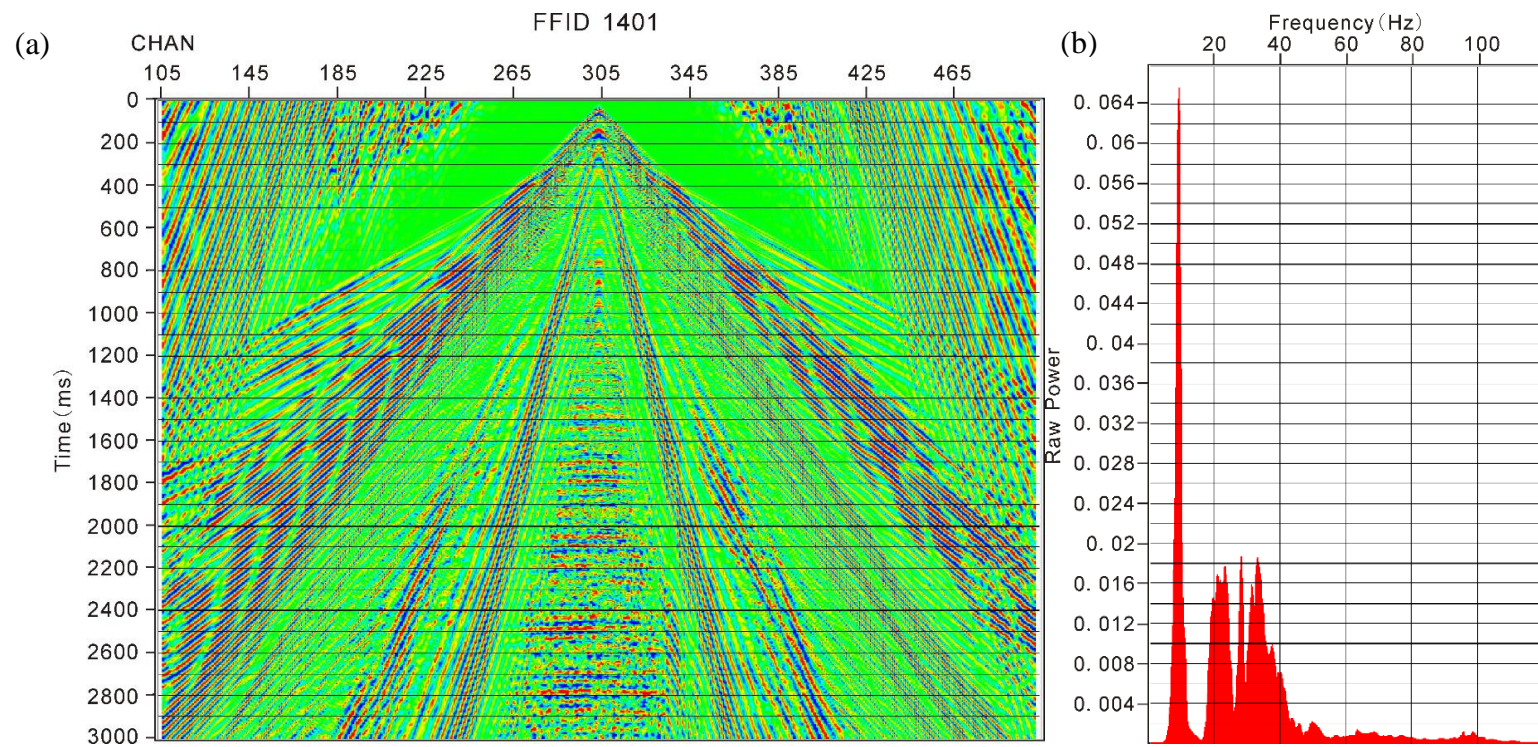


**Figure 36: Pressure component data: (a) A portion of the raw shot record (b) Frequency spectrum of the raw shot record (c) A portion of the preprocessed shot record (d) Frequency spectrum of the preprocessed shot record.**



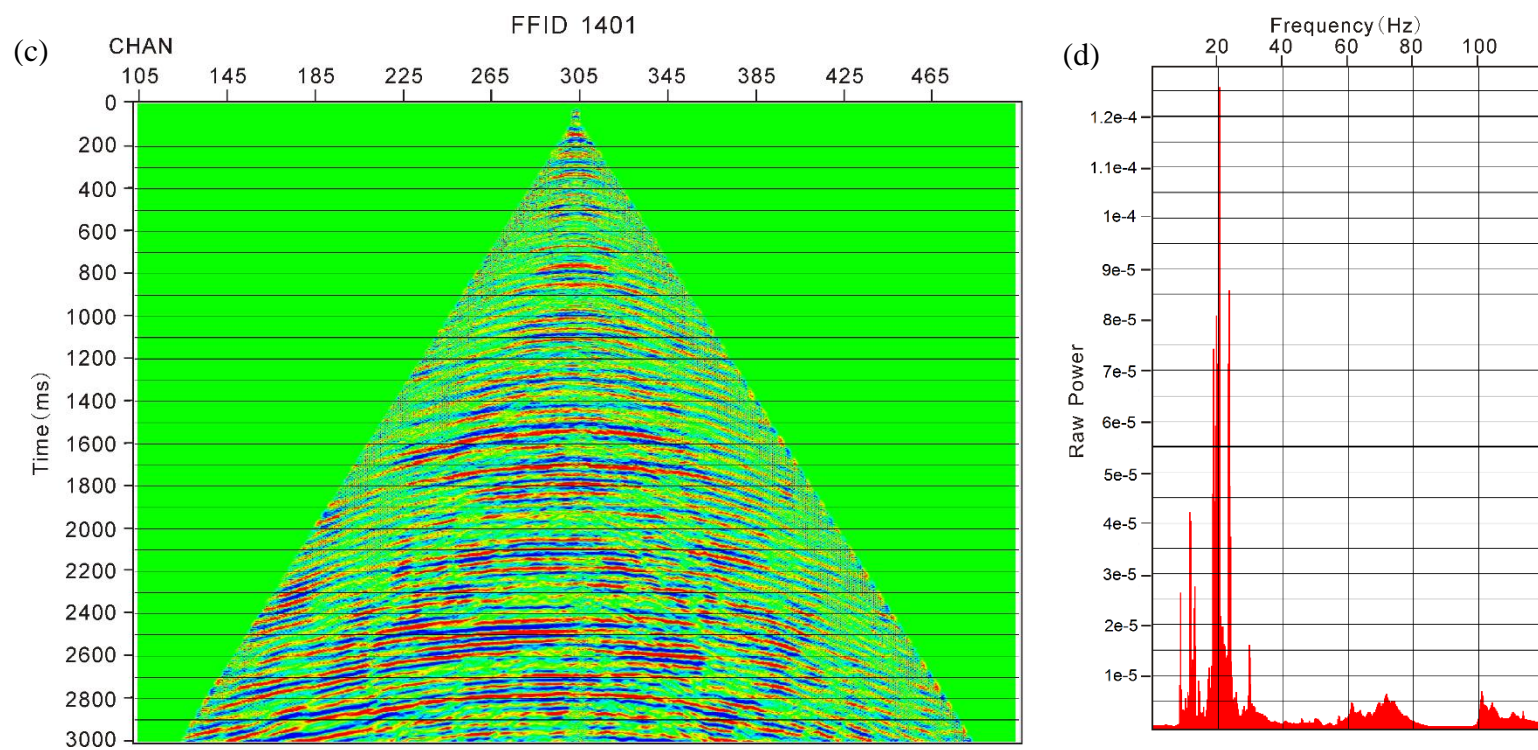


**Figure 36: Continued.**

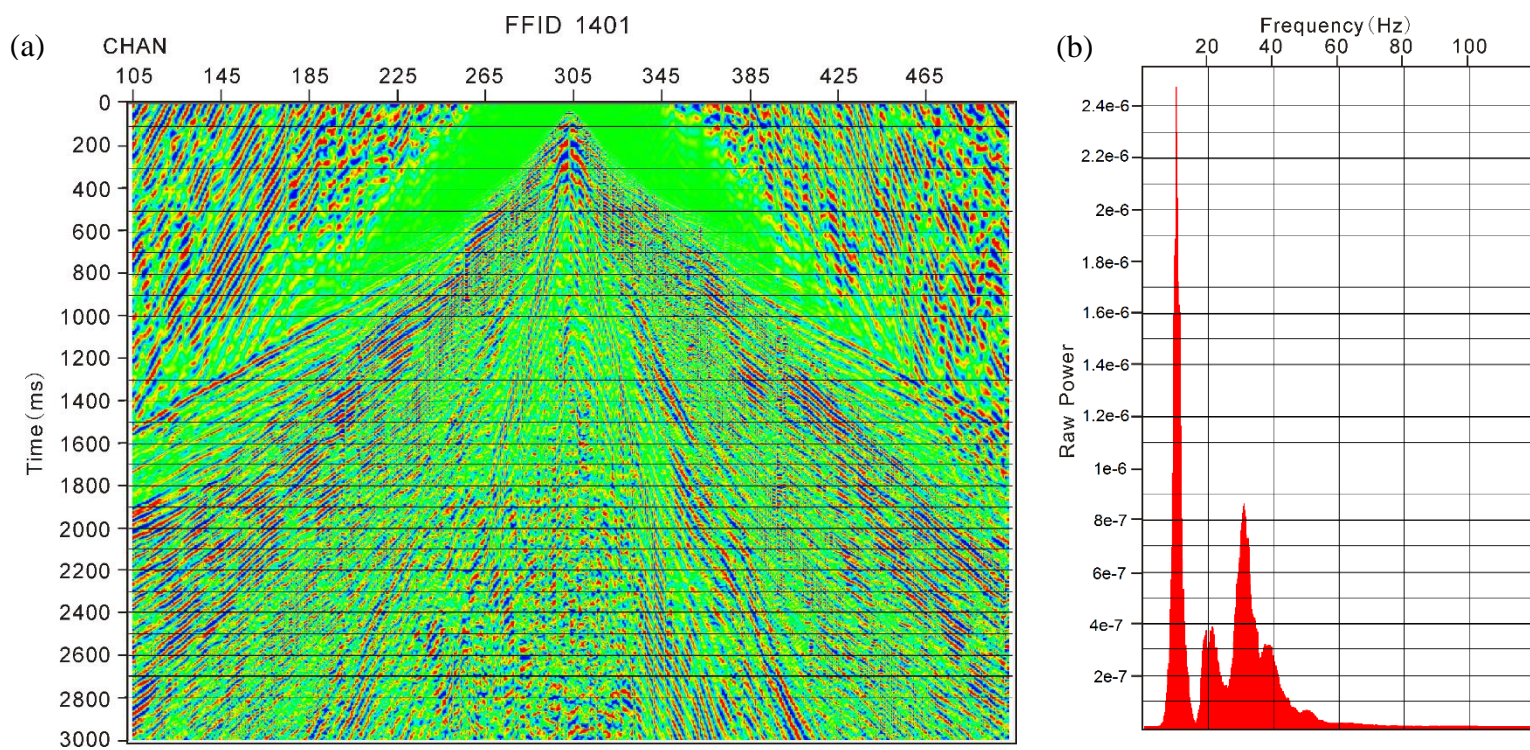


**Figure 37: Inline component data: (a) A portion of the raw shot record (b) Frequency spectrum of the raw shot record (c) A portion of the preprocessed shot record (d) Frequency spectrum of the preprocessed shot record.**

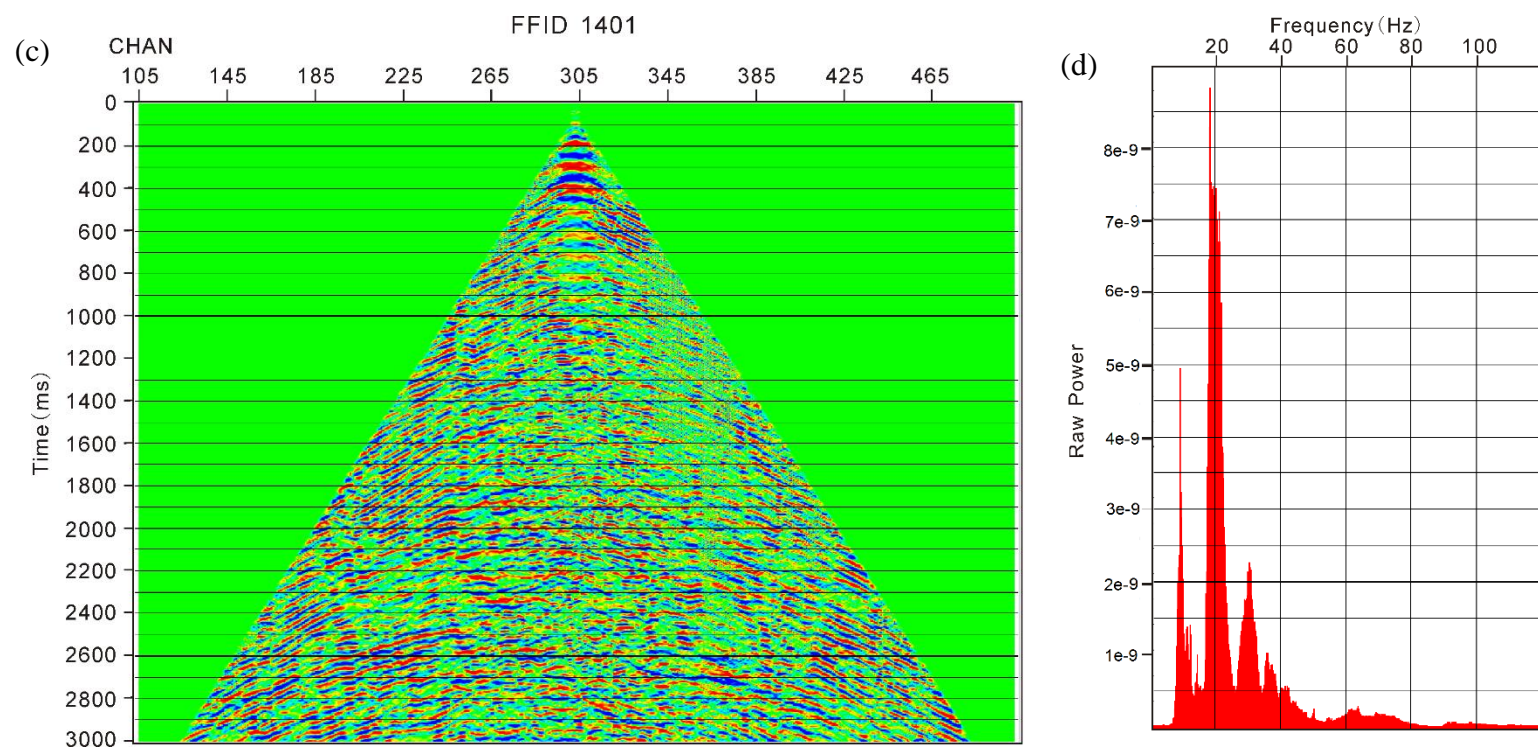


**Figure 37: Continued.**



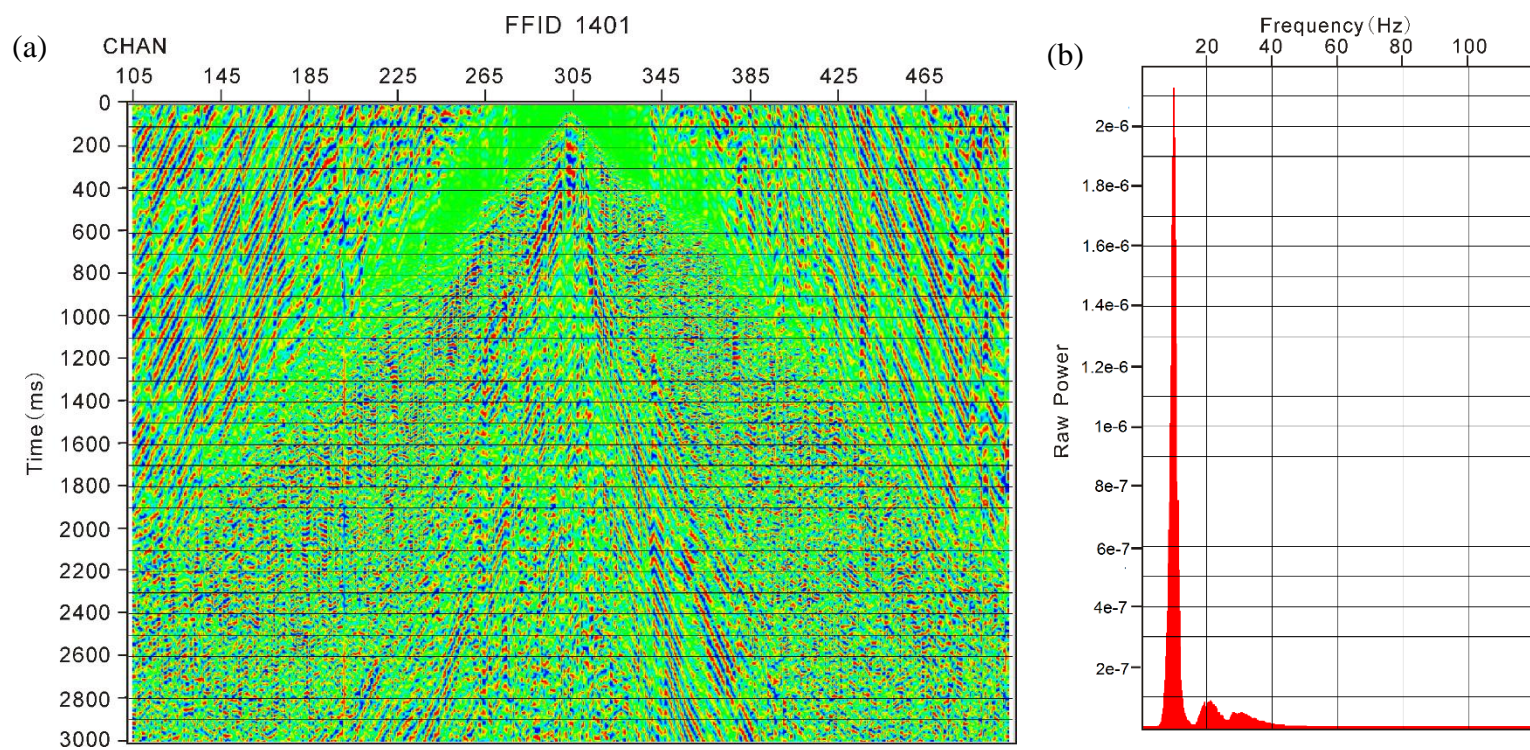


**Figure 38: Crossline component data: (a) A portion of the raw shot record (b) Frequency spectrum of the raw shot record (c) A portion of the preprocessed shot record (d) Frequency spectrum of the preprocessed shot record.**

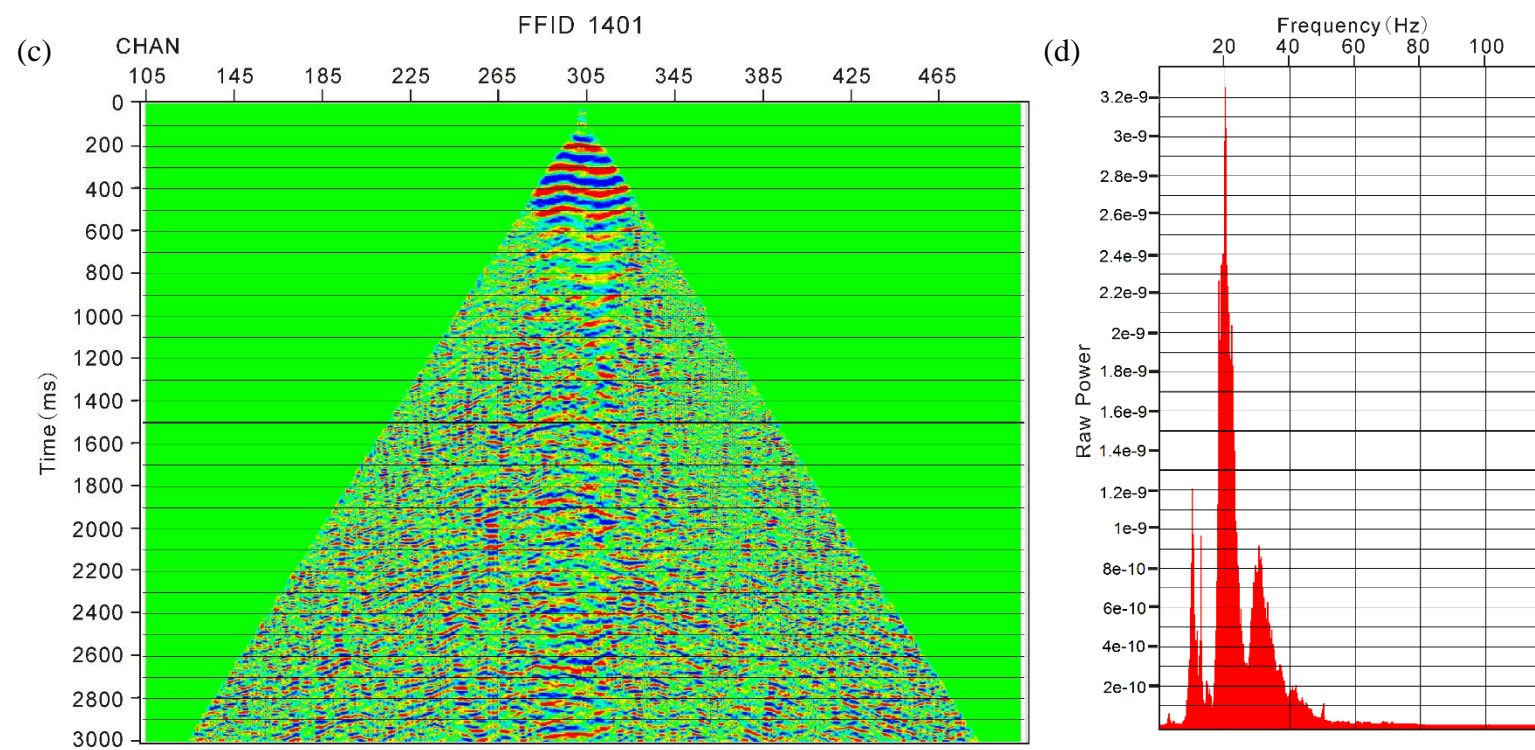


**Figure 38: Continued.**



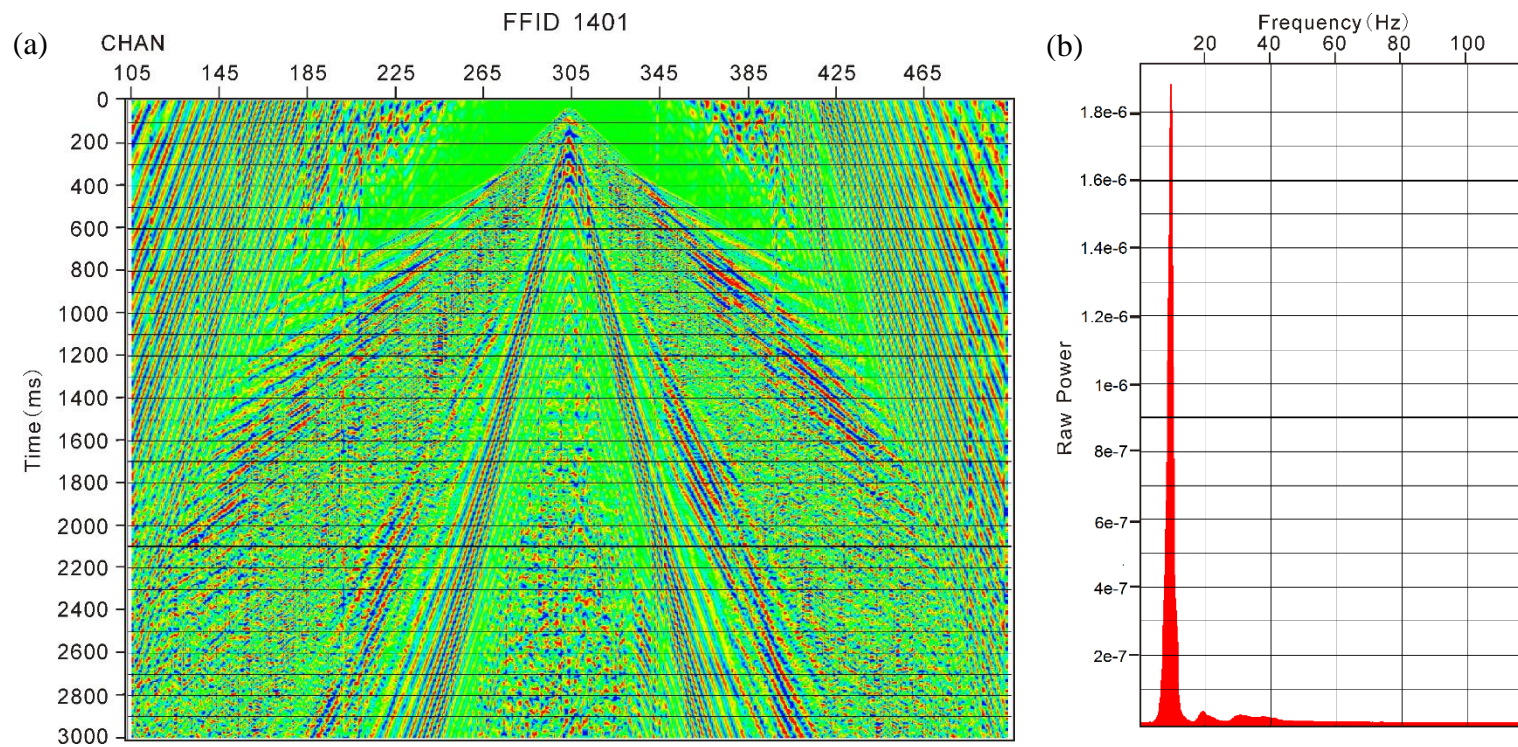


**Figure 39: Vertical component data: (a) A portion of the raw shot record (b) Frequency spectrum of the raw shot record (c) A portion of the preprocessed shot record (d) Frequency spectrum of the preprocessed shot record.**

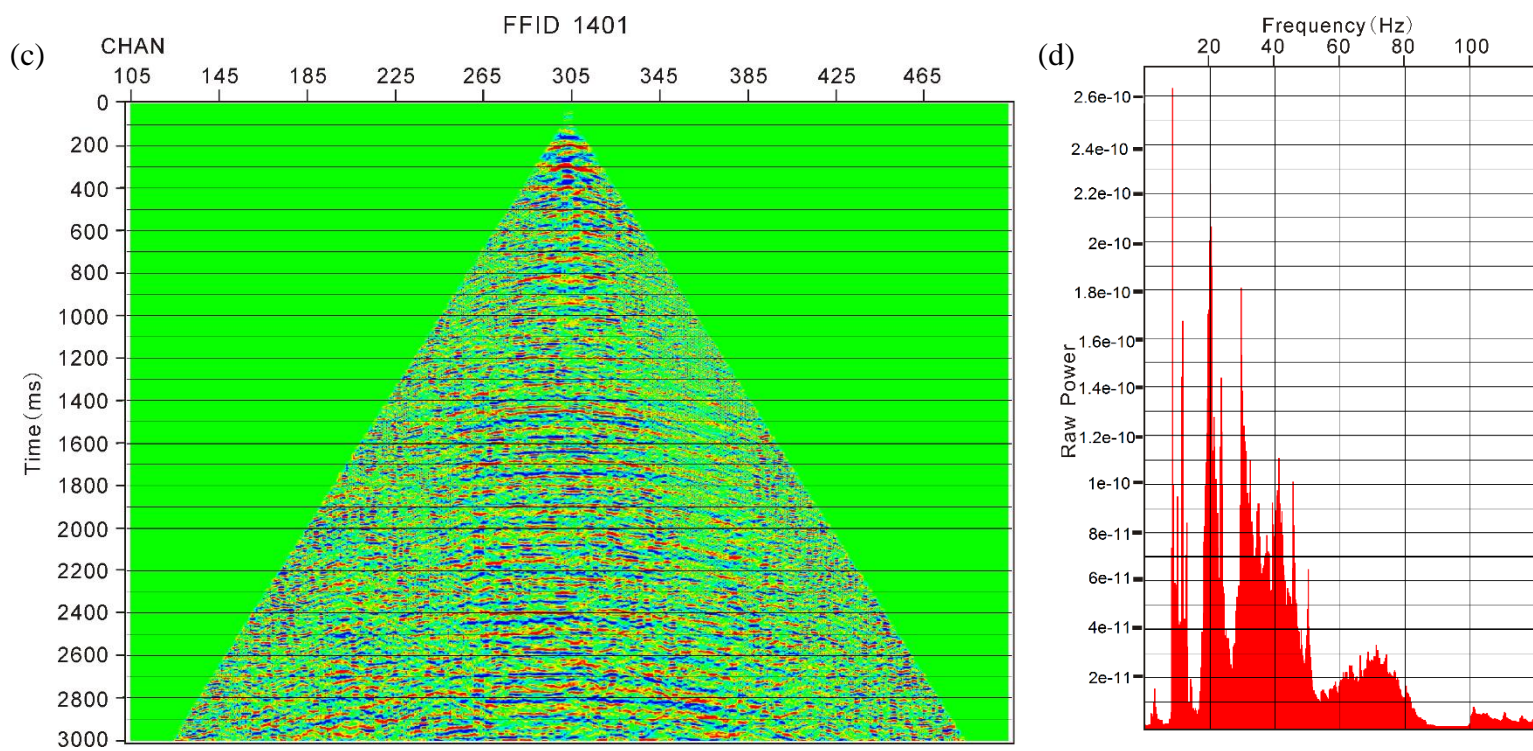


**Figure 39: Continued.**

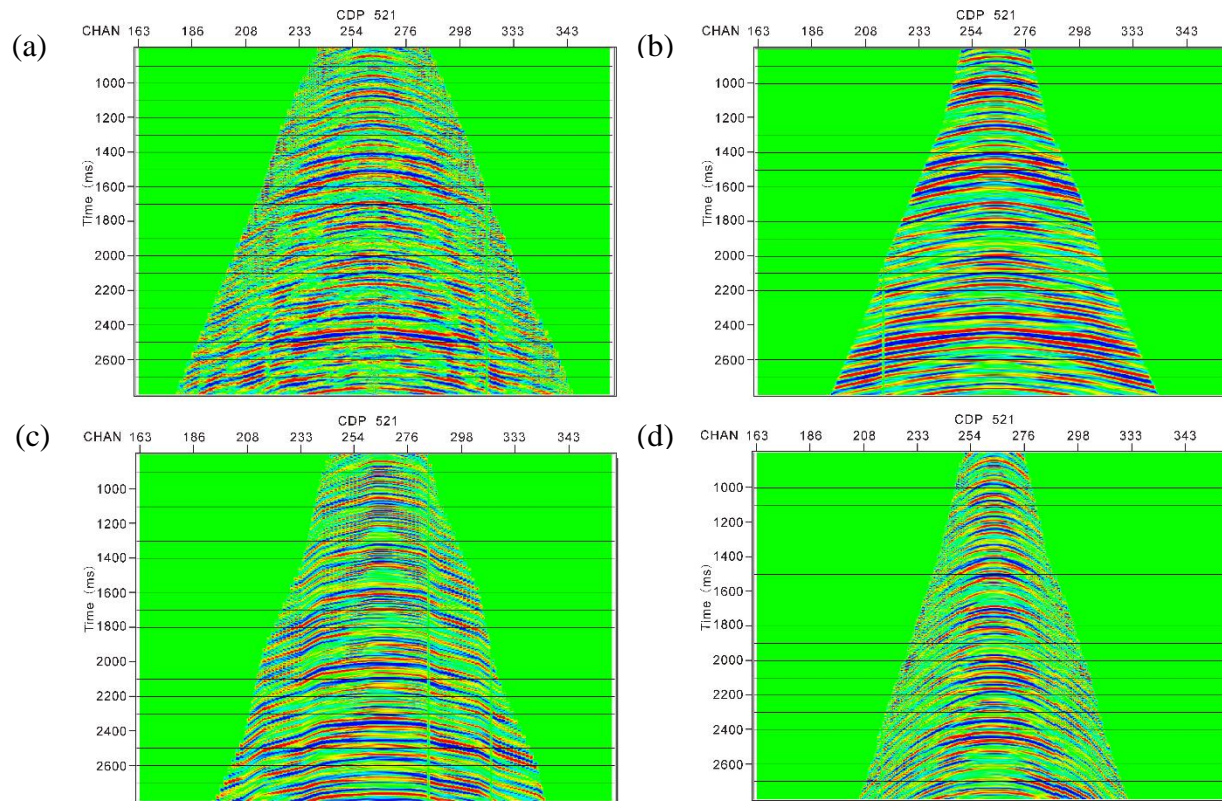
#### *3.4.4 Wave Mode Enhancement Results*

Figure 40(a) shows the CDP record of pressure component after noise suppression, in which there are some hyperbolic events. However, due to the hard sea bottom, there are strong water reverberations, which create baffles to identify primaries from these hyperbolas. In addition, according to the Hook's law, pressure component data may also record converted shear waves, even though low-amplitude S waves may be hidden by strong P waves. To analyze P waves, converted PP-S and PS-S waves respectively in pressure component data, the NMO-FK Filter-Inverse NMO sequences are utilized to extract P wave reflections, PP-S wave reflections and PS-S wave reflections in Figure 40(b)-(d). High-velocity hyperbolas in Figure 40(b) represent P-P waves existing in pressure component data. Lower-velocity hyperbolas in Figure 30(c) and very low-velocity hyperbolas in Figure 30(d) illustrate there are also converted PP-S waves and PS-S waves in pressure component data. In the same way, Figure 41(a) shows the CDP record of inline component after noise removal, and Figure 41(b)-(d) represent the extracted P-P waves, PP-S waves and PS-S waves in inline component data. These wavefields are also extracted from the crossline and vertical component data.

#### *3.4.5 Seismic Data Stacking Results*

In the end, the P-wave, PP-S wave and PS-S wave stacked sections in four-component data are obtained through stacking each extracted wavefield. Figure 42-45 show these stacking results in pressure, inline, crossline and vertical component, separately. By observing all these stacking results, it is difficult to figure out which one can image the geological structures better. However, the stacked sections in crossline

component (Figure 44) are very poor without any desired reflection signal. But there are hyperbolic reflections existing in the CDP record after the preprocessing flow in Figure 34. That's because the signal in crossline record is not consistent. Even though there exist some hyperbolic events in CDP gather, the conventional stacking algorithm results in the cancellation of reflections along the offsets in crossline component. Compared with the pressure and inline component data, the stacked sections in vertical component (Figure 45) have shorter wavelength and higher frequency, which is consistent with the previous frequency spectra analysis.



**Figure 40: Pressure component data: (a) Preprocessed CDP record (b) CDP record after extracting P wave reflections, showing hyperbolic P wave reflections; (c) CDP record after extracting PP-S wave reflections, showing hyperbolic PP-S wave reflections; (d) CDP record of after extracting PS-S wave, showing hyperbolic PS-S- wave reflections.**



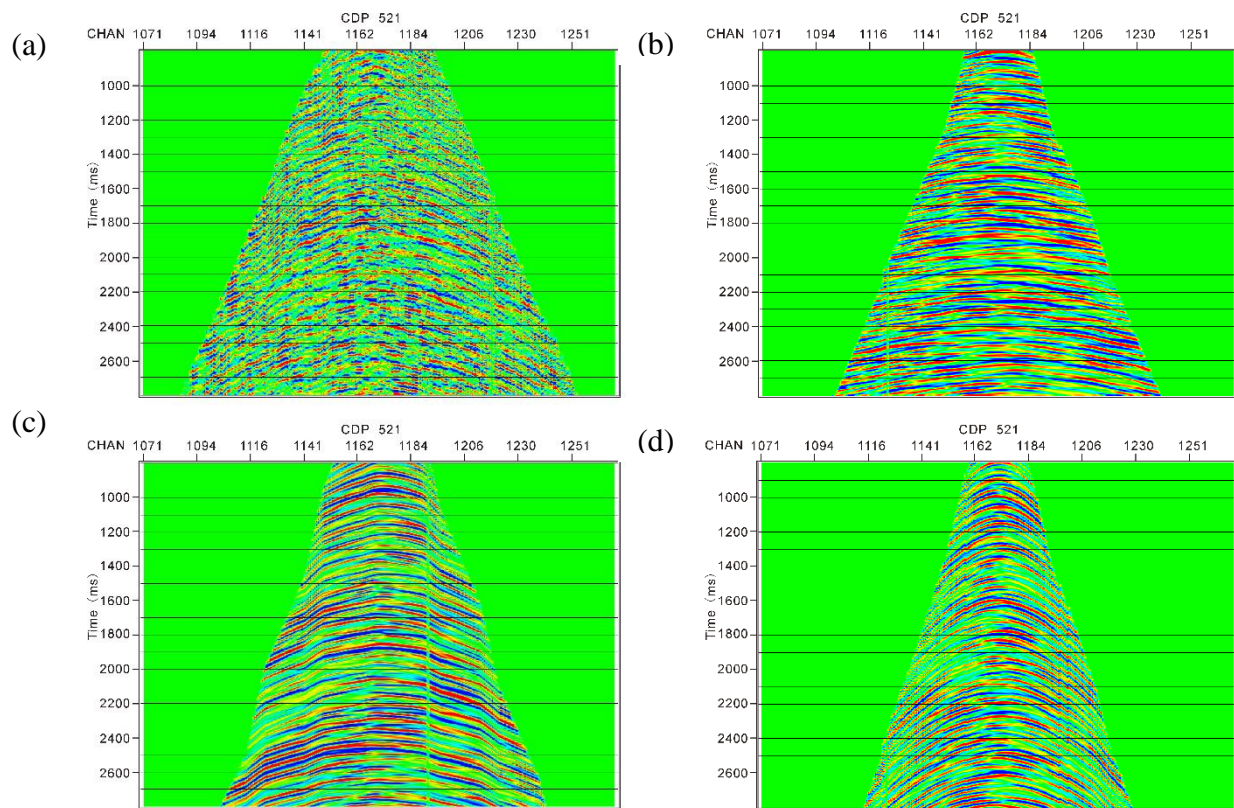


**Figure 41: Inline component data: (a) Preprocessed CDP record (b) CDP record after extracting P wave reflections, showing hyperbolic P wave reflections; (c) CDP record after extracting PP-S wave reflections, showing hyperbolic PP-S wave reflections; (d) CDP record of after extracting PS-S wave, showing hyperbolic PS-S- wave reflections.**

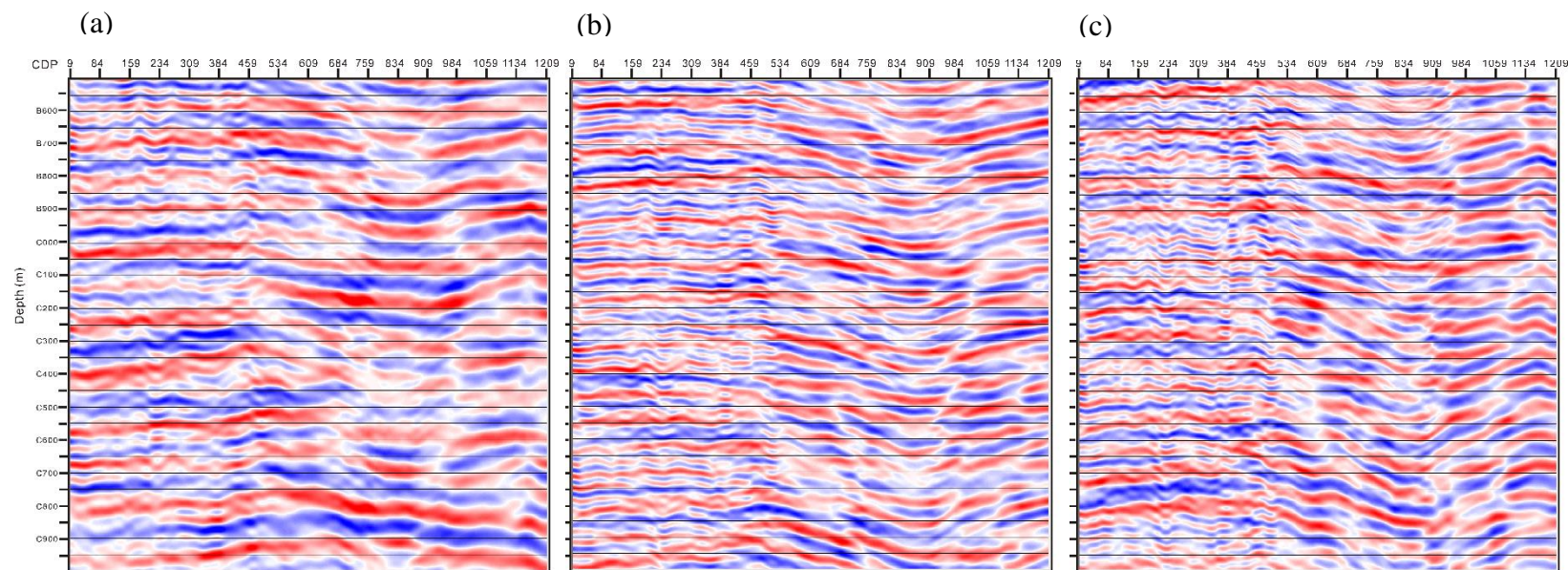


**Figure 42: Pressure component data: (a) P-P stacked section (b) PP-S stacked section (c) PS-S stacked section.**



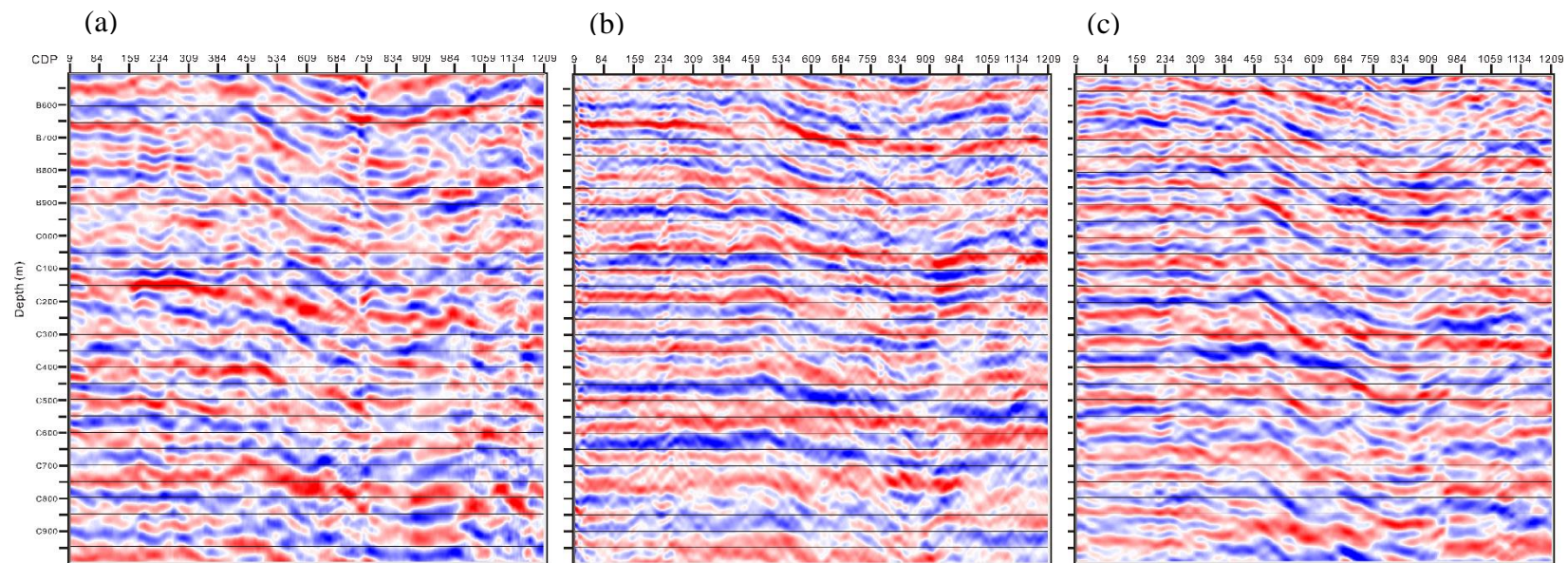


**Figure 43: Inline component data: (a) P-P stacked section (b) PP-S stacked section (c) PS-S stacked section.**

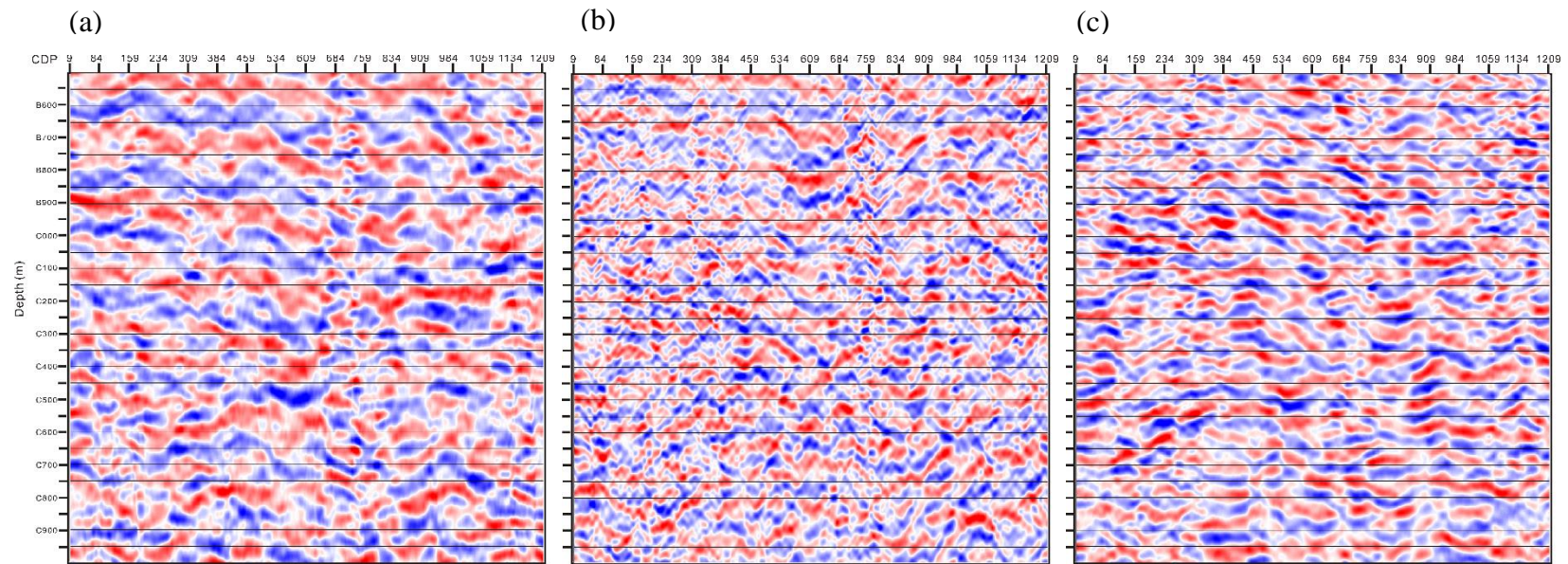


**Figure 44: Crossline component data: (a) P-P stacked section (b) PP-S stacked section (c) PS-S stacked section.**



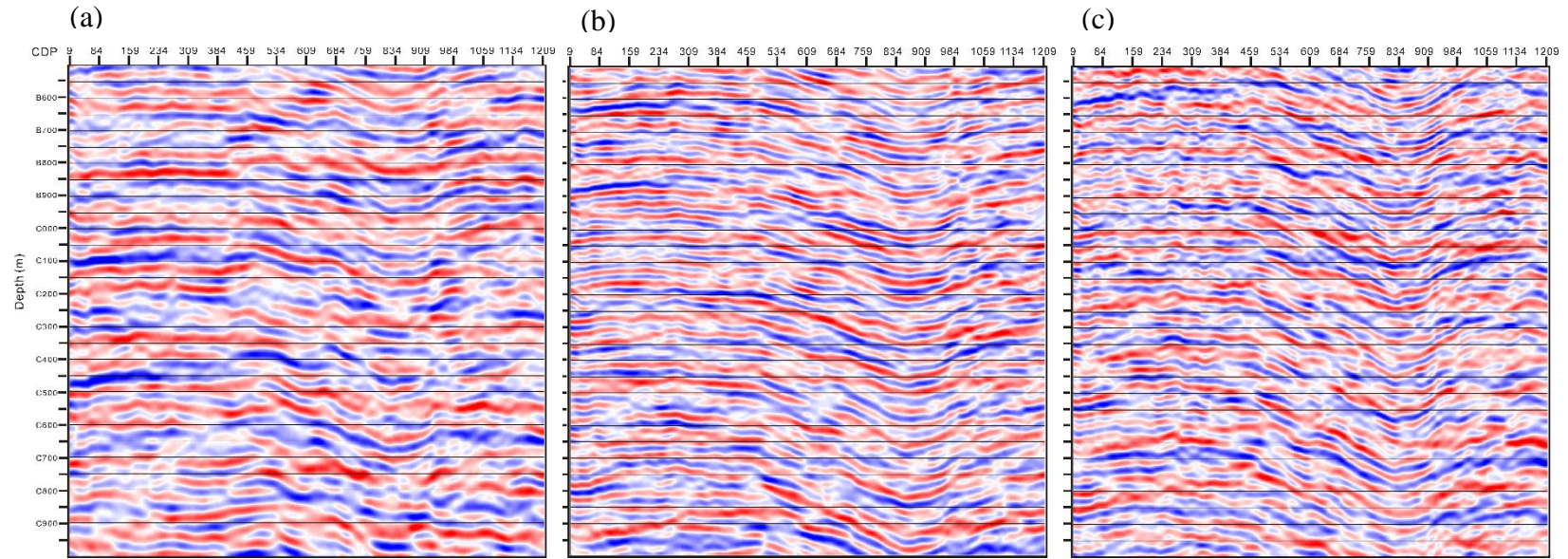


**Figure 45: Vertical component data: (a) P-P stacked section (b) PP-S stacked section (c) PS-S stacked section.**

### *3.4.6 Wave Mode Analysis and Geological Interpretation*

To evaluate these stacked sections, P wave, PP-S wave and PS-S wave synthetic traces are created from log data. Reflection coefficients are calculated from P velocity, S velocity and density in Figure 46. By convolving the reflection coefficients with the wavelet, synthetic traces are formed in the depth domain. Two wavelets used in the study are 100Hz and 20Hz Ricker wavelets. The 100Hz synthetic trace has a very high resolution, which almost reflects all variations of P wave impedance. But with decreasing the wavelet frequency to 20Hz (which is closer to the dominant frequency of real seismic data), the resolution decreases a lot. For instance, the negative wiggle at the depth C800m includes two tops of two formations. Similarly, Figure 47 and 48 show the synthetic traces of PP-S wave and PS-S wave.

The smallest distance between the well with the 2D test line is 733m at CDP 702. So, the synthetic traces are plotted with seismic data at CDP 702. Due to the dominant frequency of vertical component data is 30Hz, the synthetic traces in stacked sections of vertical records are created by a 30Hz Ricker wavelet. Other seismogram traces are formed through the convolution between reflection coefficients with a 20Hz Ricker wavelet. Figure 49 displays the P-wave stacked sections in four components. Compared with data recorded by inline and vertical geophones, the P stacked section in pressure component data has a higher S/N and matches with the synthetic P-wave trace better. The PP-S stacked sections in all four components are shown in Figure 50. The imaging results in pressure and vertical component have a better match with synthetic PP-S wave traces than the inline component imaging. But in the pressure record (Figure 50(a)), the

frequency by the left side of CDP500 is obviously higher than the right. This artificial phenomenon can be explained by the effect of residual P waves or geological variations in the space. The PP-S stacked section in vertical component has a higher resolution, so it is selected to image subsurface structures via PP-S waves. Finally, by observing the PS-S stacked sections in Figure 51, the same high-frequency phenomenon also occurs in the PS-S wave imaging of pressure record. And compared with the vertical component imaging, the PS-S imaging in inline component has a higher S/N and is more consistent with the synthetic PS-S wave. After well log tie analysis, the P stacked section in pressure component, the PP-S stacked section in vertical component and the PS-S stacked section in inline component are selected in Figure 52. Although the vertical component data have higher frequency contents and a higher resolution, these stacked images illustrate similar geological structures via utilizing different wavefields.

Besides well log tie analysis, the energy distribution of each wave mode is analyzed in four-component data. All the stacked images are shown with AGC, which cannot reflect the real energy of each wavefield in the dataset. To calculate the energy of CDP702 trace, the amplitudes along the trace are obtained at a fixed sample rate, then summarize the squared amplitudes. Table 2 concludes the energy distributions of P waves, converted PP-S and PS-S waves in pressure, inline and vertical component data. Due to the cancellation of signals in crossline component, the energy distribution is not analyzed in this part. First, by comparing the percentage of each component data, the P-P wave signals are the strongest in pressure component; and the PP-S wave signals have the largest part of energy in inline and vertical component. However, due to the different

measurement, the energy recorded by hydrophones is thirty thousand times than that by 3D geophones. To perform the comparison between different component data, scaling is implemented to make the sum of energy as a same value. Considering the previous well log tie analysis, P-P wave signals detected by hydrophones have the strongest energy. PP-S wave reflections recorded by vertical geophones and PS-S wave signals in inline component are also strong, but not the maximum.

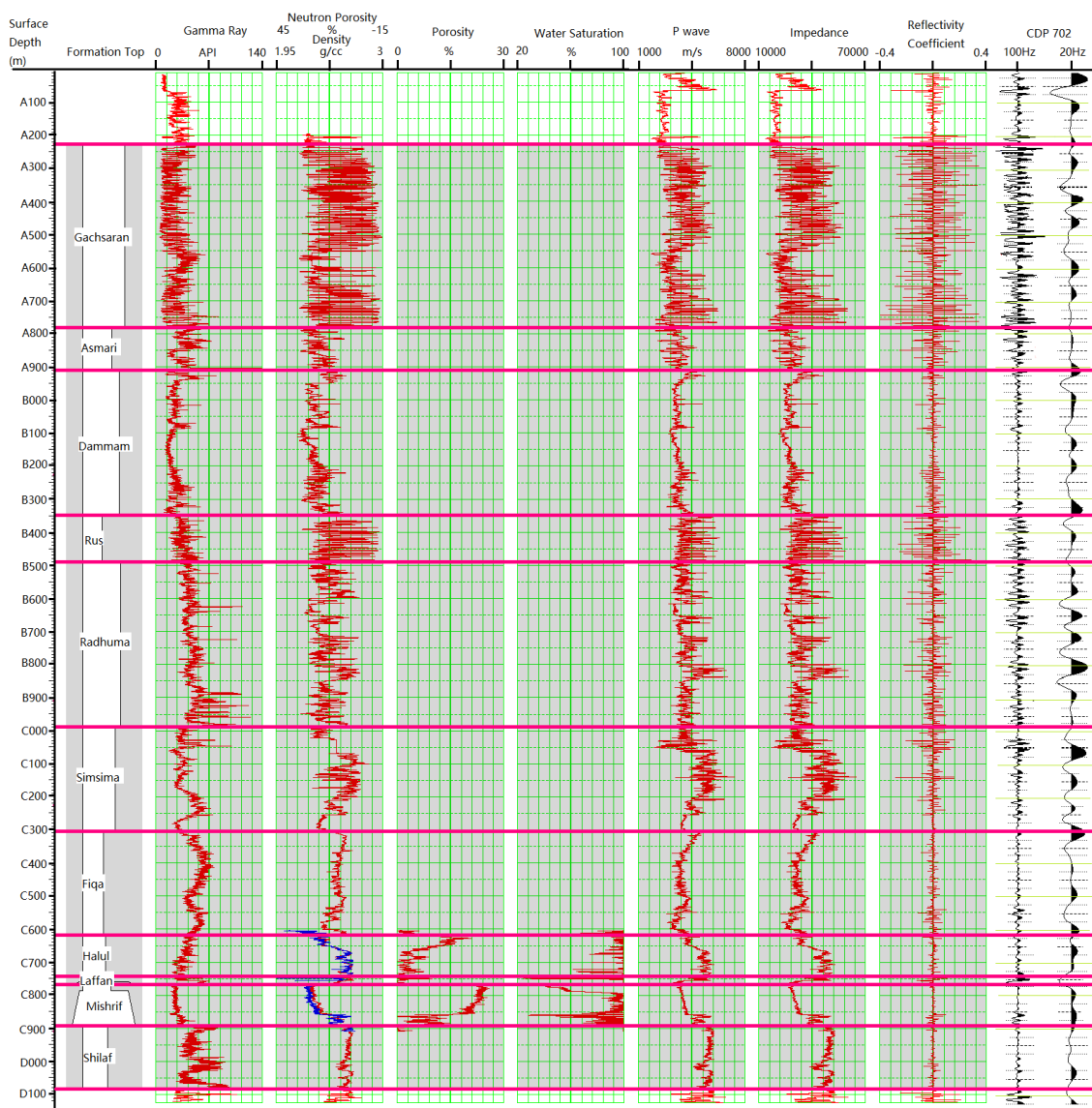


**Figure 46: Illustrating P wave acoustic impedance, reflection coefficient and synthetic trace with different-frequency Ricker wavelets (100Hz and 20Hz), based on P wave sonic log and density log data.**



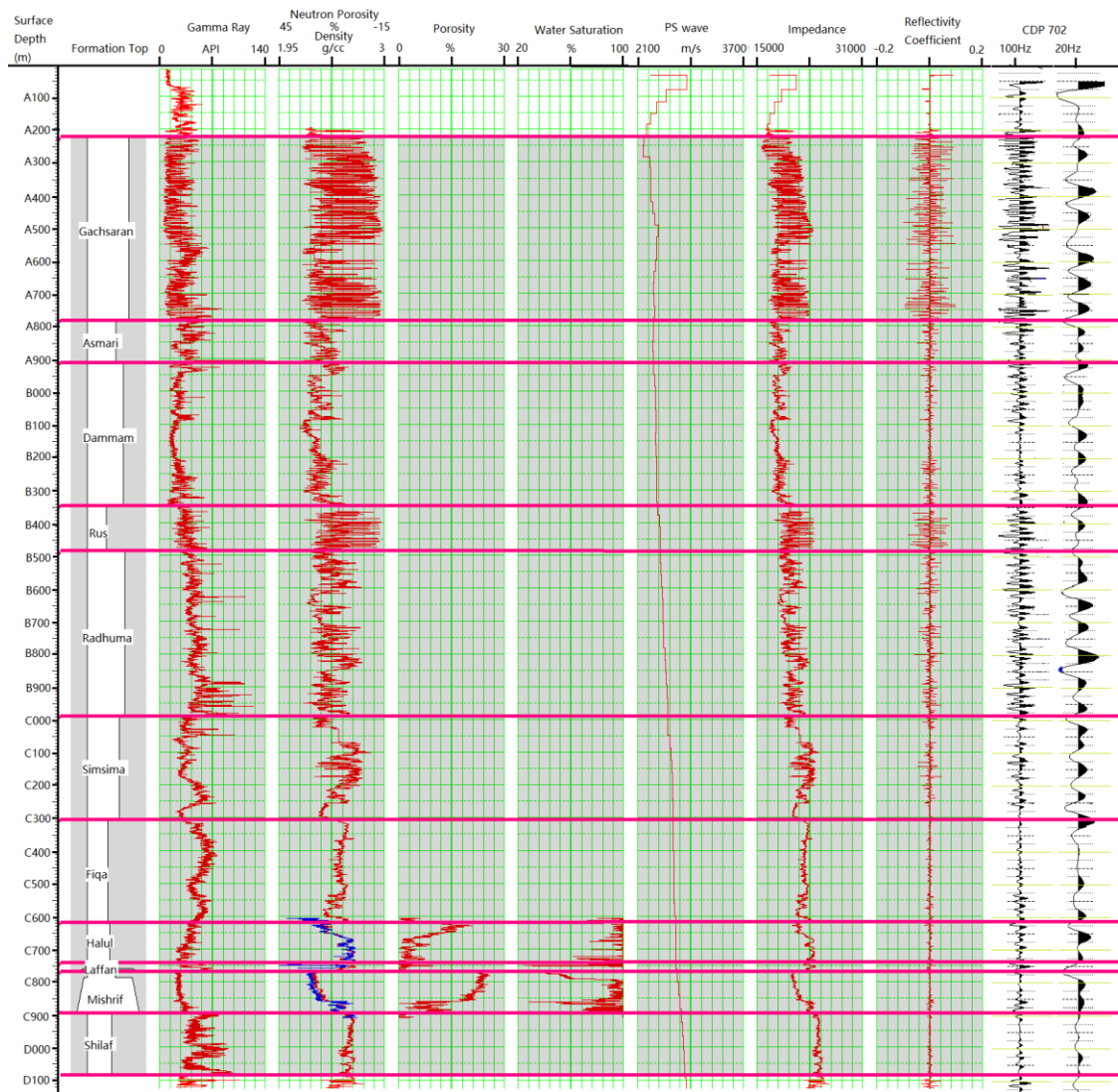


**Figure 47: Illustrating PP-S wave acoustic impedance, reflection coefficient and synthetic trace with different-frequency Ricker wavelets (100Hz and 20Hz), based on S wave sonic log and density log data.**

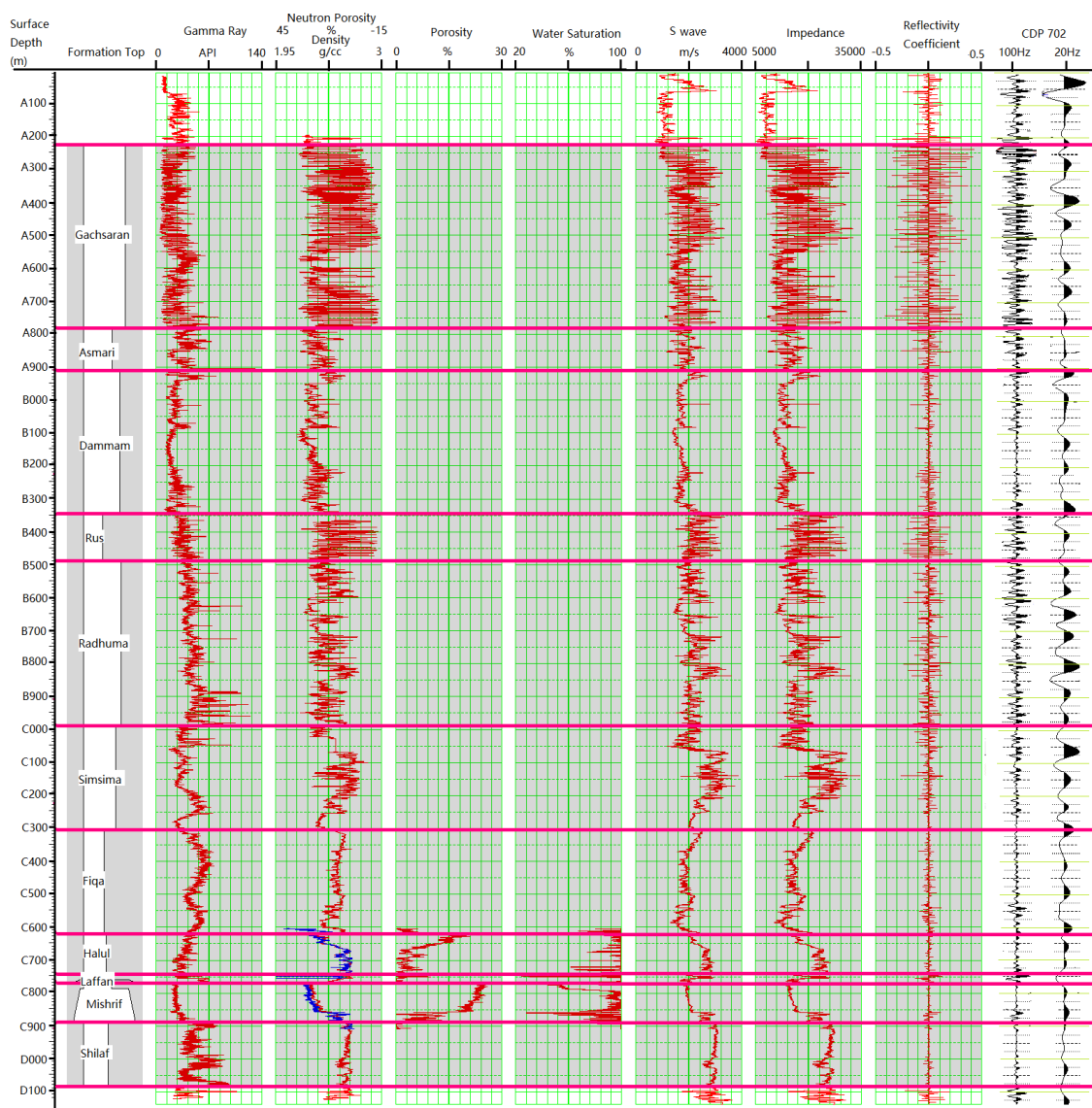


**Figure 48: Illustrating PS-S wave acoustic impedance, reflection coefficient and synthetic trace with different-frequency Ricker wavelets (100Hz and 20Hz), based on S wave sonic log and density log data.**

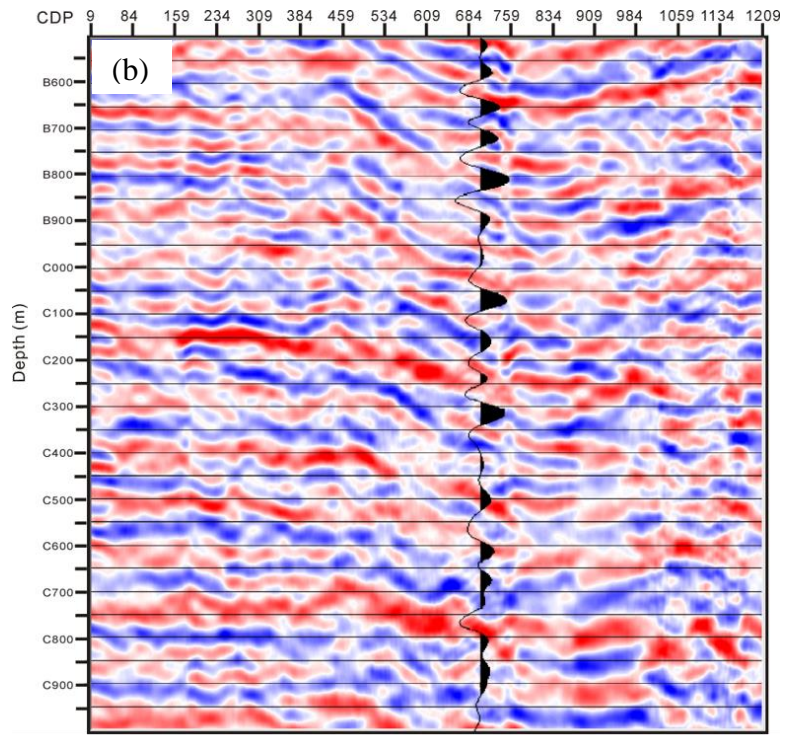
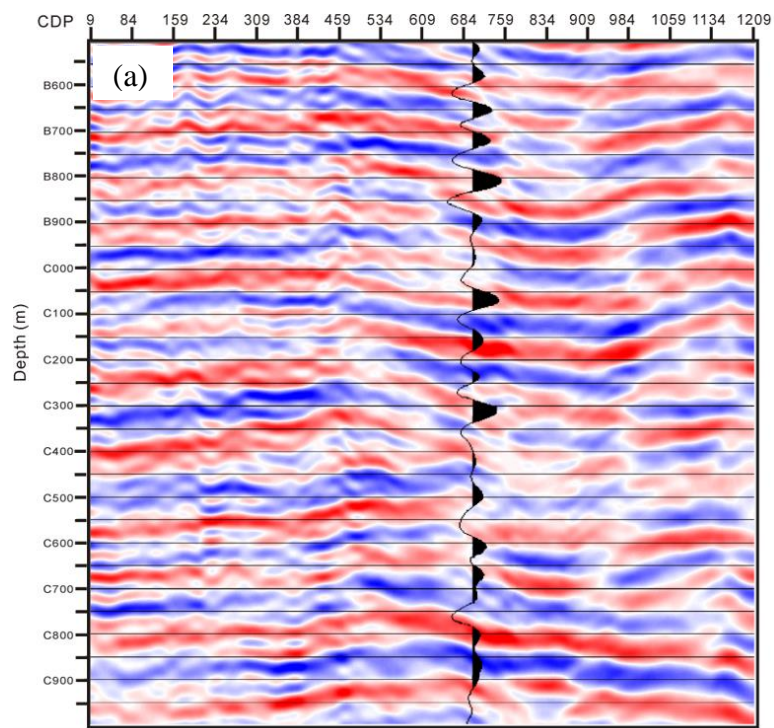


**Figure 49: Portions of P stacked sections at the reservoir zone with synthetic P-wave reflection signals: (a) Hydrophone; (b) Inline geophone; (c) Crossline geophone; (d) Vertical geophone.**



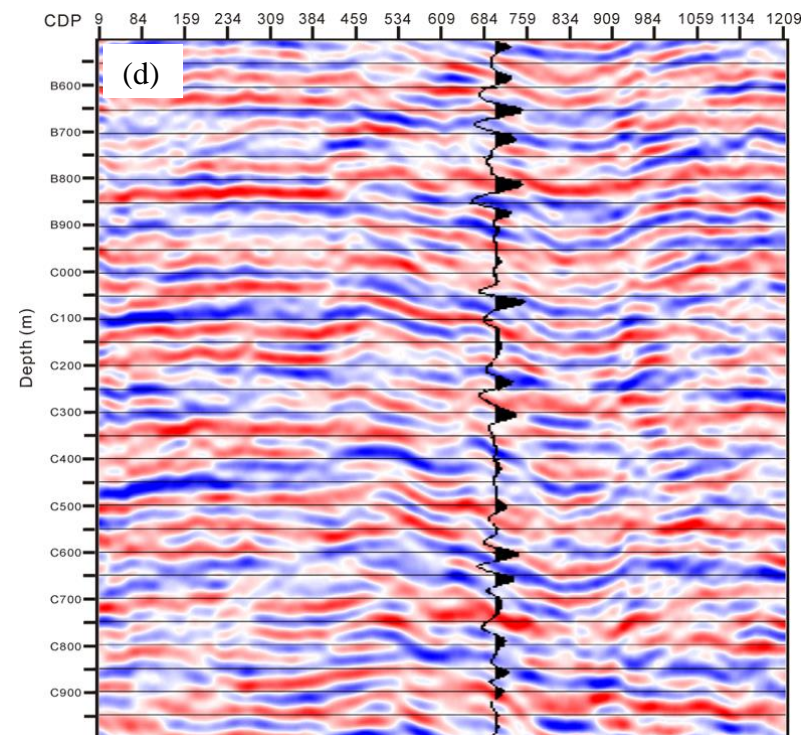
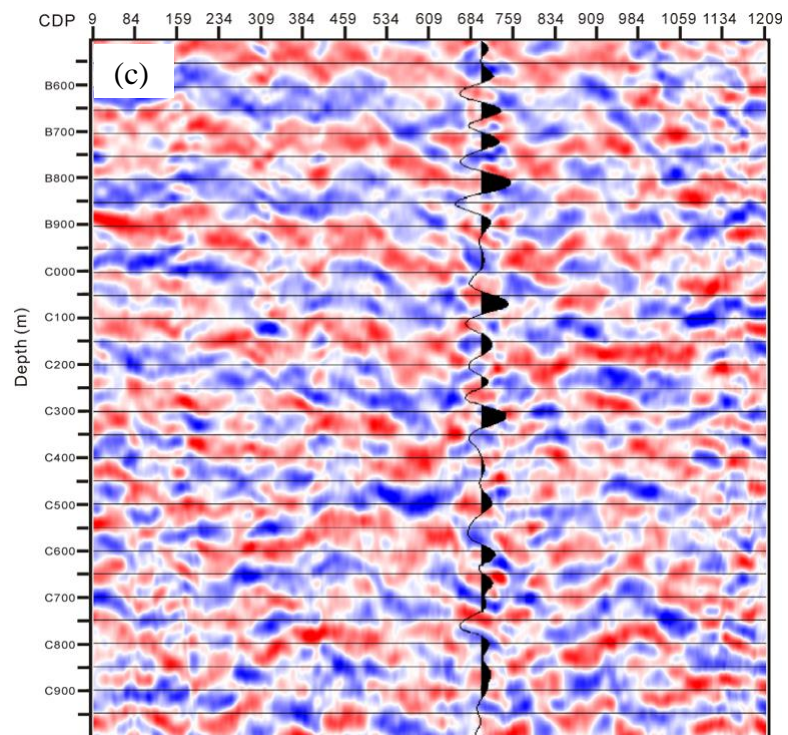


**Figure 49: Continued.**

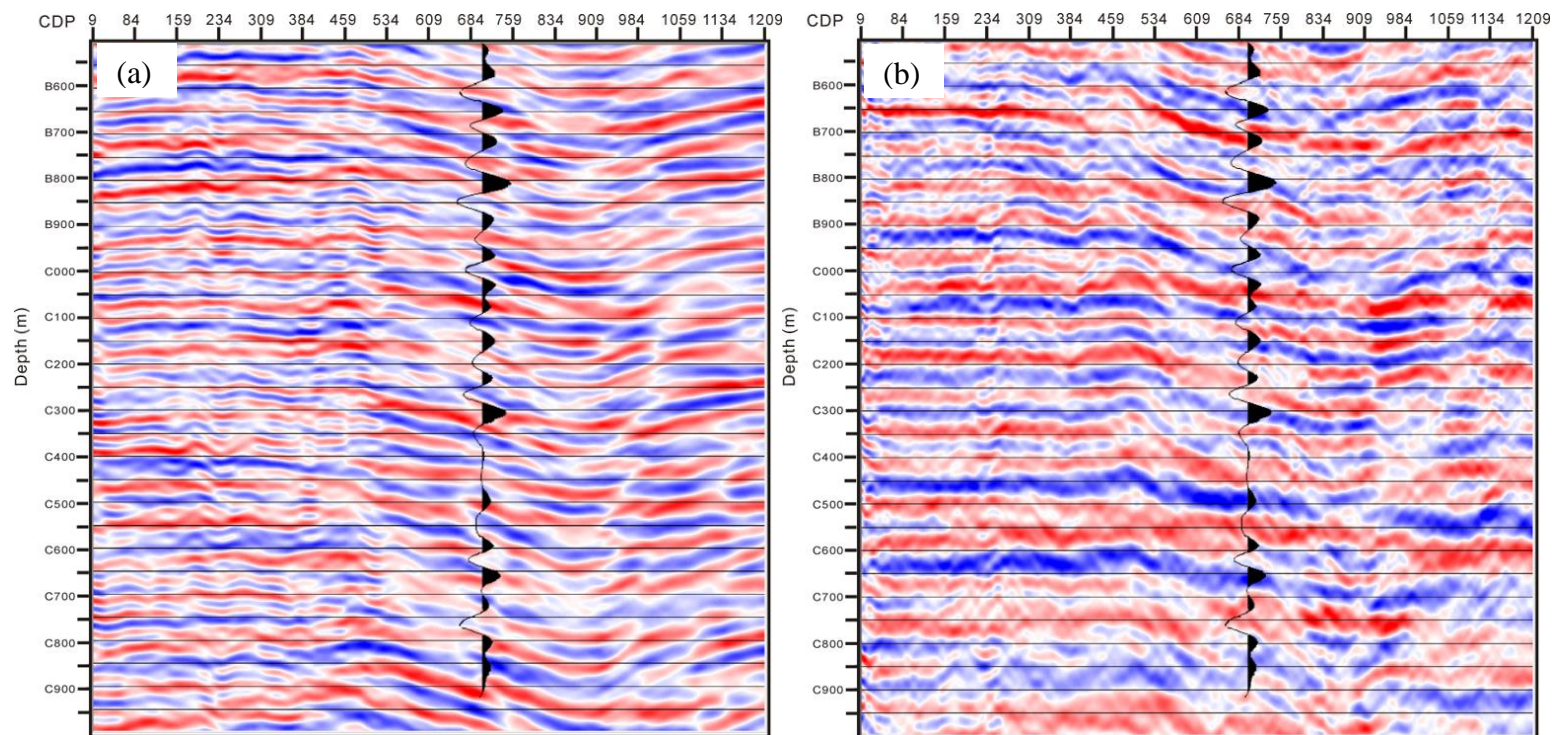


**Figure 50: Portions of PP-S stacked sections at the reservoir zone with synthetic PP-S wave reflection signals: (a) Hydrophone; (b) Inline geophone; (c) Crossline geophone; (d) Vertical geophone.**



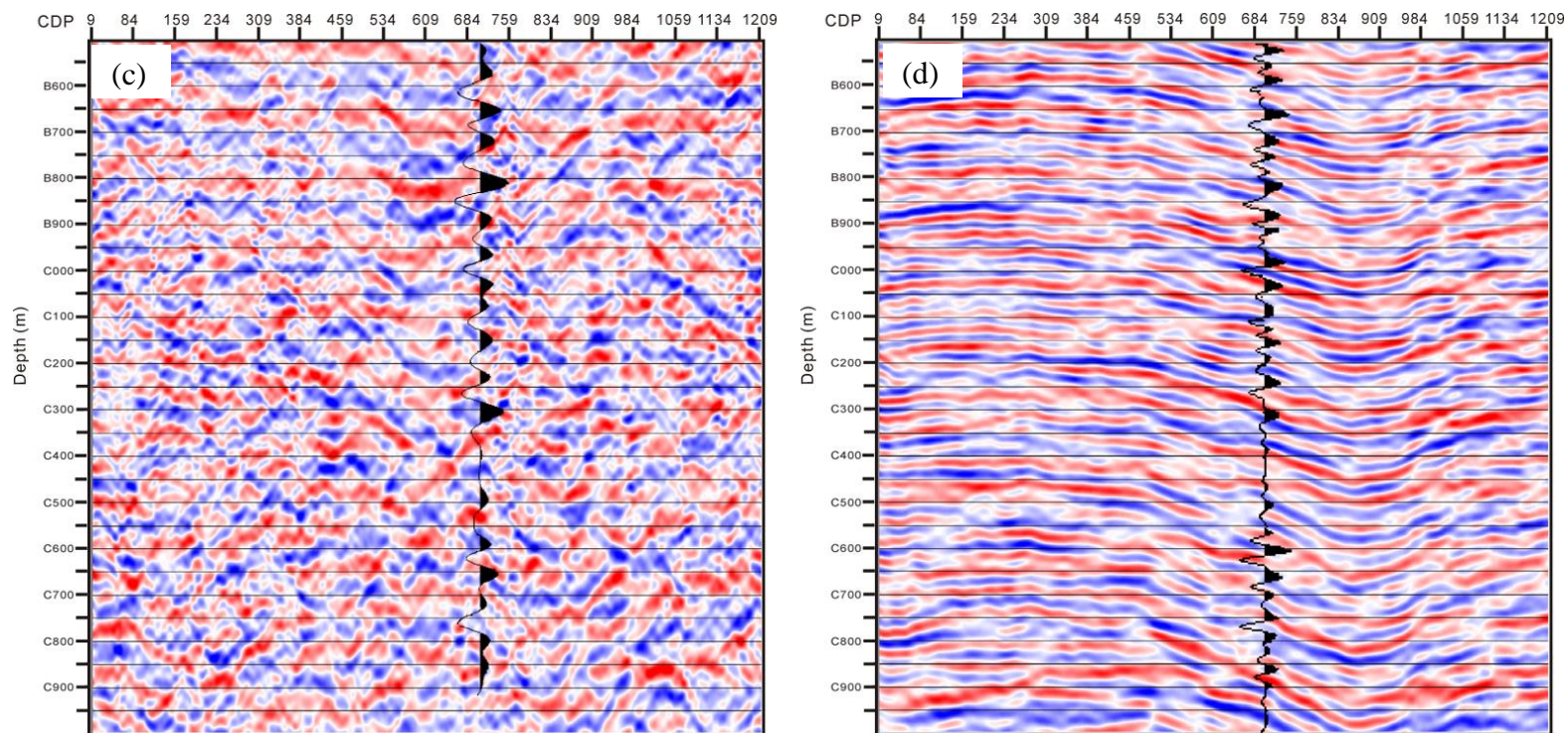


**Figure 50: Continued.**

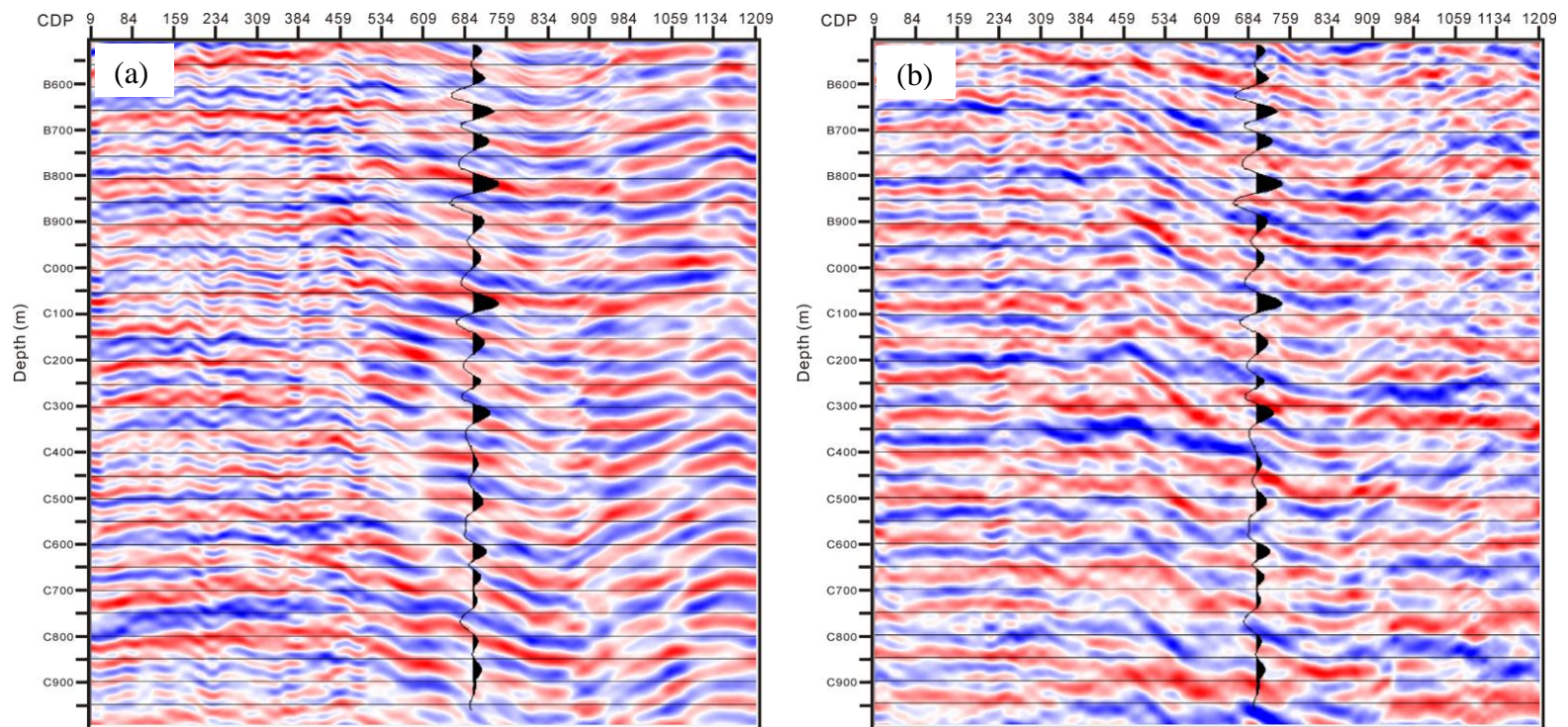


**Figure 51: Portions of PS-S stacked sections at the reservoir zone with synthetic PS-S wave reflection signals: (a) Hydrophone; (b) Inline geophone; (c) Crossline geophone; (d) Vertical geophone.**



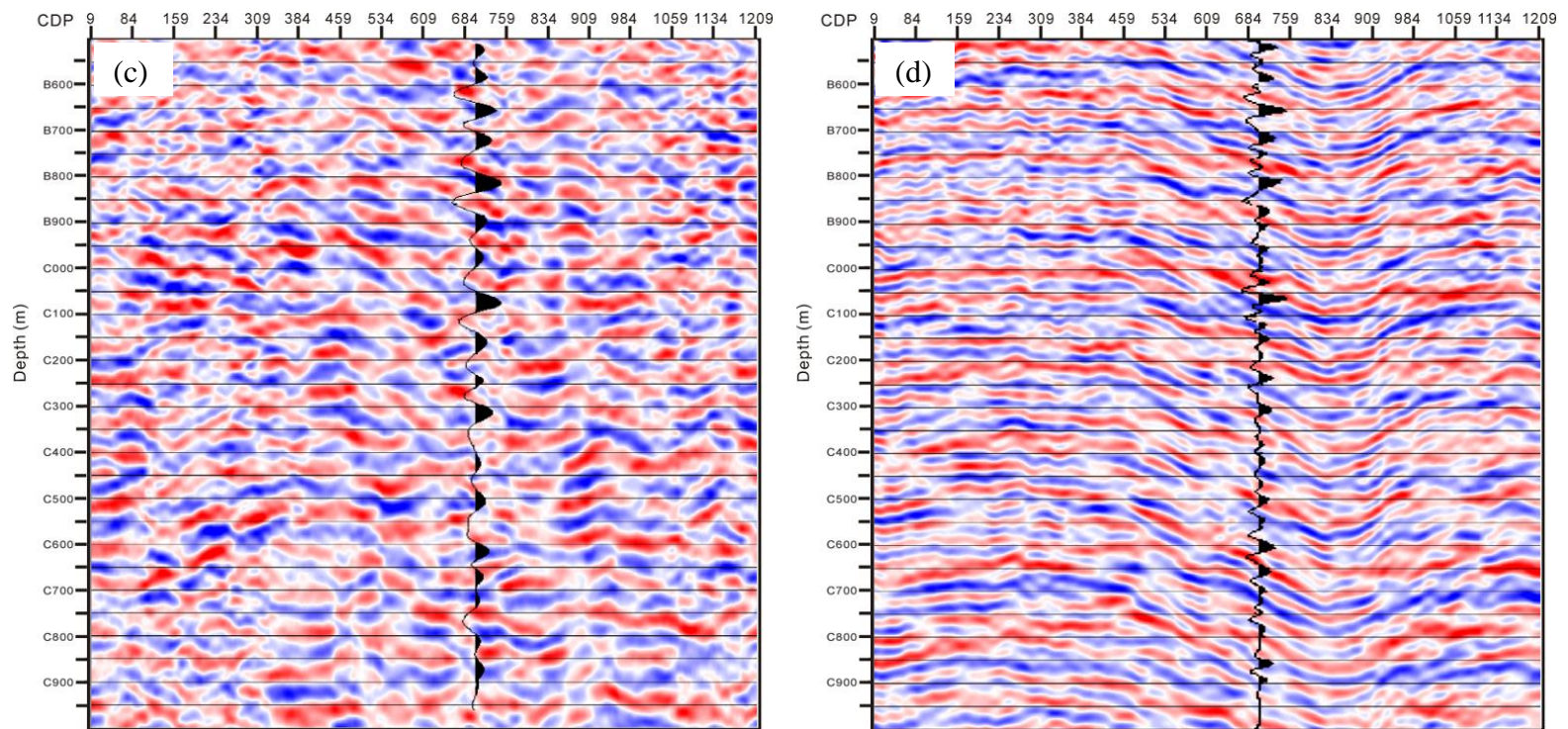


**Figure 51: Continued.**

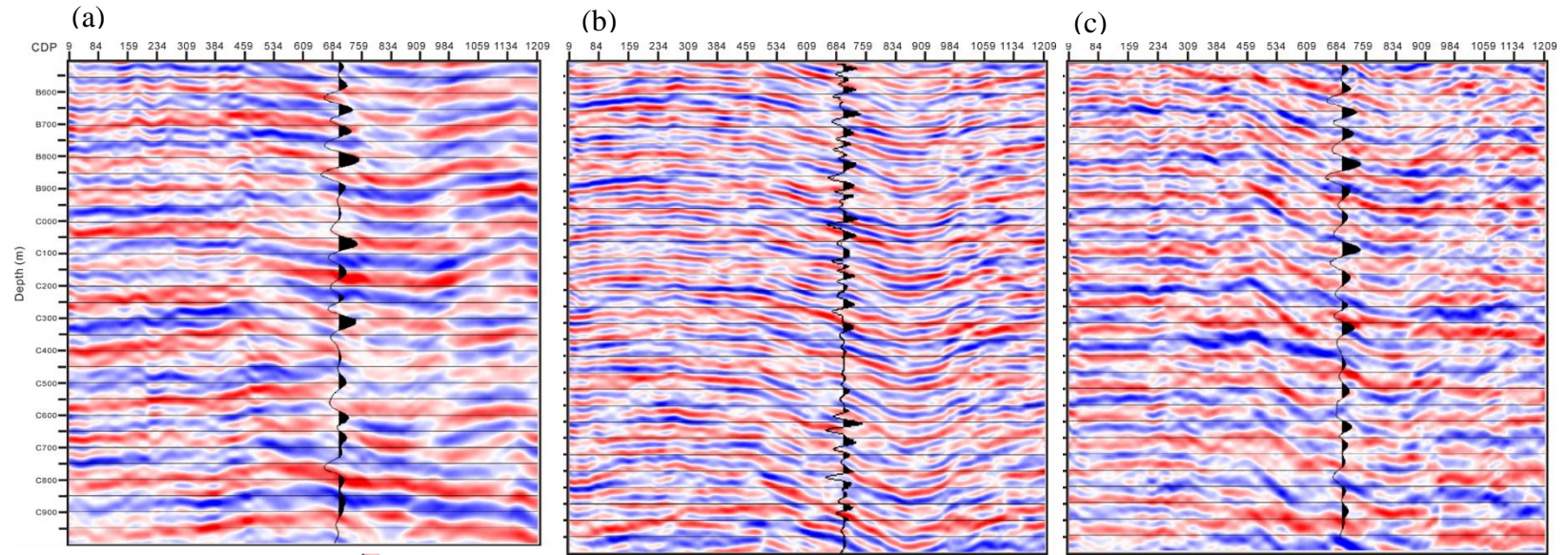


**Figure 52: (a) P stacked section in pressure component (b) PP-S stacked section in vertical component (c) PS-S stacked section in inline component.**

(a)	Pressure Component Data			
	P-P Stack	PP-S Stack	PS-S Stack	Sum
	146.94	126.79	115.41	389.14
	38%	32%	30%	100%

(b)	Inline Component Data			
	P-P Stack	PP-S Stack	PS-S Stack	Sum
	0.0018	0.0104	0.0043	0.0165
	11%	63%	26%	100%
	43.03	245.79	100.32	389.14

(c)	Vertical Component Data			
	P-P Stack	PP-S Stack	PS-S Stack	Sum
	0.00075	0.00077	0.00045	0.00196
	38%	39%	23%	100%
	149.03	151.52	88.59	389.14

**Table 2: Illustrating P-P wave, PP-S wave and PS-S wave energy distributions in pressure component, inline component and vertical component data.**



#### 4. CONCLUSIONS

Though the 4C OBC seismic data acquired in Arabian Gulf provide an opportunity to study converted shear waves, some challenging problems still exist in the study area. First, the shallow-water environment with hard seafloor lead to dispersive surface waves, contaminating the reflection signals. Second, P-P wave, converted PP-S wave and PS-S wave are recorded by hydrophones and 3D geophones. Due to the existence of various wavefields, it is more difficult to design a proper processing flow for 4C OBC seismic data to image P-P wave, PP-S wave and PS-S wave reflection signals in all four components.

First of all, three filtering methods are tested to separate surface waves from reflection signals, based on the low-frequency and low velocity characteristics. Through comparing the filtered shot gather and analyzing the S/N in frequency spectra, the Surface Wave Noise Attenuation method is selected to suppress Scholte waves. After preprocessing sequences, hyperbolic reflection events appear in the CDP records of four components, and the signal-to-noise energy ratio increases a lot in the frequency spectra. Even though the energy in hydrophones is thirty thousand times more than that in geophones, compared with inline and crossline components, the seismic data recorded by vertical geophones have an obviously lower signal-to-noise energy ratio.

The designed processing workflow performed P wave, PP-S wave and PS-S wave extraction and imaging in four-component data. Although hyperbolic reflections exist in the CDP record of crossline component, there is no reflection signals via conventional stacking techniques, due to the cancellation of reflections along the offsets.

The stacked sections in vertical component have higher frequency contents than pressure and inline component data. In spite of the same dominant frequency of signals, it is hard to say which images in pressure and inline component can give an accurate description of subsurface structures. The first criterion is to access how well they match synthetic traces, which relates to the velocity and density variations with depth. Second, the energy distribution of different waveforms is analyzed in each component data. In the end, the P stacked section in pressure component, PP-S stacked section in vertical component and PS-S stacked section in inline component can provide a high-quality subsurface imaging. Although the distinct measurements result in slight differences in these three images, they still display similar geological structures along this 2D test line.

To conclude, the proper processing sequences for the 4C OBC data are proposed in this research to enhance desired signals, extract P wave and converted shear waves, and obtain accurate geological structure images, which can make an improvement in reservoir characterization and petroleum exploration.

## REFERENCES

- Berteussen, K., Sun, Y.F., Ali, M., and Zhang, Z., 2014. Hunting S-waves using 4C seismic data in the carbonates, offshore UAE. *Proc.*, 84th SEG Annual International Meeting, Denver, Colorado, 26-31 October, 347-352.
- Boiero, D., Wiarda, E., and Vermeer, P., 2013. Surface- and guided-wave inversion for near-surface modeling in land and shallow marine seismic data: *The Leading Edge*, 32, 638-646.
- Ernst, F. and Herman, G.C., 2000. Tomography of dispersive media: *Journal of Acoustical Society of America*, 108, 105-116.
- Florian, D., Frederique, B., Katia, G., Raphael, S., and Thomas, B. et al., 2016. Near-surface velocity modeling using a combined inversion of surface and refracted P-waves: *The Leading Edge*, 35, 946-951.
- Garotta, R., Marechal, P., and Magesan, M., 1985. Two-component acquisition as a routine procedure for recording P-waves and converted waves: *Can. J. Expl. Geophys.*, 21, 40-53.
- Hardage, B.A., DeAngelo, M.V., Murray, P.E., and Sava, D., 2011. *Multicomponent Seismic Technology*. Oklahoma: Society of Exploration Geophysicists.
- Henley, D.C., 1999. Coherent noise attenuation in the radial trace domain: introduction and demonstration: *CREWES Research Report*, Volume 11.
- Johns, T.D., Vito, C., Clark, R., and Sarmiento, R., 2006. Multicomponent OBC (4C) prestack time imaging: offshore Trinidad, Pamberi, LRL Block. *Proc.*, SEG Annual International Meeting, New Orleans, Louisiana, 1-6 October, 1193-1197.

- Loewenthal, D., Lee, S.S., and Gardner, G.H.F., 1985. Deterministic estimation of a wavelet using impedance type technique: *Geophysical Prospecting*, 33, 956-969.
- Pinnegar, C.R., and Mansinha, L., 2003a. The bi-Gaussian S transform: *SIAM Journal of Scientific Computing*, 24, 1678-1692.
- ProMAX, 1997. a reference guide for the ProMAX geophysical processing software. Landmark, a Halliburton Company. Volume 2.
- Rodriguez, C., 2000. Advanced marine methods: Ocean-bottom and vertical cable analyses: Ph.D. thesis, University of Calgary.
- Stewart, R.R., Gaiser, J.E., Brown, R.J., and Lawton, D.C., 2003. Converted-wave seismic exploration: Applications: *Geophysics*, 68: 40–57.
- Stockwell, R.G., Mansinha, L., and Lowe, R.P., 1996. Localization of the complex spectrum, the S transform: *IEEE Transactions on Signal Processing*, 44(4): 998-1001.
- Stockwell, R.G., 2007. A basis for efficient representation of the S-transform: *Digital Signal Process*, 17: 371-393.
- Sun, Y.F. and Berteussen, K., 2009. New opportunities of 4C ocean bottom seismic in shallow-water environment of the Arabian Gulf: A case study. *Proc.*, 79th SEG Annual International Meeting, Houston, Texas, 25-30 October, 46-50.
- Sun, Y.F. and Berteussen, K., 2010. Multicomponent seismic acquisition in the Arabic Gulf- Should we take a new look at the acquisition parameters. *Proc.*, 72nd EAGE Conference, Barcelona, Spain, 14-18 June, 124-128.

- Tatham, R.H. and Goolsbee, D.V., 1984. Separation of P- and S-wave reflections offshore western Florida: *Geophysics*, 49, 493-508.
- Yilmaz, O., 2001. Seismic Data Processing. Tulsa: Society of Exploration Geophysicists.
- Zhang, Z., Sun, Y.F., and Berteussen, K., 2010. Analysis of surface waves in shallow water environment of the Persian Gulf using S and t-f-k transform. *Proc.*, 80th SEG Annual International Meeting, Denver, Colorado, 17-22 October, 3723-3728.
- Zhang, Z., Sun, Y.F., and Berteussen, K., 2012. Improving OBC data quality of the geophone components in shallow-water Persian Gulf through advanced time frequency analysis. *Proc.*, 82nd SEG Annual International Meeting, Las Vegas, Nevada, 4-9 November, 1131-1135.
- Zhang, Z., Sun, Y.F., Berteussen, K., and Ali, M., 2013. Effect of Scholte wave on rotation of multi-component OBC seismic data in shallow water environment of the Arabian Gulf. *Proc.*, 83rd SEG Annual International Meeting, Houston, Texas, 22-27 September, 1233-1238.
- Zhang, Z., Sun, Y.F., Berteussen, K., and Ali, M., 2015. 4C OBC shear wave processing in shallow water environment of the Arabian Gulf. *Proc.*, 85th SEG Annual International Meeting, 2113-2117.